Confronting Cosmological Models with Observations

By
Arman Shafieloo

A Thesis For the Degree of

Doctor of Philosophy

(in Physics)

submitted to the

University of Pune

Supervisor: Prof. Varun Sahni

Inter-University Centre for Astronomy and Astrophysics

Post Bag 4, Ganeshkhind, Pune 411 007, INDIA

July 2008

Dedicated to My Parents
and My Brothers

for their love and endless support

Contents

List of Tables

List of Figures

Acknowledgment

I have spent around six years at IUCAA and during this long period of pursuing my PhD I have traveled along a tortuous path. There have been many good occasions and happy times, and on the other hand there have also been some sad moments. Though it is certainly not easy for me to fully express myself in just a few terse words, I would make an effort to thank some people without whose support and help, I could not have come this far.

I would like to thank my supervisor, Varun, who accepted me as his student and taught me many things, scientific and non-scientific. As a *guru*, sometimes he would leave me completely alone with my problems. These difficulties eventually made me much stronger, more confident and relatively independent. And of course when I needed help, he was fully present and supportive. I would like to convey my deep appreciation towards him.

I would like to thank Tarun for almost everything! Tarun for me was not only a fantastic guide, he was also like a caring brother and a great friend to me. I can never forget all his help and kindness. I am indeed very proud of having worked with both Varun and Tarun during my PhD, and I really hope that I can continue collaborating with them in the future.

I would like to thank IUCAA for accepting me as a part of its family in this long period. Specifically I would like to acknowledge Prof. Narlikar, Naresh, Ajit, Paddy, Shyam, Sanjeev, Ranjeev, Joydeep, Swara, Ramaprakash, Srianand and the other IUCAA faculty members from whom I have benefited a lot. I would definitely not forget Sarah, Manisha, Sagar and the other computer center staff, Nirupama and the members of the library staff, Dr. Chellathurai, Madam Lata, Mr. Modak, Mr. Abhyankar, Rajesh, Madam Rao, Kumar, Deepika, Neelima and all the other administrative staff members for their constant and immediate help during the whole of my PhD term at IUCAA.

As a student at IUCAA I have spent most of my time with the students and

post-docs in our colony. I would like to thank all the students and post-docs who made my stay pleasant at IUCAA. I would like to specifically name Anando, Sanjit, Arnab, Amir, Subharthi, Jatush, Param, Ujjaini, Abhishek, Atul, Minu, Siddharth, Susmita, Saumya, Gaurang, Sudipta, Himan, Mudit and Sharanya.

Outside of the IUCAA family I have many friends in Pune. Their company was always very essential for my social life. I would like to name Farshid, Pooria, Golbarg, Karim, Farbod, Sharmin, Shahab, Seyyed, Neda, Meysam, Eun-Sook, Yann and Nina.

I must make a special mention of my ex-wife, Ghazal. She was always a well-wisher for me and I would like to thank her for her caring support during the considerable time that we were together.

During my PhD I have benefited vastly from the scientific and non-scientific discussions that I had with many people. I would like to thank all of them and specifically I would like to name Profs. Alexei Starobinsky, Subir Sarkar, Yuri Shtanov, Rohini Sahni, Sucheta Koshti, Mark Whittle, Reza Mansouri, Torsten Ensslin, Dipak Munshi, Reza Tavakol, Jasjeet Bagla and Tarun Deep Saini.

I would like to thank Maryam for her appearance at the right space-time. Her presence, love and support made life very much pleasant for me.

At the end, I would like to thank my parents, Baba and Ati, and my brothers, Iman and Sharaf. It will take more than some words to say how invaluable their selfless support has been for me.

And at the end, I would like to thank my 5th. standard teacher, Amir Masoud Kamal, who has left a very significant impact on my character, and I will never forget him.

List of Publications

1. Varun Sahni, Arman Shafieloo, Alexei A. Starobinsky,
   "Two new diagnostics of dark energy"
   Submitted to Phys. Rev. D (2008)
   http://arxiv.org/abs/0807.3548

2. Minu Joy, Arman Shafieloo, Varun Sahni, Alexei A. Starobinsky,
   "Is a step in the primordial spectral index favored by CMB data?"
   Submitted to Phys. Rev. D (2008)
   http://arxiv.org/abs/0807.3334

3. Arman Shafieloo, Tarun Souradeep,
   "Estimation of Primordial Spectrum with post-WMAP 3 year data",
   Phys. Rev. **D78** (2008) 023511.
   http://arxiv.org/abs/0709.1944

4. Tarun Souradeep, Arman Shafieloo
   "Early Universe with CMB Anisotropy",
   Prog. Theo. Phys. Supp. **172** (2008) 156.
   http://ptp.ipap.jp/link?PTPS/172/156/

5. Arman Shafieloo,
   "Model Independent Reconstruction of the Expansion History of the Universe and the Properties of Dark Energy",
   Mon. Not. Roy. Ast. Soc. **380** (2007) 1573.
   http://arxiv.org/abs/astro-ph/0703034

6. Arman Shafieloo, Tarun Souradeep, P. Manimaran, Prasanta K. Panigrahi, Raghavan Rangarajan,
"Features in the Primordial Spectrum from WMAP: A Wavelet Analysis",
Phys. Rev. **D75** (2007) 123502.
http://arxiv.org/abs/astro-ph/0611352

7. Arman Shafieloo, Ujjaini Alam, Varun Sahni, Alexei A. Starobinsky,
"Smoothing Supernova Data to Reconstruct the Expansion History of the Universe and its Age",
Mon. Not. Roy. Ast. Soc. **366** (2006) 1081.
http://arxiv.org/abs/astro-ph/0505329

8. Arman Shafieloo, Tarun Souradeep,
"Primordial power spectrum from WMAP",
Phys. Rev. **D70** (2004) 043523.
http://arxiv.org/abs/astro-ph/0312174

Certificate of the Guides

CERTIFIED that the work incorporated in the thesis "**Confronting Cosmological Models with Observations**" submitted by Mr. **Arman Shafieloo** was carried out by the candidate under my supervision/ guidance. Such material as has been obtained from other sources has been duly acknowledged in the thesis.

Prof. Varun Sahni
(Thesis Supervisor)

Declaration by the Candidate

I declare that the thesis entitled "**Confronting Cosmological Models with Observations**" submitted by me for the degree of Doctor of Philosophy is the record of work carried out by me during the period from **June 2005** to **July 2008** under the guidance of **Prof. Varun Sahni** and has not formed the basis for the award of any degree, diploma, associateship, fellowship, titles in this or any other University or other institution of Higher learning.

I further declare that the material obtained from other sources has been duly acknowledged in the thesis.

Date:
Place: Arman Shafieloo

Abstract

The work related to my Ph.D thesis has been on implementing and applying different non-parametric, model-independent statistical methods for analyzing cosmological data, with the purpose of reconstructing important cosmological quantities and parameters. These methods have been applied to the most recent cosmological data sets such as the WMAP data on cosmic microwave background anisotropy, the GOLD and SNLS supernovae data, and to the results from detection of baryon oscillations. My research has been primarily focused on applying some advanced statistical methods (the improved Richardson–Lucy deconvolution method, wavelet analysis, smoothing methods) in two important areas in cosmology. The main questions which I have addressed in my thesis are :

* *Non-parametric recovery of the shape of the primordial power spectrum directly from observations.*

* *Non-parametric reconstruction of the expansion history of the universe and of the properties of dark energy.*

The model-independent reconstruction of cosmological quantities, can be used to examine different cosmological models against observations without biasing the results with any initial model assumption.

The thesis has been organized as follows:

- **Chapter 1** provides a brief introduction and background to the field of cosmology and focuses in the use of CMB and supernovae data in deriving cosmological parameters. The outlines of the new developments in this field over the last decade which motivated the research presented in this thesis are also provided in this chapter.
- **Chapter 2** presents my work on supernovae data and reconstruction of the properties of dark energy in a model independent and non parametric manner.
- **Chapter 3** provides details of my work on direct reconstruction of the primordial power spectrum from CMB WMAP data.
- A summary of the results obtained in this thesis and future directions are provided in **Chapter 4**.
- The thesis also contain several appendices.

Chapter 1

Introduction

Astronomy is the oldest of all sciences. It dates back virtually to the origin of mankind. Bright mysterious points attached to the roof of the night sky have been a constant source of imagination and amazement for our ancestors. It has taken a long time for mankind to understand just what these bright objects are. It is also for few hundred years that we have recognized the sun as a star in the center of our solar system. It has only been a century since we came to know about the existence of the galaxies, each of them consisting of millions of stars like our sun.

However in the last few decades, astronomy and in particular cosmology, has entered into an era of precision science. Progresses in cosmological observations with highly sensitive instruments and advanced measurement techniques have opened up many new windows for us to look deeper into the universe with increasing accuracy. Powerful and fast supercomputers enable us to do huge computations and simulations to analyze the observed data and compare it with theoretical models. On the other hand, more precise data also requires more careful and more advanced statistical methods of analysis to extract maximum amount of science. There have therefore been many advancements in statistical methods of data analysis during the last few years.

My thesis concerns two very important areas of modern cosmology - model independent and non-parametric statistical methods of data analysis applied to **(a)** cosmic microwave background data, so as to reconstruct directly the form of primordial power spectrum, and **(b)** type Ia supernovae data in order to reconstruct the properties of dark energy. The overall introduction and motivation of this thesis is provided in this chapter. The discussions presented here will be brief; more detailed material will be contained in the subsequent chapters.

1.1 Standard model of cosmology

The standard model of cosmology is based on the general theory of relativity. Einstein's discovery of general relativity enabled us to develop a theory of the universe which is testable and can be falsified. So cosmology has become a proper science which can predict events and explain observations. The Big Bang model of the universe which is based on general relativity and is in fact the standard model of the universe at present, has successfully passed several important tests include the expansion of the universe universe as exhibited by the Hubble diagram; light element abundances which are in concordance with big bang nucleosynthesis predictions; observations of the cosmic microwave background which is a black body radiation left over from the young universe when the latter was only a few hundred thousand years old, etc.

The standard cosmological model also needs to account for the origins of inhomogeneities such as galaxies, stars and planets. In the early 1980's the inflationary model was suggested [4–6, 56] and subsequently shown to be able to successfully seed galaxy formation [8–11]. Now this model is being put to several tests by CMB experiments such as COBE, WMAP and (soon) PLANCK.

Besides the key issues of seed initial conditions for galaxies, the standard model must also account for dark matter and dark energy. Currently it is felt that the dark components of the universe, dark matter and dark energy, constitute around 96% of the total energy density of the universe. However, it could also be that the presence of an unseen component implies a crises for the standard model of cosmology and calls for a revision of the general theory of relativity as advocated by some researchers. To determine which is the correct direction for theory to take one must develop sophisticated statistical methods and apply these to observational data in order to get a bias free picture of cosmological observations. This has been a primary objective of this thesis which has developed model independent and non-parametric statistical approaches to study two important issues in modern cosmology: (i) the form of the primordial perturbations spectrum and (ii) the properties of dark energy. Before embarking on our study of these two topics we briefly review some important issues in cosmology related to our studies.

1.1.1 The Robertson-Walker Universe

The most general expression for a 4 dimensional metric which contains a 3 dimensional maximally symmetric subspace is the Friedmann-Robertson-Walker (FRW)

space-time:

$$ds^2 = dt^2 - a(t)^2\Big[\frac{dr^2}{1-kr^2} + r^2(d\theta^2 + sin^2\theta d\phi^2)\Big], \tag{1.1}$$

where $a(t)$ is the cosmological scale factor while the curvature constant k has discrete values of +1, 0 or −1 corresponding respectively, to closed, flat or open geometries. This formalism holds for a homogeneous and isotropic universe. Different cosmological observations have shown that our universe is indeed isotropic and homogeneous on large scales, so we shall follow this prescription in the whole thesis. Eqn (1.1) can also be written as

$$ds^2 = dt^2 - a(t)^2\Big[d\chi^2 + S_k^2(\chi)(d\theta^2 + sin^2\theta d\phi^2)\Big], \tag{1.2}$$

where $S_k(r)$ is $sin(\chi)$,χ,$sinh(\chi)$ for $k = +1, 0, -1$ and χ is dimensionless.

1.1.2 The Friedmann equations

The cosmological equations of motion in a FRW metric are derived from the Einstein equations [1]:

$$R_{\mu\nu} - \frac{1}{2}g_{\mu\nu}R = 8\pi G\sum_i T^{(i)}_{\mu\nu} \tag{1.3}$$

where Λ is the cosmological constant, G is Newton constant, $T_{\mu\nu}$ is the energy-momentum tensor, $R_{\mu\nu}$ is the Ricci tensor and $g_{\mu\nu}$ is the space-time metric described by eqn (1.1). Assuming the matter content of the universe to be a perfect fluid, we will have:

$$T^{(i)}_{\mu\nu} = -p_i g_{\mu\nu} + (p_i + \rho_i)u^{(i)}_\mu u^{(i)}_\nu \tag{1.4}$$

where p_i is the isotropic pressure, ρ_i is the energy density and $u^{(i)} = (1, 0, 0, 0)$ is the velocity vector for the i^{th} isotropic fluid in co-moving coordinates. So, in this case, by assuming the matter content to be a perfect fluid, the Einstein's equations lead to Friedmann equation:

$$H^2 = \sum_i \frac{8\pi G\rho_i}{3} - \frac{k}{a^2} \tag{1.5}$$

and the Roychaudhury equation:

$$\frac{\ddot{a}}{a} = -\frac{4\pi G}{3}\sum_i (\rho_i + 3p_i), \tag{1.6}$$

where $H = \frac{\dot{a}}{a}$ is the Hubble parameter. For the i^{th} matter component the energy conservation equation $T^{\mu\nu}_{;\mu} = 0$ leads to

$$\dot{\rho}_i = -3H(\rho_i + p_i). \tag{1.7}$$

Now we have a full expression of the evolution of our universe as a function of different cosmological components and parameters. It is common in cosmology to define dimensionless parameters, $\Omega_i = \rho_{0i}/\rho_{0c}$, by comparing them with the critical density:

$$\rho_{0c} = \frac{3H_0^2}{8\pi G} = 1.88 \times 10^{-29}\ h^2\ g\ cm^{-3} \tag{1.8}$$

where $h = \frac{H_0}{100\ km/sec/Mpc}$. In terms of the dimensionless parameters Friedmann equation, eqn (1.5), becomes particularly simple:

$$k/a^2 = H^2(\Omega_{tot} - 1) \tag{1.9}$$

where $\Omega_{tot} = \sum_i \rho_i/\rho_c$. In this new format, one can see that when $\Omega_{tot} > 1$, $k = +1$ and the universe is closed, when $\Omega_{tot} = 1$, $k = 0$ and the universe is spatially flat, when $\Omega_{tot} < 1$, $k = -1$ and the universe is open.

1.2 Cosmological parameters

Within any model proposed to explain a dynamical system there are some parameters which define the evolution and dynamics of the system qualitatively. In fact a model suggested to explain any phenomena is a basic frame which only by defining its parameters can be confronted with observations and tested. A good model is a model which can explain the evolution of a system, can predict correctly the events and has also a few number of free parameters. Our standard model of cosmology (together with its companion theories such as inflation), has also several free parameters which need to be determined from observations. In the standard model, the universe is a perturbed FRW space-time with dynamics governed by the Einstein equations. All cosmological components with different densities and different equations of state ($w_i = \frac{p_i}{\rho_i}$, p_i is the pressure and ρ_i is the energy density of the i^{th} component) are responsible for the overall dynamics of our cosmological system. The Friedmann equation, eqn (1.5), expressed in terms of the cosmological redshift $z(t) = \frac{a_0}{a_t} - 1$ becomes

$$\frac{H^2}{H_0^2} = \sum_i \Omega_{0i}(1+z)^{3(1+w_i)} + (1 - \sum_i \Omega_{0i})(1+z)^2. \tag{1.10}$$

Below we briefly comments on some important cosmological parameters.

Hubble parameter

The value of the Hubble parameter as a function of redshift was given in eqn (1.10). Its present value $H_0 = (\frac{\dot{a}}{a_0})_{t=t_0}$, denotes the expansion rate at the current epoch. A recent measurement of the Hubble constant from the Hubble Space Telescope KeyProject [2] estimated $H_0 = 72 \pm 3(\text{statistical}) \pm 7(\text{systematic}) km\ sec^{-1}\ Mpc^{-1}$ by using the empirical period-luminosity relation for Cepheid variable stars to obtain distances to 31 galaxies. This result is in very good agreement with estimates of H_0 derived from observation of the cosmic microwave background made by the WMAP satellite [3].

Curvature parameter

The observed value of the curvature parameter $\Omega_{0k} = -k/a_0^2 H_0^2 = 1 - \sum_i \Omega_{0i} = -0.099^{+0.085}_{-0.100}$ [3] provides strong support for a spatially flat universe as originally predicted by the inflationary scenario [4–6, 56]. This has important implications for the total matter density of the universe as we discuss later.

1.2.1 Matter density

As noted above, observations of the cosmic microwave background suggest a universe which is close to being spatially flat. In other words $\Omega_{tot} \simeq 1$. Big bang nucleosynthesis constraints imply that the baryon density in the universe is less than 5% of the total value, the remaining 95% of the dark universe is divided amongst dark matter (25%) and dark energy (70%). Furthermore there is considerable observational support for the cold dark matter model according which dark matter is non-baryonic and collision-less. Although interesting alternatives have also been suggested [40].

In addition to non-baryonic cold dark matter, it is widely believed that our universe contains a small amount of hot dark matter in terms of ultralight massive neutrinos with total density not exceeding 1%. Finally we would also like to mention the important role played by the radiation density which, though is small today, was large at early times, before recombination.

1.2.2 Cosmological Constant

The cosmological constant was originally introduced by Einstein in 1917 [1]. The cosmological constant has a constant equation of state of $w = -1$. Although introduced in 1917 the so called Λ -term has had a checkered history. Its recent prominence in cosmological literature is largely due to supernovae observations [12, 27, 41–47] supported by CMB and other datasets [3, 100], which points to the interesting fact that the universe may currently be accelerating. To generate this acceleration one requires a component with a negative pressure and with a relatively large value of the energy density as compared with dark and baryonic matter. Currently it is our belief that the cosmological constant density must be as least 2/3 of the total energy budget of the universe. However many other theoretical candidates for a matter component with similar characteristics to the cosmological constant have been proposed [19,20,37–39]. All these candidates together are called dark energy. One of the challenges of cosmology is to define which one is in fact responsible for the acceleration of the universe.

1.2.3 Density perturbation amplitude and spectral index

We need to include a description about deviations from homogeneity to complete our description about the universe. The curvature perturbation R, describes inhomogeneities in the early universe. The curvature perturbation, in fact measures the spatial curvature of a comoving slice of the space time. Zeldovich and Harrison suggested a scale invariant form of the curvature power spectrum [13–15] (from now on we simply call it power spectrum or primordial power spectrum, in other cases like when we mean the matter power spectrum we specifically bring the full name). In the Harrison-Zeldovich form of the power spectrum, $P(k) = constant$, and the power does not vary for different scales. A more general approximation for the form of the power spectrum is power law form of the primordial spectrum:

$$P_R(k) = A_s[\frac{k}{k_*}]^{n_s-1} \tag{1.11}$$

where n_s is known as the spectral index, A_s is the density perturbation amplitude, and k_* is an arbitrarily chosen scale. We can see that in the case of the Harrison-Zeldovich power spectrum we have $n_s = 1$. It is very interesting that observations support the power law form of the primordial spectrum and require n_s to be close to 1, which corresponds to the perturbation in the curvature being almost indepen-

dent of scale. We should note that the subsequent evolution by the transfer function (which is a function of our cosmological parameters) will modify the power spectrum from its initial form. On the other hand, inflationary cosmology enables us to have a theoretical mechanism which generates initial perturbations and results in a power spectrum which is close to being scale invariant [8–11]. It is widely accepted that inflationary cosmology is now an important part of our standard model which can answer many basic questions in cosmology and has been very successful in confronting different cosmological observations.

In cosmological parameter estimation it is very common to assume a power law form for the primordial power spectrum. Hence A_s and n_s are considered as a pair of cosmological parameters. However we should emphasize here that this is just an assumption and as we will see later, a considerable part of this thesis is devoted to the reconstruction of the primordial spectrum directly from observational data and independently of any assumptions. It is also worth mentioning that a power law form of the power spectrum is not the only one predicted from inflation and there are some inflationary scenarios which give rise to features in the form of the primordial power spectrum [22, 23, 139–144].

1.2.4 Tensor to scalar ratio

Inflation generates perturbations by amplifying quantum fluctuations and stretching them to astrophysical scales through rapid expansion. The simplest inflationary scenarios based on a single scalar field generate both scalar field perturbation as well as tensor metric fluctuations (gravity waves).

Fluctuations in the scalar field subsequently result in structure formation in the universe via gravitational instability, while the tensor metric fluctuations give rise to a relic gravity background. Both tensor and scalar fluctuations perturb the CMB. The ratio between the tensor power spectrum and scalar power spectrum in the CMB is characterized by the tensor to scalar ratio, r. This ratio can be derived by analyzing the cosmic microwave background data and comparing with theoretical predictions from different inflationary scenarios. In the following we briefly discuss the tensor to scalar ratio for a single scalar field (slow roll) inflation.

Inflation leads to a period of early acceleration $\ddot{a} > 0$ during which

$$\frac{d}{dt}(\frac{1}{aH}) < 0 \tag{1.12}$$

in other words, during the inflationary epoch the comoving Hubble length, $1/aH$,

decreases with time. From eqn (1.6) we find that a necessary (but not sufficient) condition for inflation is

$$\rho + 3p < 0. \tag{1.13}$$

So we see that, in order to obtain inflation, we need a material with the very unusual property of negative pressure (similar to Λ or any other candidate of dark energy, but here it must be a dominant agent by a huge factor and also it needs to decay subsequently to baryons, dark matter and radiation). Scalar fields are good candidates for our purpose. For the energy density and pressure of a homogeneous scalar field, $\phi = \phi(t)$, we find

$$\rho_\phi = \frac{1}{2}\dot{\phi}^2 + V(\phi) \tag{1.14}$$

and

$$p_\phi = \frac{1}{2}\dot{\phi}^2 - V(\phi) \tag{1.15}$$

where $V(\phi)$ is the potential of the scalar field and $\frac{1}{2}\dot{\phi}^2$ is its kinetic energy. Next, by assuming the scalar field to be the dominant component in a spatially flat universe, we can derive the following equations describing the inflationary era:

$$H^2 = \frac{1}{3M_{pl}^2}[V(\phi) + \frac{1}{2}\dot{\phi}^2] \tag{1.16}$$

and

$$\ddot{\phi} + 3H\dot{\phi} = -\frac{dV}{d\phi} \tag{1.17}$$

where $M_{pl} = (8\pi G)^{-1/2} = 4.342 \times 10^{-6} g = 2.436 \times 10^{18} GeV$ is the reduced Planck mass. To satisfy the inflationary condition, eqn (1.13) we must have $\dot{\phi}^2 < V(\phi)$ which arises for sufficiently flat potentials. It is interesting that even if we start with a non-flat spatially geometry, a suitably flat potential makes the curvature term in the Friedmann equation less important as inflation gets underway. In fact it is one of the predictions of inflation that the geometry of the universe must flatten towards the end of inflation which is indeed in agreement with recent CMB observations. The most common approach to studying single field inflation is by means of the slow-roll approximation. In this approximation we neglect the $\dot{\phi}^2$ term in comparison with $V(\phi)$ and we also assume that $\ddot{\phi}$ must be negligible in

comparison to other terms in eqn (1.17) Hence:

$$H^2 \simeq \frac{V(\phi)}{3M_{pl}^2} \tag{1.18}$$

and

$$3H\dot{\phi} \simeq -V'(\phi) \tag{1.19}$$

where $V'(\phi) = \frac{dV}{d\phi}$. The slow-roll approximation translates into the following requirements for the slow-roll parameters, ϵ and η:

$$\epsilon(\phi) = \frac{M_{pl}^2}{2}\Big(\frac{V'}{V}\Big)^2 << 1 \tag{1.20}$$

and

$$|\eta(\phi)| = M_{pl}^2\Big|\frac{V''}{V}\Big| << 1. \tag{1.21}$$

In the slow-roll approximation the scalar and tensor spectra can be written as [17]

$$P_R(k) \simeq \frac{1}{24\pi^2 M_{Pl}^4}\frac{V}{\epsilon}\Big|_{k=aH} \tag{1.22}$$

$$P_{grav}(k) \simeq \frac{2}{3\pi^2 M_{Pl}^4} V\Big|_{k=aH} \tag{1.23}$$

where, in each case, the expressions in the right hand side are calculated when the scale k is equal to the Hubble radius during inflation. The symbol $\simeq$ indicates the slow roll approximation has been used, which is expected to be accurate to a few percent. As a result one can compute the spectral index in eqn (1.11):

$$n_s \simeq 1 - 6\epsilon + 2\eta. \tag{1.24}$$

One can also compute n_{grav} for the gravity waves by defining $P_{grav}(k) = A_{grav}(\frac{k}{k_*})^{n_{grav}}$,

$$n_{grav} \simeq -2\epsilon \tag{1.25}$$

and the tensor to scalar ratio [139]

$$r \equiv \frac{P_{grav}(k_*)}{P_R(k_*)} \simeq 16\epsilon \simeq -8n_{grav} \tag{1.26}$$

which is also known as the consistency equation. The five-year WMAP data has given the upper limit on the tensor to scalar ratio $r < 0.43$ (with 95% CL), for the standard ΛCDM model assuming a power-law primordial spectrum [3].

1.2.5 Other important cosmological parameters

Optical depth to reionization

In Big Bang cosmology, reionization is the process that reionized the matter in the universe after the "dark ages" which lasted from $z \simeq 1000$ until $z \simeq 20$. It is the second of two major phase changes of hydrogen gas in the universe.

The first phase change was recombination, which occurred due to the cooling of the universe to the point where the CMB temperature dropped to $T \simeq 3000K$ at which point the rate of combination of an electron and proton to form neutral hydrogen was higher than the ionization rate of hydrogen by photon. This occurred at $z_{rec} \simeq 1089$ [3]. Thereafter the universe became transparent to the propagation of radiation.

The second phase change occurred once gravitationally bound objects started to form in the early universe. Explosive releases of energy from such objects (population III stars, quasars, etc) were energetic enough to ionize neutral hydrogen. As these objects formed and radiated energy, the universe went from being neutral back to being an ionized plasma at a redshift $6 < z < 20$ [1].

The electron-scattering optical depth, known as $\tau(z_{reion})$, is an important cosmological parameter characterizing this second phase change. In an FRW universe it is given by

$$\tau(z_{reion}) = c \int_0^{z_{reion}} \frac{n_e(z)\sigma_T dz}{(1+z)H(z)} \tag{1.27}$$

where n_e is the electron density and σ_T is the Thomson cross-section describing scattering between electrons and CMB photons and z_{reion} is the redshift of reionization. The most recent results from WMAP 5 year data gives $z_{reion} = 11 \pm 1.4$ corresponding to an optical depth of $\tau = 0.087 \pm 0.017$ for the standard ΛCDM model with power law model of the primordial spectrum [3].

[1] When protons and electrons are separate, they cannot capture energy in the form of photons. Photons may be scattered, but scattering interactions are infrequent if the density of the plasma is low. Thus, a universe full of low density ionized hydrogen will be relatively translucent, as is the case today.

Age of the universe

As we have seen in eqn (1.10), the expansion history of the universe is directly related to the matter-energy components of the universe. Knowing all cosmological parameters related to the matter-energy components of the universe, we can derive the expansion history and by knowing the expansion history we can simply calculate the look back time and age of the universe

$$t(z) = \int_z^\infty \frac{dz'}{(1+z')H(z')} \tag{1.28}$$

Assuming our standard ΛCDM model of cosmology, the WMAP 5 year data derived the age of the universe equal to 13.69 ± 0.13 Gyr [3].

Redshift of matter radiation equality

Shortly before the universe recombined the matter and radiation densities equalized. This occurred at the redshift $z_{eq} \approx 3200$.

Deceleration parameter and epoch of acceleration of the universe

The deceleration parameter measures the change in the rate of expansion of the universe. It can be simply derived by taking the derivative of the Hubble parameter with respect to redshift

$$q(z) \equiv \frac{-\ddot{a}}{aH^2} = \frac{H'(z)}{H(z)}(1+z) - 1 \tag{1.29}$$

$q(z) < 0$ corresponds to acceleration and $q(z) > 0$ to deceleration. The redshift z_* at which $q(z_*) = 0$ determines the transition epoch. As we will see later in the second chapter of this thesis, we have introduced a new method of reconstruction which can calculate z_* in a model independent manner.

Acoustic shift parameter and the redshift of the last scattering surface

The acoustic shift parameter R is directly related to the position of acoustic peaks in the observed angular power spectrum of the cosmic microwave background. The shift parameter R can be also computed theoretically

$$R = \sqrt{\Omega_{m0}} \int_0^{z_{ls}} \frac{dz'}{H(z')}, \tag{1.30}$$

from where we see it related to the matter density as well as the expansion history of the universe right until the redshift of last scattering, z_{ls}. z_{ls} is the redshift where the radiation starts to freely propagate in the universe after Hydrogen and Helium recombine. This quantity can also be computed through the fitting function given in [18]

$$z_{ls} = 1048[1 + 0.00124(\Omega_b h^2)^{-0.738}][1 + g_1(\Omega_{0m} h^2)^{g_2}] \tag{1.31}$$

where g_1 and g_2 are defined as

$$g_1 = 0.078(\Omega_b h^2)^{-0.238}[1 + 39.5(\Omega_b h^2)^{0.763}]^{-1} \tag{1.32}$$

$$g_2 = 0.56[1 + 21.1(\Omega_b h^2)^{1.81}]^{-1} \tag{1.33}$$

where again is a function of some main cosmological parameters: matter density, baryon density and the Hubble parameter. Results from WMAP 5 year data give $R = 1.713 \pm 0.020$ and $z_{ls} = 1087.9 \pm 1.2$ [3].

1.3 Cosmological observations

In order to understand our universe we need to find the correct cosmological model and determine its parameters by testing its predictions against observations. The standard model of cosmology, namely ΛCDM with a power law primordial spectrum, has been very convincing in explaining many different kinds of cosmological observations. In figure 1.1 we see the observational constraints on the parameters of ΛCDM obtained using type Ia supernovae, cosmic microwave background and baryon acoustic peak oscillation (BAO) data. In this section we briefly review some important cosmological observations which have been used in this thesis to determine the cosmological properties of the universe in a quasi-model-independent manner. Although we shall focus on observations of **Type Ia supernovae** and the **cosmic microwave background** we should note here that beside these two important cosmological observations, we can also name galaxy clustering, clusters of galaxies, direct measurements of the Hubble parameter, clustering in the intergalactic medium, gravitational lensing and observations of the peculiar velocities of galaxies as other important cosmological probes.

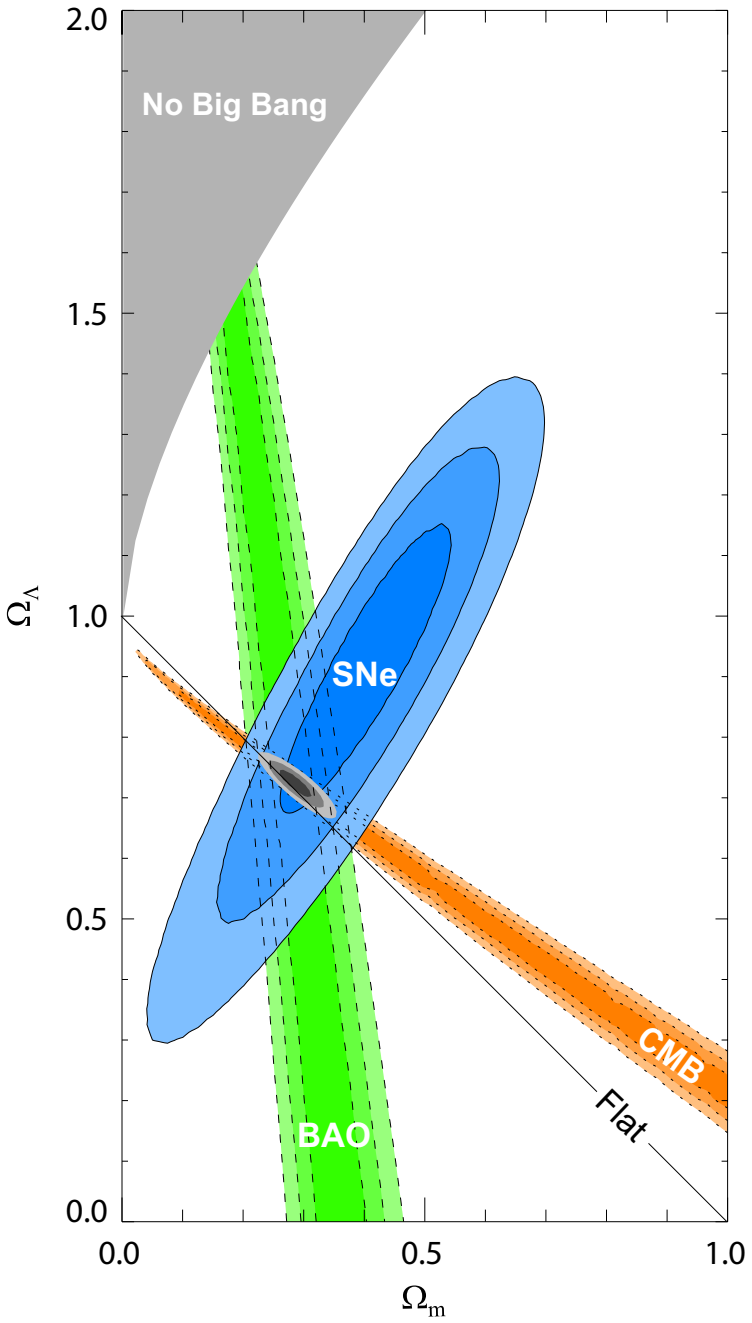

Figure 1.1: 68.3%, 95.4% and 99.7% confidence level contours on Ω_m and Ω_Λ obtained from CMB, BAO and the Union supernovae data set, as well as their combination for a ΛCDM model (figure is from [27]).

1.3.1 Type Ia supernovae

Type Ia supernovae[2]are extremely bright objects which can be seen by current telescopes from a very large cosmological distance. They also have the unique characteristic of being a standard candle. The dispersion in their peak luminosity is very small, $\Delta m = 0.3$ and their absolute brightness is $M_B \simeq -19.5$. In addition the light curve of a type Ia supernova is correlated with its peak luminosity to a precision of $\sim 7\%$ so that brighter supernovae take longer to fade (it takes around 20 days for a Type Ia supernova to rise from relative obscurity to its maximum light). These characteristics makes a type Ia supernova an ideal astronomical object to study the universe on very large scales. From the theoretical point of view, the relation between observed flux, f_{obs} and the intrinsic luminosity of an object, F_{int} depends on the luminosity distance,

$$f_{obs} = \frac{F_{int}}{4\pi d_L^2}. \tag{1.34}$$

In the Newtonian perspective, this luminosity distance is equal to the actual Euclidean distance but in the general theory of relativity, the geometry of space can be non-Euclidean and the luminosity distance to an object depend to both upon the geometry of the space as well as the expansion history of the universe. We can derive the luminosity distance as

$$d_L(z) = \frac{(1+z)}{H_0\sqrt{|\Omega_{k0}|}} S\Big[\sqrt{|\Omega_{k0}|}\int_0^z \frac{dz'}{H(z')}\Big], \tag{1.35}$$

where $S(x) = sin(x), x, sinh(x)$ for a closed, flat and open universe. Specializing to the case of a spatially and expanding FRW universe, which we focus on in this thesis

$$d_L(z) = (1+z)\int_0^z \frac{dz'}{H(z')}. \tag{1.36}$$

We therefore find that the luminosity distance is directly related to the expansion history of the universe. As we have seen earlier, the expansion history of the universe is in turn related to the matter and energy components of the universe through eqn (1.10). In figure 1.2 one can see how, by varying Ω_m and Ω_Λ for a

[2]If a supernova's spectrum contains a line of hydrogen it is classified Type II; otherwise it is Type I. Type Ia supernovae presents a singly-ionized silicon (Si II) line at 615.0 nm, near peak light. Type Ib supernovae have Non-ionized helium (He I) line at 587.6 nm and no strong silicon absorption feature near 615 nm. In type Ic supernovae there are weak or no helium lines and no strong silicon absorption feature near 615 nm.

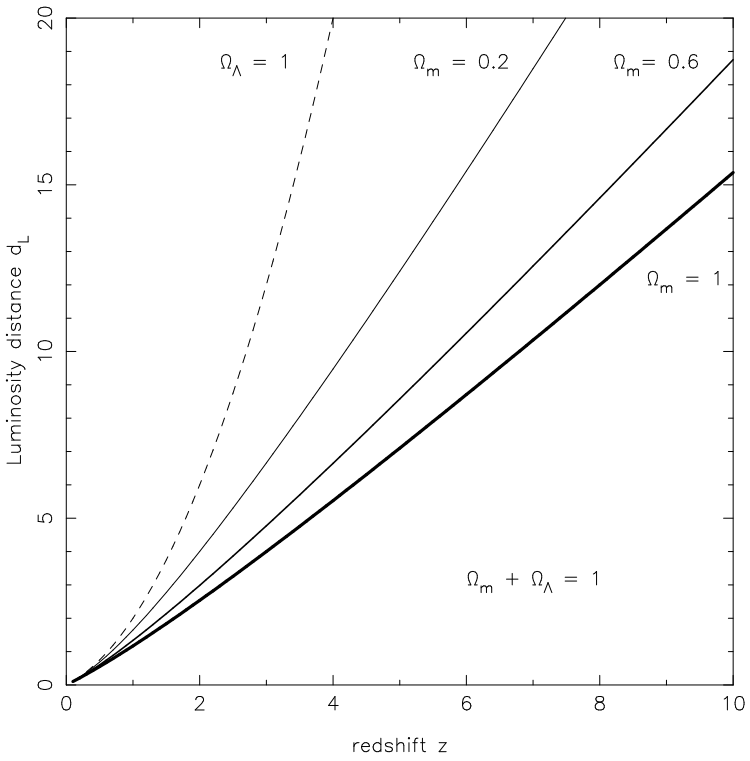

Figure 1.2: The luminosity distance d_L (in units of H_0^{-1}) is shown as a function of cosmological redshift for spatially flat cosmological models with $\Omega_m + \Omega_\Lambda = 1$. We can clearly see the sensitivity of the luminosity distance to the main energy components of the universe (figure is from [19]).

flat ΛCDM model we get different luminosity distances to different redshifts. Since type Ia supernovae are standardized candles, we can with their help determine the luminosity distance up to redshifts of about unity.

By neglecting the small effects of the radiation density in the late universe (and assuming spatial flatness) we can write the most general form of the equation for the expansion history of the universe for collisionless (cold) matter and time varying dark energy as

$$\Big(\frac{H(z)}{H(0)}\Big)^2 = \Omega_{m0}(1+z)^3 + (1-\Omega_{m0})\, exp\Big[\int \frac{3(1+w(z))dz}{1+z}\Big]. \tag{1.37}$$

Therefore by knowing (or assuming) the current value of the matter density we can derive the theoretical luminosity distance for a given model of dark energy and confront the latter with the observed luminosity distances of type Ia supernovae. To be precise, we should mention here that the observed quantity is in fact the distance

modules, $\mu(z)$ which has a direct relation to the luminosity distance by

$$\mu(z) = 5\ log_{10}[d_L(z)] + 25. \tag{1.38}$$

Since we can observe type Ia supernovae up to moderately high redshifts, they have become one of the main sources of information for the cosmological community to analyze the universe on these scales. In the second chapter of this thesis we use supernovae data extensively in our analysis. The most recent uniform catalog of the supernovae type Ia consist of 307 data points up to the redshift of $z = 1.4$ [27].

1.3.2 Cosmic microwave background

The cosmic microwave background was discovered in 1965 by Penzias and Wilson [28] but predicted much earlier by George Gamow and his colleagues [29]. The CMB has the highest background radiation density in the universe. The CMB spectrum can be very well described by a blackbody function with $T = 2.725 \pm 0.001\ K$. This radiation is one of the biggest pillars of the hot big bang scenario which is the basis of our standard model of cosmology. Another important observable quantity is the CMB anisotropy which is the spatial variation in temperature (or intensity) of the CMB sky. There is a very significant amount of information hidden in these anisotropies which can help us to understand our universe and compute the cosmological parameters. Since the first detection of these anisotropies by COBE satellite [30] (which resulted in a Noble prize for George Smooth and John Mather), there have been intense activities to map the sky in different angular scales in order to analyze and study cosmological models and determine the parameters of the universe. During the last 20 years there have been many ground-based, balloon-borne and space-based probes of the CMB anisotropy. In combination with other cosmological observations, CMB anisotropy measurements place quite precise constrains on the cosmological parameters.

Description of CMB anisotropies

Observations show that after subtraction of monopole and dipole contribution the CMB contains of anisotropies of the order of 10^{-5} over a wide range of multipoles. These anisotropies are usually expressed by using a spherical harmonic expansion of the CMB sky:

$$T(\theta,\phi) = \sum_{lm} a_{lm} Y_{lm}(\theta,\phi), \tag{1.39}$$

where Y_{lm}'s are the spherical harmonics. The majority of the needed information is contained in the temperature 2-point function that is in fact the variance as function of separation θ. If we assume the Gaussian statistics and if there is no preferred direction, then what is important here would be the variance of the temperature field which carries all the cosmological information and the individual a_{lm}'s would not be so important for us. So we can define the angular power spectrum which fully characterizes the anisotropies by $C_l \equiv \left\langle |a_{lm}|^2 \right\rangle$ and the power at each l will be $(2l+1)C_l/(4\pi)$. However there are some important points that we should consider. Since we have only one universe that we live in, and we have only one realization of the CMB sky, then even for an ideal full sky observation we are still bound by cosmic variance. Cosmic variance is the variance of each measured C_l which is in fact the variance of the variance. Since each C_l is χ^2 distributed with $(2l+1)$ degrees of freedom, the cosmic variance for each C_l can be derived as $[2/(2l+1)]C_l^2$. We should consider that this cosmic variance is for the ideal case of the full sky map and if we have a fractional sky coverage, f_{sky}, this variance is increased by $1/f_{sky}$ and the modes becomes partially correlated. So we see that the cosmic variance is an unavoidable source of uncertainty specifically at low l's. This is specifically important when we compare theoretical models with CMB observations. In the analysis of the CMB anisotropies usually we neglect the monopole(l=0) and the dipole (l=1) contributions. The monopole of the CMB maps refer to the mean average temperature of the CMB radiation which is around $2.725 \pm 0.001K$. The largest anisotropy is in the $l = 1$ (dipole) first spherical harmonic, with amplitude 3.346 ± 0.017 mK [31]. The dipole is usually interpreted to be the result of the Doppler shift caused by the motion of the solar system relative to the nearly isotropic blackbody field, as confirmed by measurements of the radial velocities of local galaxies [32]. The dipole is a frame dependent quantity, and one can thus determine the 'absolute rest frame' of the Universe as that in which the CMB dipole would be zero. Our velocity relative to the Local Group, as well as the velocity of the Earth around the Sun, and any velocity of the receiver relative to the Earth, is normally removed for the purposes of CMB anisotropy study.

CMB anisotropies and cosmological parameters

In the previous subsection we have briefly introduced the angular power spectrum the CMB anisotropies. The observed angular power spectrum can be confronted with predictions of different cosmological models. Interestingly different cosmological models can have very different impacts on the angular power spectrum which can be easily tested by comparing them with the observations. Even within a single cosmological model, like our standard ΛCDM model, the predicted angular power spectrum at different scales changes significantly by changing the cosmological parameters. Hence we can perform the cosmological parameter estimation by using the observed angular power spectrum from CMB maps.

The angular power spectrum can be considered as a vector, C_l, which is derived from multiplication of a matrix, $G(l,k)$ by another vector $P(k)$. $P(k)$, as we have seen earlier, describes primordial perturbations at the end of inflation and $G(l,k)$ is the transfer function. The transfer function, $G(l,k)$, depends on the assumed cosmological model and its parameters. So as we see, the derived angular power spectrum can be different by assuming different models of primordial spectrum and also it can be different by assuming different cosmological models or using different cosmological parameters. In figure 1.3 we see the sensitivity of the angular power spectrum to four fundamental cosmological parameters. Clearly a precise measurement of the angular power spectrum can be very useful to estimate different cosmological parameters.

Physics of cosmic microwave background anisotropy includes many different effects and consequences which have been studied and understood during the last few decades. These include Sachs-Wolf effect, Integrated Sachs-Wolf effect, Silk damping, Sunyaev-Zeldovich effect, CMB polarization, angular resolution and binning, physics and statistics of non-circular beams, foregrounds and map cleanings, secondary anisotropies, higher order statistics etc. It is beyond the scope of this thesis to discuss these effects in detail and we shall focus hereafter only on methods of reconstructing the primordial power spectrum.

1.4 Beyond the standard model

In this section we briefly discuss extensions to the standard cosmological model. There are possibilities that our universe may be much more complicated than the standard model introduced in the previous section. In addition, the standard of

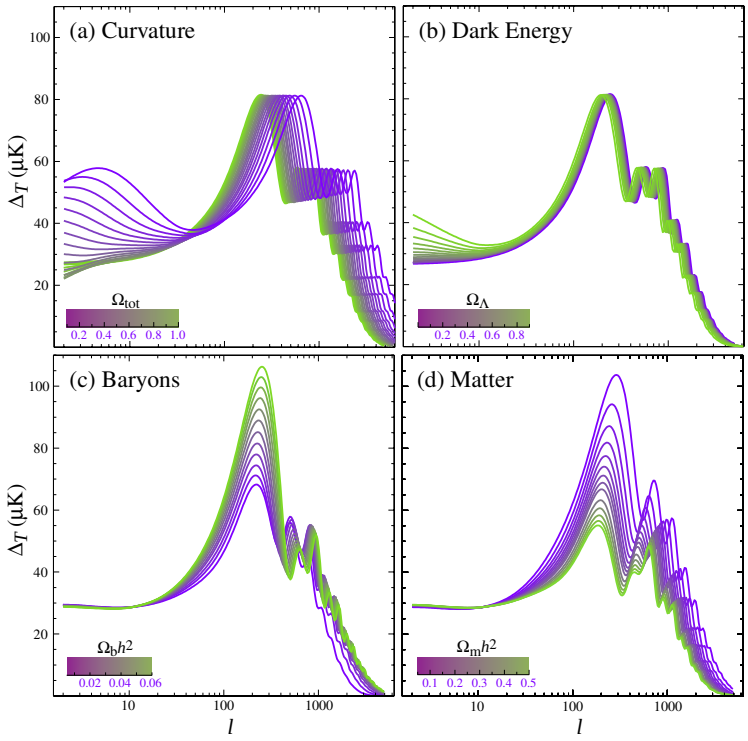

Figure 1.3: Sensitivity of the angular power spectrum to four fundamental cosmological parameters (a) the curvature as quantified by Ω_{tot} (b) the dark energy as quantified by the cosmological constant Ω_Λ ($w_\Lambda = -1$) (c) the physical baryon density $\Omega_b h^2$ (d) the physical matter density $\Omega_m h^2$, all varied around a fiducial model of $\Omega_{tot} = 1$, $\Omega_\Lambda = 0.65$, $\Omega_b h^2 = 0.02$, $\Omega_m h^2 = 0.147$, $n = 1$, $z_{reion} = 0$ (figure is from [33]).

cosmology assumes an adiabatic and Gaussian initial perturbations. In general primordial perturbations can be both adiabatic and isocurvature and the possibility of non-Gaussian fluctuations has also been widely discussed in the literature. The ionization history of the universe too can be much more complicated than in the standard model which assumes rapid ionization. But observational evidence is mixed and maybe we have to improve our analysis with a better and more complicated approximation which may result in a change to our basic set of cosmological parameters. Properties of dark matter can differ from the assumptions of the standard model where we assume the dark matter has no significant interaction with other matter and that its particles have a low velocities. Any change in this assumption will directly effect gravitational clustering and the properties of large scale structure. Variation of the fundamental constants on cosmological scales can be another extension to the standard model of cosmology. We can also ask whether the general theory of relativity is valid at all epochs or not. Braneworld models and f(R) theories address this important issue. Topology of the universe is another open question which could add some more parameters to the standard model.

Beside all of the above points, there are two very important extensions to the standard model which are within our observational reach. The first one is **models of dark energy** with different properties in comparison with cosmological constant, and the second one is **non-power law form of the primordial perturbation spectrum**. We will have more detailed discussions about these two topics in the next subsections.

1.4.1 Dark energy candidates

In the last few years, the acceleration of the universe has been confirmed by many different cosmological observations including observations of type Ia supernovae, the cosmic microwave background and large scale structure. To accelerate the universe, we need an agent with a negative pressure and a positive density. This element is called **dark energy**. The cosmological constant, Λ, seems to be a perfect candidate for dark energy and indeed it is. Our current standard model of cosmology, ΛCDM consists of cold dark matter and cosmological constant as its main constituents. However despite the fact that ΛCDM has a very good consistency to most cosmological observations, there remain other candidates of dark energy with a very different theoretical motivation which can also give a good fit to the data. It is one of the main targets of the current cosmology to be able to distinguish between these different models of dark energy and to find the real agent of cosmic

acceleration. Most dark energy candidates have a varying equation of state and in this sense resemble another form of dark energy encountered in the early universe, namely inflation. Dark energy models proposed to account for the present cosmic acceleration include:
(i) **Cosmological constant** or Λ with $w = -1$.
(ii) **Quiescence** with constant equation of state, $w \equiv p_{DE}/\rho_{DE} =$ constant, the Λ ($w = -1$) is a special member of this class.
(iii) **Quintessence** these models are inspired by the simplest class of inflationary models of the early Universe and employ a scalar field rolling down a potential $V(\phi)$ to achieve late-time acceleration.
(iv) The **Chaplygin gas** model has the equation of state $p \propto -1/\rho$ and evolves as $\rho = \sqrt{A + B(1+z)^6}$. It therefore behaves like dark matter at early times ($z \gg 1$) and like the cosmological constant at late times. Chaplygin gas is a phenomenological model of dark energy which appears to be the simplest model attempting to unify dark energy and non-baryonic cold dark matter.
(v) **Phantom** dark energy ($w < -1$).
(vi) **Oscillating** dark energy.
(vii) Models with **interactions between dark energy and dark matter**.
(viii) **Scalar-tensor** dark energy models.
(ix) **Modified gravity** dark energy models in which the gravitational Lagrangian is changed from R to $F(R)$ where R is the scalar curvature and F is an arbitrary function.
(x) Dark energy driven by **quantum effects**.
(xi) Higher dimensional **braneworld** models in which acceleration is caused by the effects of the higher dimensions.
(xii) **Holographic** dark energy, etc.
See the reviews [19, 20, 37–39] for an exhaustive list of models and references. At the current state-of-the-art, all these different candidates of dark energy requires at least one new parameter whose value is set from observations.

In the second chapter of this thesis we introduce a model independent method of reconstruction of the properties of dark energy. We also propose three diagnostics of dark energy to distinguish between different dark energy models in a non-parametric and model independent manner.

1.4.2 Initial conditions and the primordial spectrum

A power law form of the primordial power spectrum is predicted by some of the earliest models of inflation [8–11]. Observational evidence also confirms that the form of the primordial spectrum is fairly close to this power law shape. But there is also some evidence (like the low power in the observed low l multiples and also some glitches at $l \approx 22$ and $l \approx 42$) which suggests the possibility of existence of features in power spectrum. The non-power law form of the primordial spectrum is not something unexpected in the context of inflation. In fact there are some inflationary scenarios which predict features in the primordial spectrum [22, 23, 139–144]. Any possible feature in the form of the primordial spectrum would be another extension to our standard model which would involve changing the set of basic cosmological parameters. In the following we will point to some of these inflationary scenarios which result in features in the form of the primordial spectrum. These models have been intentionally chosen to have a cut off in their power spectrum in order to give a better fit to the observed CMB data at low multiples.

Exponential Cutoff model(EC)

This model has a monotonic cutoff imposed on a scale-free power law spectrum. Such an infrared cutoff discussed and motivated by [21] leads to a spectrum of the form below

$$P(k) \;=\; A_s\, k^{n_s-1} \left[1 - e^{-(k/k_*)^\alpha}\right]. \tag{1.40}$$

The value of the parameter α was fixed ($\alpha = 3.35$) to approximately mimic the sharpness of the cutoff in a specific scenario (See KD model described later).

Starobinksy model(SB)

It was shown by Starobinsky [22] that if the effective inflationary potential has a 'singularity' in the form of a sharp change in the slope (a 'kink'), it can create an infrared suppression in the power spectrum of adiabatic perturbations at any chosen wavenumber k_*. The infrared cutoff is followed by a 'bump' that arises naturally as the first peak of a damped ringing. The effect of a kink at some point on the inflaton potential can be neatly expressed in terms of the analytic multiplicative transfer function applied on the underlying power spectrum $P_0(k)$ as

$$P(k) \;=\; P_0(k)\; \mathcal{D}^2(y, R_*). \tag{1.41}$$

In the simpler form we restrict $P_0(k)$ to be a simple power law. However, in general, $P_0(k)$ can be of any form allowed by models of scalar field driven inflation. The transfer function

$$\mathcal{D}^2(y, R_*) = [1 - 3\,(R_* - 1)\,\frac{1}{y}\,((1 - \frac{1}{y^2})\sin 2y + \frac{2}{y}\cos 2y) + \frac{9}{2}(R_* - 1)^2\frac{1}{y^2}(1 + \frac{1}{y^2})\times$$

$$(1 + \frac{1}{y^2} + (1 - \frac{1}{y^2})\cos 2y - \frac{2}{y}\sin 2y)]\,, \tag{1.42}$$

with $y = k/k_*$. R_* is the ratio of the slope $dV/d\phi$ which dictates the shape of the power spectrum, $V(\phi)$ being the inflaton potential of the scalar field ϕ. The power spectrum $P(k)$ in eqn (1.41) has a step-up feature (towards larger k) for $R_* < 1$ and a step-down feature for $R_* > 1$. An infrared cutoff is created when $R_* < 1$. This shape of the primordial power spectrum with a Starobinsky step not only mimics the sharp infrared cutoff but also subsequently produces the localized excess in power.

Pre-inflationary Kinetic Domination model(KD)

The observable inflationary epoch could be preceded by a period of fast rolling of the inflaton field, ϕ, leading to a pre-inflationary phase of kinetic domination. The difference of the vacuum in the kinetic domination (fast rolling) phase relative to the inflationary phase would imprint a feature in the power spectrum at large scales corresponding to the first modes that crossed out of the Hubble radius at the onset of inflation [21]. The feature is an infrared cutoff akin to that first shown by Vilenkin and Ford [23] for a radiation dominated pre-inflationary phase. If the scale corresponding to the current horizon exited the horizon very soon after the onset of inflation, then the feature could explain the observed suppression of power at the horizon scale. The form of primordial perturbations is given by

$$P(k) = \frac{H^2}{2\pi^2}\,k\,|\,A - B\,|^2 \tag{1.43}$$

where

$$A = \frac{e^{-ik/H}}{\sqrt{32\,H/\pi}}\left[\mathcal{H}_0^{(2)}\left(\frac{k}{2H}\right) - \left(\frac{H}{k} + i\right)\mathcal{H}_1^{(2)}\left(\frac{k}{2H}\right)\right]$$

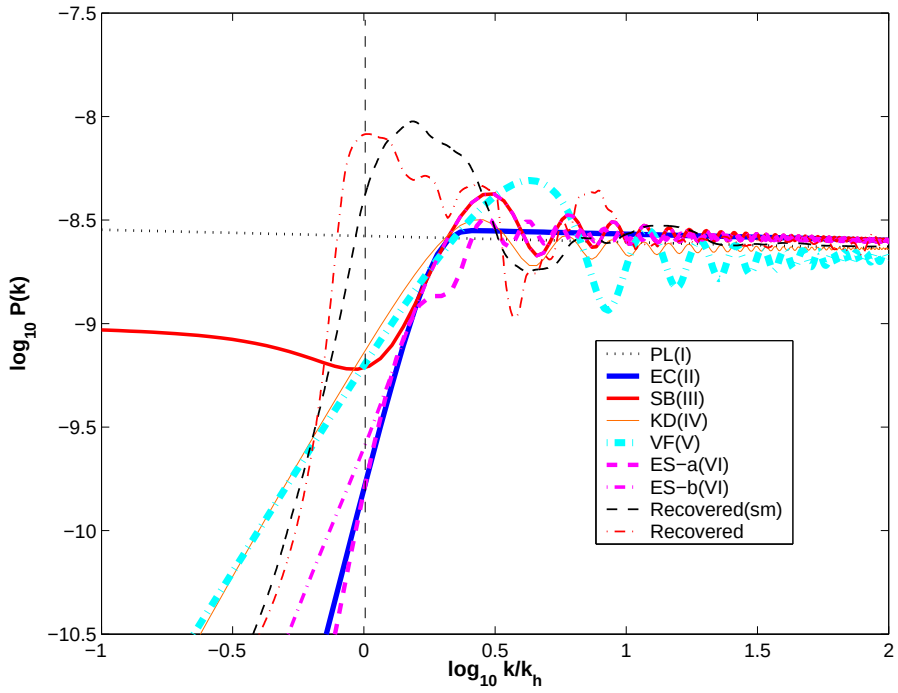

Figure 1.4: The class of primordial power spectra with features which have been introduced in this section are plotted. Here $k_h = 2\pi/\eta_o \approx 4.5 \times 10^{-4}$ Mpc^{-1}, is the wavenumber corresponding to the Horizon scale for best fit ΛCDM model. For comparison we also give the power spectrum recovered from WMAP data by direct deconvolution in the third chapter of this thesis ("Recovered") and wavelet smoothed version that retains the most prominent features ("Recovered(sm)") (figure is from [25]).

and

$$B = \frac{e^{ik/H}}{\sqrt{32\,H/\pi}}\left[\mathcal{H}_0^{(2)}\left(\frac{k}{2H}\right) - \left(\frac{H}{k} - i\right)\mathcal{H}_1^{(2)}\left(\frac{k}{2H}\right)\right].$$

Here H denotes the (physical) Hubble parameter during inflation while $\mathcal{H}_0^{(2)}$ and $\mathcal{H}_1^{(2)}$ denote the Hankel function of the second kind with order 0 and 1, respectively.

Pre-inflationary Radiation domination model(VF)

For a pre-inflationary radiation dominated epoch the power spectrum was given by Vilenkin and Ford [23] as follows (referred to as 'VF' model here)

$$P(k) = A_s\, k^{1-n_s}\,\frac{1}{4y^4}\left|e^{-2iy}(1+2iy) - 1 - 2y^2\right|^2, \tag{1.44}$$

where $y = k/k_*$. The VF power spectrum can also provide an infrared cutoff with the required 'bump' after it. The infrared cutoff here is not as sharp as the one arising from kinetic domination in the pre-inflationary phase. The cutoff scale k_* is set by the Hubble parameter at the onset of inflation. Here too, the current horizon scale crosses the Hubble radius very close to the onset of inflation.

We emphasize here that there are many other inflationary scenarios that can generate features in the form of the primordial spectrum and the above examples are just a small sample for these scenarios. For instance in [26], an inflationary scenario is proposed which gives rise to a local running of the spectral index. [3]

This thesis focuses on reconstruction of the expansion history of the universe and the properties of dark energy and also direct reconstruction of the primordial power spectrum. In chapter two we introduce a novel method of reconstruction of the expansion history of the universe and apply this method to simulated and real data. In the second chapter we also introduce three diagnostics of dark energy which help to distinguish between different models of dark energy. Chapter three relates to our study on direct reconstruction of the primordial perturbation spectrum from CMB data. We have improved the Richardson-Lucy deconvolution method to make it suitable for our studies and have applied our method to WMAP CMB data. Conclusion are drawn in the fourth chapter and the thesis ends with a bibliography.

[3] In writing this introduction I found the following books and reviews very helpful [17,19,20,34–36].

Chapter 2

Model Independent Reconstruction of the Properties of Dark Energy

This chapter of the thesis includes two major sections. The first section discusses non-parametric reconstruction of the expansion history of the universe through a smoothing method which we have developed and successfully applied on simulated and real data. The second part is about three new diagnostics of dark energy which we have introduced to the cosmological community to distinguish between different models of dark energy.

2.1 Non Parametric Reconstruction of the Expansion History of the Universe

The nature of dark energy has been the subject of much debate over the past decade (for reviews see [19, 20, 37–40]). The supernova (SNe) type Ia data, which gave the first indications of the accelerated expansion of the universe, are expected to throw further light on this intriguing question as their quality steadily improves. While the number of SNe available to us has increased two-fold over the past couple of years (at present there are about 300 SNe between redshifts of 0 and 1.75, with 10 SNe above a redshift of unity) [12,27,41–47], the SNe data are still not of a quality to firmly distinguish different models of dark energy. In this connection, an important role in our quest for a deeper understanding of the nature of dark energy has been

played by the 'reconstruction program'. Commencing from the first theoretical exposition of the reconstruction idea – [48–50], and [51] which applied it to an early supernova data set– there have been many attempts to reconstruct the properties of dark energy directly from observational data without assuming any particular microscopic/phenomenological model for the former. When using SNe data for this purpose, the main obstacle is the necessity to: (i) differentiate the data once to pass from the luminosity distance d_L to the Hubble parameter $H(t) \equiv \dot{a}(t)/a(t)$ and to the effective energy density of dark energy ρ_{DE}, (ii) differentiate the data a second time in order to obtain the deceleration parameter $q \equiv -\ddot{a}a/\dot{a}^2$, the dark energy effective pressure p_{DE}, and the equation of state parameter $w(t) \equiv p_{DE}/\rho_{DE}$. Here, $a(t)$ is the scale factor of a Friedmann-Robertson-Walker (FRW) isotropic cosmological model which we further assume to be spatially flat, as predicted by the simplest variants of the inflationary scenario of the early Universe and confirmed by observational CMB data.

To get around this obstacle, some kind of smoothing of d_L data with respect to its argument – the redshift $z(t)$ – is needed. One possible way is to parameterize the quantity which is of interest ($H(z)$, $w(z)$, etc.) by some functional form containing a few free parameters and then determine the value of these parameters which produce the best fit to the data. This implies an implicit smoothing of d_L with a characteristic smoothing scale defined by the number of parameters, and with a weight depending on the form of parameterization. Different parameterizations have been used for: d_L [49, 51, 52], $H(z)$ [53, 54, 68], $w(z)$ [55–65] and $V(z)$ [66, 67]. In [49], a polynomial expansion of the luminosity distance was used to reconstruct the equation of state. However, [56] showed this ansatz to be inadequate since it needed an arbitrarily large number of parameters to fit even the simplest ΛCDM equation of state. They proposed instead a polynomial ansatz for the equation of state which worked somewhat better. In [51] a rational Padè-type ansatz for d_L was proposed, which gave good results. In recent times there have been many more attempts at parameterizing dark energy. In [55] and [60] an ansatz of the form $w = w_0 + w_a(1 - a)$ was suggested for the equation of state. [59] suggested a four-parameter ansatz for the equation of state. [53] proposed a slightly different approach in which the dark energy density was expanded in a polynomial ansatz, the properties of which were examined in [54, 68, 68]. See [69–71] for a summary of different approaches to the reconstruction program and for a more extensive list of references. However it is necessary to point out that the current SNe data are not of a quality that could allow us to unambiguously differentiate ΛCDM from evolving

dark energy. That is why our initial focus in this chapter will be on better quality data (from the SNAP experiment) which should be able to successfully address this important issue.

A non-parametric smoothing procedure involves directly smoothing either d_L, or any other quantity defined within redshifts bins, with some characteristic smoothing scale. Different forms of this approach have been elaborated in [72–77]. One of the advantages of this approach is that the dependence of the results on the size of the smoothing scale becomes explicit. We emphasize again that the present consensus seems to be that, while the cosmological constant remains a good fit to the data, more exotic models of dark energy are by no means ruled out (though their diversity has been significantly narrowed already). Thus, until the quality of data improves dramatically, the final judgment on the nature of dark energy cannot yet be pronounced.

In this thesis, we develop a new reconstruction method which formally belongs to the category of non-parametric methods, and which is complementary to the approach of fitting a parametric ansatz to the dark energy density or the equation of state. Most of the papers using the non-parametric approach cited above exploited a kind of top-hat smoothing in redshift space. Instead, we follow a procedure which is well known and frequently used in the analysis of large-scale structure [78, 79]; namely, we attempt to smooth noisy data directly using a Gaussian smoothing function. Then, from the smoothed data, we calculate different cosmological functions and, thus, extract information about dark energy. This method allows us to avoid additional noise due to sharp borders between bins. Furthermore, since our method does not assume any definite parametric representation of dark energy, it does not bias results towards any particular model. We therefore expect this method to give us model-independent estimates of cosmological functions, in particular, the Hubble parameter $H(z) \equiv \dot{a}(t)/a(t)$. On the basis of data expected from the SNAP satellite mission, we first show that the Gaussian smoothing ansatz proposed in this thesis can successfully distinguish between rival cosmological models and help shed light on the nature of dark energy. Then we apply our method on the current available supernovae data and we reconstruct the properties of dark energy in a non parametric and model independent manner.

2.1.1 Methodology: Smoothing Method

It is useful to recall that, in the context of structure formation, it is often advantageous to obtain a smoothed density field $\delta^S(\mathbf{x})$ from a fluctuating 'raw' density field,

$\delta(\mathbf{x}')$, using a low pass filter F having a characteristic scale R_f [78]

$$\delta^S(\mathbf{x}, R_f) = \int \delta(\mathbf{x}')F(|\mathbf{x}-\mathbf{x}'|; R_f)\, d\mathbf{x}' \ . \tag{2.1}$$

Commonly used filters include: (i) the 'top-hat' filter, which has a sharp cutoff $F_{\rm TH} \propto \Theta(1-|\mathbf{x}-\mathbf{x}'|/R_{\rm TH})$, where Θ is the Heaviside step function ($\Theta(z) = 0$ for $z \leq 0$, $\Theta(z) = 1$ for $z > 0$) and (ii) the Gaussian filter $F_{\rm G} \propto \exp(-|\mathbf{x}-\mathbf{x}'|^2/2R_{\rm G}^2)$. For our purpose, we shall find it useful to apply a variant of the Gaussian filter to reconstruct the properties of dark energy from supernova data. In other words, we apply Gaussian smoothing to supernova data (which is of the form $\{\ln d_L(z_i), z_i\}$) in order to extract information about important cosmological parameters such as $H(z)$ and $w(z)$. The smoothing algorithm calculates the luminosity distance at any arbitrary redshift z to be

$$\ln d_L(z,\Delta)^{\rm s} = \ln\ d_L(z)^g + N(z)\sum_i [\ln d_L(z_i) - \ln\ d_L(z_i)^g] \times \exp\left[-\frac{\ln^2\left(\frac{1+z_i}{1+z}\right)}{2\Delta^2}\right],$$

$$N(z)^{-1} = \sum_i \exp\left[-\frac{\ln^2\left(\frac{1+z_i}{1+z}\right)}{2\Delta^2}\right] . \tag{2.2}$$

Here, $\ln d_L(z,\Delta)^{\rm s}$ is the smoothed luminosity distance at any redshift z which depends on luminosity distances of each SNe event with the redshift z_i, and $N(z)$ is a normalization parameter. Note that the form of the kernel bears resemblance to the lognormal distribution (such distributions find application in the study of cosmological density perturbations, [80]). The quantity $\ln d_L(z)^g$ represents a guessed background model which we subtract from the data before smoothing it. This approach allows us to smooth noise only, and not the luminosity distance. After noise smoothing, we add back the guess model to recover the luminosity distance. This procedure is helpful in reducing noise in the results. Since we do not know which background model to subtract, we may take a reasonable guess that the data should be close to ΛCDM and use $d_L(z)^g = d_L(z)^{\Lambda\rm CDM}$ as a first approximation and then use a boot-strapping method to find successively better guess models. We shall discuss this issue in greater detail in the section 2.1.2. Having obtained the smoothed luminosity distance, we differentiate once to obtain the Hubble parameter $H(z)$ and

Table 2.1: Expected number of supernovae per redshift bin from the SNAP experiment

Δz	0.1–0.2	0.2–0.3	0.3–0.4	0.4–0.5	0.5–0.6	0.6–0.7	0.7–0.8	0.8–0.9
N	35	64	95	124	150	171	183	179

Δz	0.9–1.0	1.0–1.1	1.1–1.2	1.2–1.3	1.3–1.4	1.4–1.5	1.5–1.6	1.6–1.7
N	170	155	142	130	119	107	94	80

twice to obtain the equation of state of dark energy $w(z)$, using the formula

$$H(z) = \left[\frac{d}{dz}\left(\frac{d_L(z)}{1+z}\right)\right]^{-1} , \tag{2.3}$$

$$w(z) = \frac{[2(1+z)/3]\, H'/H - 1}{1 \;-\; (H_0/H)^2 \Omega_m\, (1+z)^3}. \tag{2.4}$$

The results will clearly depend upon the value of the scale Δ in eqn (2.2). A large value of Δ produces a smooth result, but the accuracy of reconstruction worsens, while a small Δ gives a more accurate, but noisy result. Note that, for $|z - z_i| \ll 1$, the exponent in eqn (2.2) reduces to the form $-(z - z_i)^2/2\Delta^2(1+z)^2$. Thus, the effective Gaussian smoothing scale for this algorithm is $\Delta(1+z)$. We expect to obtain an optimum value of Δ for which both smoothness and accuracy are reasonable.

To check our method, we use data simulated according to the SuperNova Acceleration Probe (SNAP) experiment. This space-based mission is expected to observe close to 6000 supernovae, of which about 2000 supernovae can be used for cosmological purposes [81]. We propose to use a distribution of 1998 supernovae between redshifts of 0.1 and 1.7 obtained from [81]. This distribution of 1998 supernovae is shown in table 2.1. Although SNAP will not be measuring supernovae at redshifts below $z = 0.1$, it is not unreasonable to assume that, by the time SNAP comes up, we can expect high quality data at low redshifts from other supernova surveys such as the Nearby SN Factory [1]. Hence, in the low redshift region $z < 0.1$, we add 25 more supernovae of equivalent errors to the SNAP distribution, so that our data sample now consists of 2023 supernovae . Using this distribution of data, we check whether the method is successful in reconstructing different cosmological parameters, and also if it can help discriminate different models of dark energy.

[1] http://snfactory.lbl.gov

2.1.2 Results from simulated SNAP data

In this section we show the results obtained when our smoothing scheme is applied to data expected from the SNAP experiment. We simulate 1000 realizations of data using the SNAP distribution with the error in the luminosity distance given by $\sigma_{\ln d_L} = 0.07$ – the expected error for SNAP. We also consider the possible effect of weak-lensing on high redshift supernovae by adding an uncertainty of $\sigma_{lens}(z) \approx 0.46(0.00311 + 0.08687z - 0.00950z^2)$ (as in [77]). Initially, we use a simple model of dark energy when simulating data – an evolving model of dark energy with $w = -a/a_0 = -1/(1+z)$ and $\Omega_m = 0.3$. It will clearly be of interest to see whether this model can be reconstructed accurately and discriminated from ΛCDM using this method. From the SNAP distribution, we obtain smoothed data at 2000 points taken uniformly between the minimum and maximum of the distributions used. Once we are assured of the efficacy of our method, we shall also attempt to reconstruct other models of dark energy. Among these, one is the standard cosmological constant (ΛCDM) model with $w = -1$. The other is a model with a constant equation of state, $w = -0.5$. Such models with constant equation of state are known as "quiessence models" of dark energy [69]. These three models are complementary to each other. For the ΛCDM model, the equation of state is constant at $w = -1$, w remains constant at -0.5 for the quiessence model and for the evolving model, $w(z)$ varies rapidly, increasing in value from $w_0 = -1$ at the present epoch to $w \simeq 0$ at high redshifts.

The first issue we need to consider is that of the guess model. As mentioned earlier, the guess model in eqn (2.2) is arbitrary. Using a guess model will naturally cause the results to be somewhat biased towards the guess model at low and high redshifts where there is paucity of data. Therefore we use an iterative method to estimate the guess model from an initial guess.

Iterative process to obtain Guess model

To estimate the guess model for our smoothing scheme, we use the following iterative method. We start with a simple cosmological model, such as ΛCDM, as our initial guess model– $\ln d_L^{g0} = \ln d_L^{\Lambda\mathrm{CDM}}$. The result obtained from this analysis, $\ln d_L^1$, is expected to be closer to the real model than the initial guess. We now use this result as our next guess model– $\ln d_L^{g1} = \ln d_L^1$ and obtain the next result $\ln d_L^2$. With each iteration, we expect the guess model to become more accurate, thus giving a result that is less and less biased towards the initial guess model used. A few points about the iterative method should be noted here.

- Using different models for the initial guess does not affect the final result provided the process is iterated several times. For example, if we use a $w = -1/(1+z)$ 'metamorphosis' model to simulate the data and use either ΛCDM or the $w = -0.5$ quiessence model as our initial guess, the results for the two cases converge by few iterations.

- Using a very small value of Δ will result in a accurate but noisy guess model, therefore after a few iterations, the result will become too noisy to be of any use. Therefore, we should use a large Δ for this process in order to obtain smoother results.

- The bias of the final result will decrease with each iteration, since with each iteration we get closer to the true model. The bias decreases non-linearly with the number of iterations M. Generally, after about 10 iterations, for moderate values of Δ, the bias is acceptably small. Beyond this, the bias still decreases with the number of iterations but the decrease is negligible while the process takes more time and results in larger errors on the parameters.

- It is important to choose a value of Δ which gives a small value of bias and also reasonably small errors on the derived cosmological parameters. To estimate the value of Δ in eqn (2.2), we consider the following relation between the reconstructed results, quality and quantity of the data and the smoothing parameters. One can show that the relative error bars on $H(z)$ scale as [82]

$$\frac{\delta H}{H} \propto \frac{\sigma}{N^{1/2}\Delta^{3/2}} \ , \tag{2.5}$$

  where N is the total number of supernovae (for approximately uniform distribution of supernovae over the redshift range) and σ is the noise of the data. From the above equation we see that a larger number of supernovae or larger width of smoothing, Δ, will decrease the error bars on reconstructed H, but as we shall show in appendix A, the bias of the method is approximately related to Δ^2. This implies that, by increasing Δ we will also increase the bias of the results. We attempt to estimate Δ such that the error bars on H be of the same order as σ, which is a reasonable expectation. If we consider a single iteration of our method, then for $N \simeq 2000$ we get $\Delta_0 \simeq N^{-1/3} \simeq 0.08$. However, with each iteration, the errors on the parameters will increase. Therefore using this value of Δ when we use an iterative process to find the guess model will result

in such large errors on the cosmological parameters as to render the reconstruction exercise meaningless. It shall be shown in appendix A that at the M-th iteration, the error on $\ln d_L$ will be approximately $\delta_M(\ln d_L) \simeq \sqrt{M}\delta_0(\ln d_L)$. The error on $\ln d_L$ scales as $1/\Delta$. We would like the errors after M iterations to be commensurate with the optimum errors obtained for a single iteration, Δ_0, so we require $\Delta_{\rm optimal} \simeq \sqrt{M}\Delta_0$. Therefore, if we wish to stop the boot-strapping after 10 iterations, then $\Delta_{\rm optimal} \simeq 3\Delta_0 \simeq 0.24$. This is the optimal value of Δ we shall use for best results for our smoothing procedure.

Considering all these factors, we use a smoothing scale $\Delta = 0.24$ for the smoothing procedure of eqn (2.2) with a iterative method for finding the guess model (with ΛCDM as the initial guess). The boot-strapping is stopped after 10 iterations. We will see that the results reconstructed using these parameters do not contain noticeable bias and the errors on the parameters are also satisfactory.

Figure 2.1 shows the reconstructed $H(z)$ and $w(z)$ with 1σ errors for the $w = -1/(1+z)$ evolving model of dark energy. From this figure we can see that the Hubble parameter is reconstructed quite accurately and can successfully be used to differentiate the model from ΛCDM. The equation of state, however, is somewhat noisier. There is also a slight bias in the equation of state at low and high redshifts. Since the $w = -1/(1+z)$ model has an equation of state which is very close to $w = -1$ at low redshifts, we see that $w(z)$ cannot discriminate ΛCDM from the fiducial model at $z \leq 0.2$ at the 1σ confidence level.

Age of the Universe

We may also use this smoothing scheme to calculate other cosmological parameters of interest such as the age of the universe at a redshift z:

$$t(z) = H_0^{-1} \int_z^\infty \frac{dz'}{(1+z')H(z')} \ . \tag{2.6}$$

In this case, since data is available only up to redshifts of $z \simeq 1.7$, it will not be possible to calculate the age of the universe. Instead, we calculate the look-back time at each redshift–

$$T(z) = t(z=0) - t(z) = H_0^{-1} \int_0^z \frac{dz'}{(1+z')H(z')} \ . \tag{2.7}$$

Figure 2.2 shows the reconstructed $T(z)$ with 1σ errors for the $w = -1/(1+z)$ 'metamorphosis' model using the SNAP distribution. For this model the current

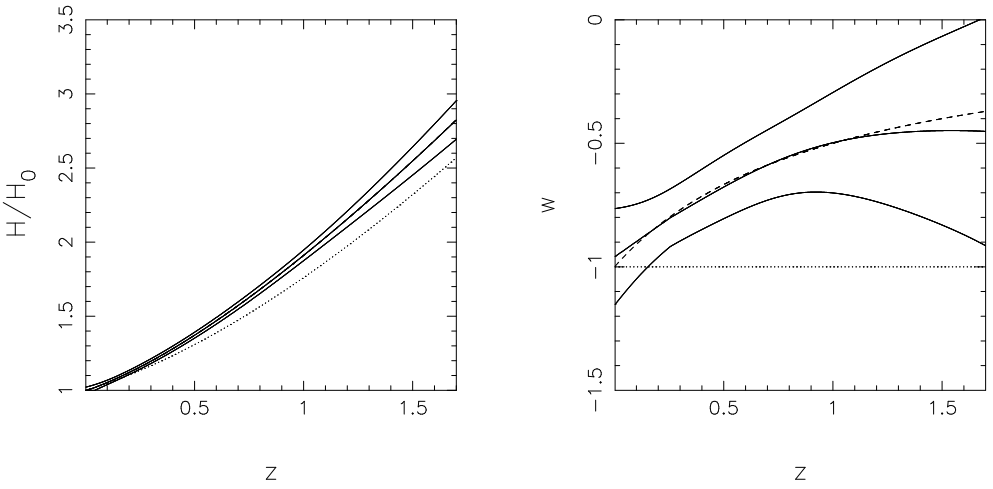

Figure 2.1: The smoothing scheme of eqn (2.2) is used to determine $H(z)$ and $w(z)$ from 1000 realizations of the SNAP dataset. The smoothing scale is $\Delta = 0.24$. The dashed line in each panel represents the fiducial $w = -1/(1+z)$ 'metamorphosis' model while the solid lines show the mean Hubble parameter (left), the mean equation of state (right), and 1σ limits around these quantities. The dotted line in both panels is ΛCDM. Note that the mean Hubble parameter is reconstructed so accurately that the fiducial model (dashed line) is not visible in the left panel.

age of the universe is about 13 Gyrs and the look-back time at $z \simeq 1.7$ is about 9 Gyrs for a Hubble parameter of $H_0 = 70$ km/s/Mpc. We see that the look-back time is reconstructed extremely accurately. Using this method we may predict this parameter with a high degree of success and distinguish between the fiducial look-back time and that for ΛCDM even at the 10σ confidence level. Indeed any cosmological parameter which can be obtained by integrating the Hubble parameter will be reconstructed without problem, since integrating involves a further smoothing of the results.

Looking at these results, we draw the conclusion that the method of smoothing supernova data can be expected to work quite well for future SNAP data as far as the Hubble parameter is concerned. Using this method, we may reconstruct the Hubble parameter and therefore the expansion history of the universe accurately. We find that the method is very efficient in reproducing $H(z)$ to an accuracy of $\leq 2\%$ within the redshift interval $0 < z < 1$, and to $\leq 4\%$ at $z \simeq 1.7$, as demonstrated in figure 2.1. Furthermore, using the Hubble parameter, one may expect to discriminate between different families of models such as the metamorphosis model $w = -1/(1+z)$ and ΛCDM. This method also reproduces very accurately the look-back time for a given model, as seen in figure 2.2. It reconstructs the look-back time to an accuracy of

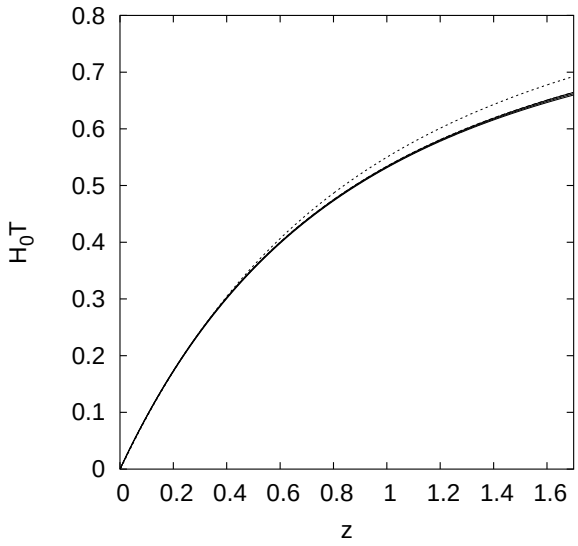

Figure 2.2: The smoothing scheme of eqn (2.2) is used to determine the look-back time of the universe, $T(z) = t(0) - t(z)$, from 1000 realizations of the SNAP dataset for a $w = -1/(1+z)$ 'metamorphosis' model. The smoothing scale is $\Delta = 0.24$. The solid lines show the mean look-back time and the 1σ limits around it. The look-back time for the fiducial model matches exactly with the mean for the smoothing scheme. The dotted line shows the ΛCDM model.

$\leq 0.2\%$ at $z \simeq 1.7$.

Reducing noise through Double Smoothing

As we saw in the preceding subsection, the method of smoothing supernova data to extract information on cosmological parameters works very well if we employ the first derivative of the data to reconstruct the Hubble parameter. It also works reasonably for the second derivative, which is used to determine $w(z)$, but the errors on $w(z)$ are somewhat large. In this section, we examine a possible way in which the equation of state may be extracted from the data to give slightly better results.

The noise in each parameter translates into larger noise levels on its successive derivatives. We have seen earlier that, using the smoothing scheme eqn (2.2), one can obtain $H(z)$ from the smoothed $d_L(z)$ fairly successfully. However, small noises in $H(z)$ propagate into larger noises in $w(z)$. Therefore, it is logical to assume that if $H(z)$ were smoother, the resultant $w(z)$ might also have smaller errors. So, we attempt to smooth $H(z)$ a second time after obtaining it from $d_L(z)$. The procedure in this method is as follows – first, we smooth noisy data $\ln d_L(z)$ to obtain $\ln d_L(z)^{\rm s}$ using eqn (2.2). We differentiate this to find $H(z)^{\rm s}$ using eqn (2.3). We then further

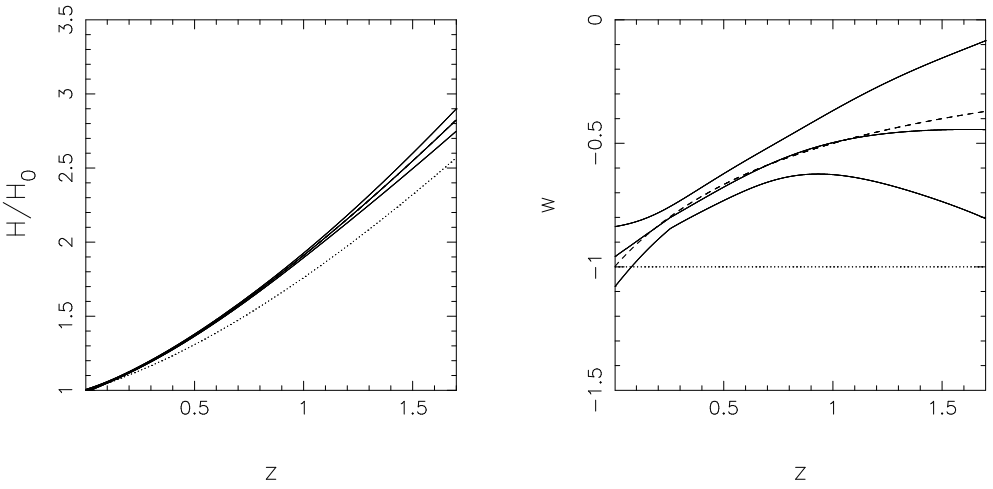

Figure 2.3: The double smoothing scheme of eqns (2.2) and (2.8) has been used to obtain $H(z)$ and $w(z)$ from 1000 realizations of the SNAP dataset. The smoothing scale is $\Delta = 0.24$. The dashed line in each panel represents the fiducial $w = -1/(1+z)$ 'metamorphosis' model while the solid lines represent the mean and 1σ limits around it. The dotted line in both panels is ΛCDM. In the left panel $H(z)$ for the fiducial model matches exactly with the mean for the smoothing scheme.

smooth this Hubble parameter by using the same smoothing scheme at the new redshifts

$$H(z,\Delta)^{s_2} = H(z)^g + N(z)\sum_i [H(z_i)^s - H(z_i)^g] \times \exp\left[-\frac{\ln^2\left(\frac{1+z_i}{1+z}\right)}{2\Delta^2}\right],$$

$$N(z)^{-1} = \sum_i \exp\left[-\frac{\ln^2\left(\frac{1+z_i}{1+z}\right)}{2\Delta^2}\right]. \tag{2.8}$$

We then use this $H(z,\Delta)^{s_2}$ to obtain $w(z)$ using eqn (2.4). This has the advantage of making $w(z)$ less noisy than before, while using the same number of parameters. However, repeated smoothing can also result in the loss of information.

The result for the SNAP distribution using this double smoothing scheme for the $w = -1/(1+z)$ model is shown in figure 2.3. We use $\Delta = 0.24$ for smoothing both $\ln d_L(z)$ and $H(z)$. Comparing with figure 2.1, we find that there is an improvement in the reconstruction of $H(z)$ as well as $w(z)$. Thus, errors on the Hubble parameter decrease slightly and errors on $w(z)$ also become somewhat smaller.

We now explore this scheme further for other models of dark energy. We first consider a $w = -1$ ΛCDM model. In figure 2.4, we show the results for this model. We find that the Hubble parameter accurately reconstructed and even w is well

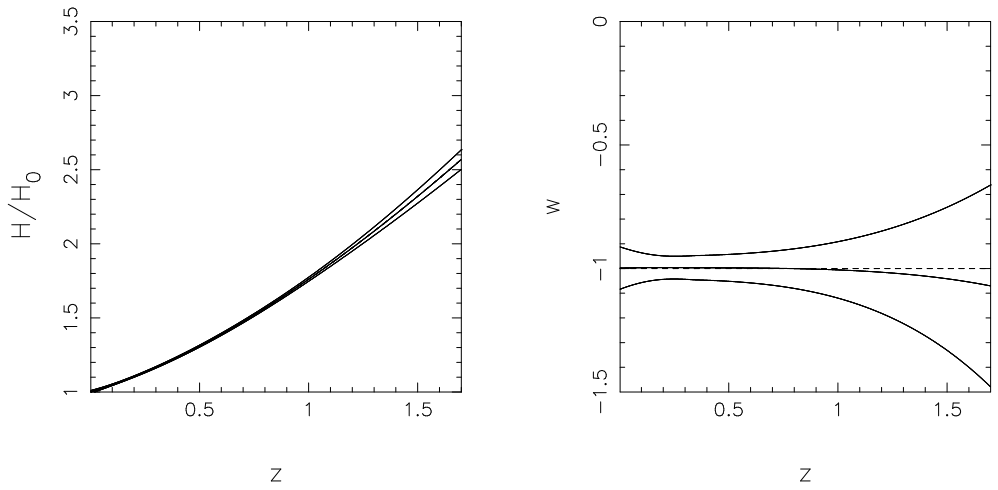

Figure 2.4: The double smoothing scheme of eqns (2.2) and (2.8) has been used to obtain $H(z)$ and $w(z)$ from 1000 realizations of the SNAP dataset. The smoothing scale is $\Delta = 0.24$. The dashed line in each panel represents the fiducial ΛCDM model with $w = -1$ while the solid lines represent the mean and 1σ limits around it. In the left panel $H(z)$ for the fiducial model matches exactly with the mean for the smoothing scheme.

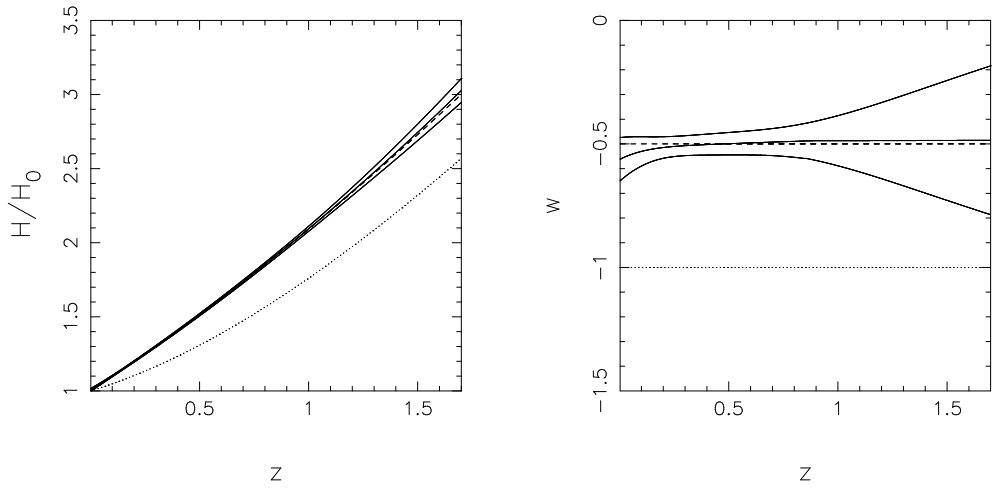

Figure 2.5: The double smoothing scheme of eqns (2.2) and (2.8) has been used to obtain $H(z)$ and $w(z)$ from 1000 realizations of the SNAP dataset. The smoothing scale is $\Delta = 0.24$. The dashed line in each panel represents the fiducial quiessence model with $w = -0.5$ while the solid lines represent the mean and 1σ limits around it. The dotted line is ΛCDM.

reconstructed, with a little bias at high redshift. The next model we reconstruct is a $w = -0.5$ quiessence model. The results for double smoothing are shown in figure 2.5. There is a little bias for this model at the low redshifts, although it is still well within the error bars.

We note that in all three cases, a slight bias is noticeable at low or high redshifts. This is primarily due to edge effects– since at low (high) redshift, any particular point will have less (more) number of supernovae to the left than to the right. Even by estimating the guess model through an iterative process, it is difficult to completely get rid of this effect. In order to get rid of this effect, we would require to use much larger number of iterations for the guess model, but this would result in very large errors on the parameters. However, this bias is so small as to be negligible and cannot affect the results in any way.

Looking at these three figures, we can draw the following conclusions. The Hubble parameter is quite well reconstructed by the method of double smoothing in all three cases while the errors on the equation of state also decrease. At low and high redshifts, a very slight bias persists. In appendix B we have shown that by using a proper variable width of smoothing it is possible to decrease the bias at the two tails significantly. Despite this, the equation of state is reconstructed quite accurately. Also, since the average error in $w(z)$ is somewhat less than that in the single smoothing scheme (figure 2.1), the equation of state may be used with better success in discriminating different models of dark energy using the double smoothing procedure.

2.1.3 Cosmological Reconstruction applied to other physical models of Dark Energy

In this subsection we draw the readers attention to the dangers encountered during cosmological reconstruction of a typical dark energy models. There are currently two plausible ways of making the expansion of the universe accelerate at late times. The first approach depends on changing the matter sector of the Einstein equations. Examples of this approach are the quintessence fields. A completely different approach has shown that it is possible to obtain an accelerating universe through modifying the gravity sector (see, for instance, [83–91] and references therein). In these models, dark energy should not be treated as a fluid or a field. Instead, it may be better dubbed as 'geometric dark energy'. Indeed the DGP model [91] can cause the universe to accelerate even in the absence of a physical dark energy component.

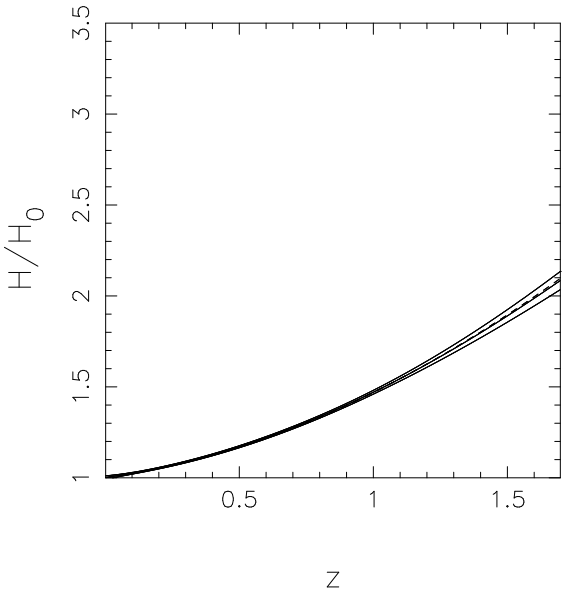

Figure 2.6: The reconstructed Hubble parameter $H(z)$ for the braneworld model, eqn (2.9) for 1000 realizations of the SNAP dataset. We use the double smoothing scheme of eqns (2.2) and (2.8) with $\Delta = 0.24$. The dashed line represents the fiducial $\Omega_m = 0.3, \Omega_l = 1, \Omega_{l_b} = 0$ braneworld model while the solid lines represent the mean and 1σ limits around it. We note that the Hubble parameter is very well reconstructed for the braneworld model.

As pointed out in [69, 90], the equation of state is not a fundamental quantity for geometric dark energy. E.g., using $w(z)$ in the reconstruction of such models may result in very strange results, including, for instance, singularities in the equation of state. [2]

As an example, we consider the braneworld dark energy model proposed in [85] described by the following set of equations for a flat universe :

$$\frac{H^2(z)}{H_0^2} = \Omega_m(1+z)^3 + \Omega_\sigma + 2\Omega_l - 2\sqrt{\Omega_l}\,\sqrt{\Omega_m(1+z)^3 + \Omega_\sigma + \Omega_l + \Omega_{l_b}}$$

[2] A very simple model which has a well-behaved $q(z)$ but singular $w(z)$ is a model which has, in addition to the cosmological constant, a second dark energy component disguised as a spatial curvature term– $H^2(z)/H_0^2 = \Omega_m(1+z)^3 + \Omega_X(1+z)^2 + \Omega_\Lambda$. If we assume that $\Omega_m = 0.3, \Omega_X = -0.05, \Omega_\Lambda = 0.75$, then $w(z)$ becomes singular when $\Omega_X(1+z)^2 + \Omega_\Lambda = 0$, i.e., at $z \simeq 2.8$. Although this property of $w(z)$ can be easily understood physically and rests in the fact that it is an 'effective' equation of state for the combination of DE fluids, nevertheless any reasonable parameterization of $w(z)$ will clearly experience difficulty in reproducing this behavior. An effective equation of state with a similar 'pole-like' divergence is frequently encountered in braneworld models of dark energy [85,92] as well as in holographic models [93].

$$\Omega_\sigma = 1 - \Omega_m + 2\sqrt{\Omega_l(1+\Omega_{\text{ł}_b})}\ , \tag{2.9}$$

where the densities Ω are defined as :

$$\Omega_m = \frac{\rho_{0m}}{3m^2H_0^2},\quad \Omega_\sigma = \frac{\sigma}{3m^2H_0^2},\quad \Omega_l = \frac{1}{l_c^2H_0^2},\quad \Omega_{\text{ł}_\text{b}} = -\frac{\text{ł}_\text{b}}{6H_0^2}\ , \tag{2.10}$$

$l_c = m^2/M^3$ being a new length scale (m and M refer respectively to the four and five dimensional Planck masses), ł_b the bulk cosmological constant and σ the brane tension. In this section we have used $\hbar = c = 1$. On short length scales $r \ll l_c$ and at early times, one recovers general relativity, whereas on large length scales $r \gg l_c$ and at late times brane-related effects become important and may lead to the acceleration of the universe. The 'effective' equation of state for this braneworld model is given by

$$\rho = \frac{3H^2}{8\pi G}(1-\Omega_\text{m}(z)),\quad p = \frac{H^2}{4\pi G}(q(z)-1/2)\quad w_\text{eff} = \frac{p}{\rho} = \frac{q(z)-1/2}{3(1-\Omega_\text{m}(z))}\ . \tag{2.11}$$

It is obvious that the effective equation of state in this braneworld model may become singular if $\Omega_\text{m}(z) \equiv \Omega_m(1+z)^3H_0^2/H^2(z)$ becomes unity. This does not signal any inherent pathologies in the model however. We should remember that the acceleration of the universe in this model is due to modification of the expansion of the universe at late times due to extra-dimensional effects. Hence it is not very appropriate to describe dark energy by an equation of state for such a model. However, it would be interesting to see if the singularity in the effective w for this model can be recovered by our smoothing method.

We attempt to reconstruct an $\Omega_m = 0.3, \Omega_l = 1, \Omega_{\text{ł}_b} = 0$ braneworld model which is a good fit to the current supernova data [94]. We simulate data according to SNAP and obtain results for the double smoothing method with $\Delta = 0.24$. In figure 2.6, we show the reconstructed Hubble parameter for this reconstruction. We see that the Hubble parameter is very well reconstructed and shows no pathological behavior.

We now obtain the equation of state of dark energy for this model. For this purpose, we also use an ansatz for the equation of state as suggested by [55] and [60] (the CPL fit)

$$w(z) = w_0 + \frac{w_1 z}{1+z}\ . \tag{2.12}$$

The results are shown in figure 2.7. We find, as expected, that it is impossible

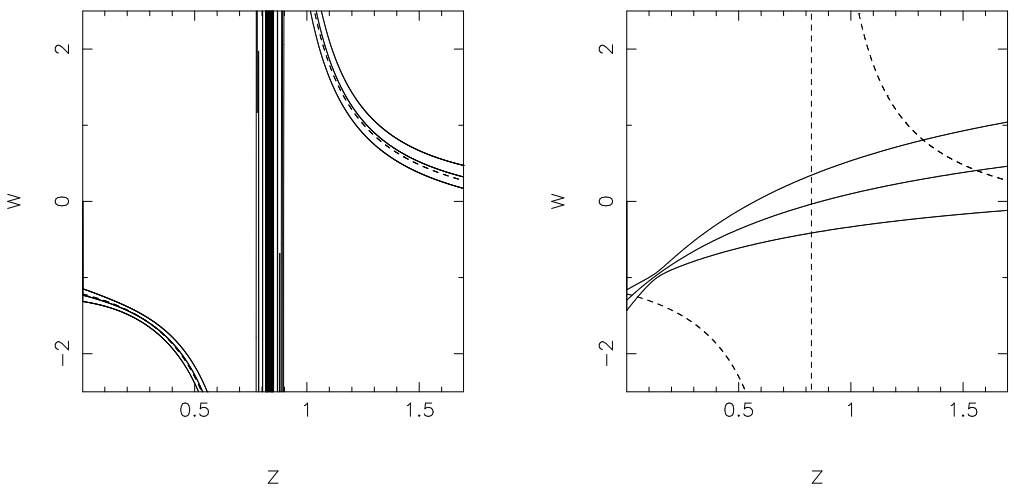

Figure 2.7: Reconstructed equation of state for the braneworld model, eqn (2.9), for 1000 realizations of the SNAP dataset. The left panel shows results for the double smoothing scheme of eqns (2.2) and (2.8) with $\Delta = 0.24$ while the right panel uses the ansatz eqn (2.12) to reconstruct the equation of state. The dashed line in each panel represents the fiducial $\Omega_m = 0.3, \Omega_l = 1, \Omega_{k_b} = 0$ braneworld model while the solid lines represent the mean and 1σ limits around it.

to catch the singularity in the equation of state at $z \simeq 0.8$ using an equation of state ansatz. Of course, one may try and improve upon this somewhat dismal picture by introducing fits with more free parameters. However, it is well known that the presence of more degrees of freedom in the fit leads to a larger degeneracy (between parameters) and hence to larger errors of reconstruction [56]. In contrast to this approach, when we reconstruct the equation of state using the smoothing scheme (which does not presuppose any particular behavior of the equation of state), the Hubble parameter is reconstructed very accurately and hence the 'effective' equation of state for this model is also reconstructed well, as shown in figure 2.7. From this figure we see a clear evidence of the singularity at $z \simeq 0.8$. Thus to obtain maximum information about the equation of state, especially in cases where the dark energy model is very different from the typical quintessence-like models, it may be better to reconstruct the Hubble parameter or the dark energy density first.

Therefore, we find that the smoothing scheme, which performs reasonably when reconstructing quintessence models of dark energy models, can be also applied to models which show a departure from general relativistic behavior at late times. [3] This section illustrates the fact that, in general, reconstructing $H(z)$ and its

[3]Note, however, that most reconstruction methods including the present one may have problems in reproducing the rapidly oscillating equation of state predicted to arise in some models of dark

derivatives such as the deceleration parameter $q(z)$ may be less fraught with difficulty than a reconstruction of $w(z)$, which, being an effective equation of state and not a fundamental physical quantity in some DE models, can often show peculiar properties.

2.1.4 Applying smoothing method on the real data

In the previous subsection we have suggested a non-parametric method based on smoothing the supernova data over redshift in order to reconstruct cosmological quantities, including the expansion rate, $h(z)$, and the equation of state of dark energy, $w(z)$, in a *model-independent* manner. In this approach, the data are dealt with directly, and one does not rely on a parametric functional form for fitting any of the quantities $d_L(z)$, $h(z)$ or $w(z)$. The result obtained by using this approach is, therefore, expected to be model-independent. As we have seen in the previous section, this method was shown to be successful in discriminating between different models of dark energy if the quality of data is commensurate with that expected from the future SuperNova Acceleration Probe (SNAP). In this section we slightly improve the smoothing method and apply it to two recent sets of supernovae data: Gold [46] and SNLS [47]. We then compare the derived expansion history of universe with the results of baryon acoustic peak observations [96]. Specifically, we use the improved smoothing method to reconstruct the Hubble parameter, $h(z)$, and then derive the distance factor, A, up to a redshift of 0.35 independently of the assumption of any cosmological model. This derived value, based on supernovae data, is then compared with the distance factor A (which is also claimed to be relatively independent of dark energy model) being determined by the detection of the baryon acoustic oscillation peak. One of the main results of this section is that there is a good agreement between supernovae data (both Gold and SNLS) and baryon acoustic peak observations for the values $\Omega_{0m} \approx 0.276 \pm 0.023$. The derived value of Ω_{0m} is then used to reconstruct the equation of state of dark energy for both supernovae datasets. We should emphasize here that all the results are only based on observational data and no theoretical model has been assumed. This is an advantage of this method over the functional fitting methods in which the reconstructed results are biased by an assumed functional form or a theoretical model.

energy [95].

Defining the basic parameters in the smoothing method

As we have seen earlier, it is important to choose a value of Δ which gives a small value of the bias and also reasonably small errors on derived cosmological parameters. To estimate the value of Δ in eqn (2.2), we consider the eqn (2.5) relation. We also know that the bias of the method is approximately related to Δ^2 (see appendix A). This implies that by increasing Δ we will also increase the bias of the results. If we attempt to estimate Δ such that $\frac{\delta H}{H} \propto 3\sigma$, then for $N = 182$ data points (which is the number of data points in the Gold sample), we get $\Delta = 0.084$ for a single iteration of our method. However, with each iteration, the errors on the parameters will increase. Therefore, using this value of Δ when we use an iterative process to find the guess model will result in such large errors on the cosmological parameters as to render the reconstruction exercise meaningless. We see in appendix A, that at the M-th iteration, the error on $\ln d_L$ will be approximately $\delta_M(\ln d_L) \simeq \sqrt{M}\delta_0(\ln d_L)$, and the error on $\ln d_L$ scales as $1/\Delta$. We would like the errors after M iterations to be commensurate with the optimum errors obtained for a single iteration, δ_0, so we require $\Delta_{\rm optimal} \simeq \sqrt{M}\Delta_0$. Therefore, if we wish to stop the boot-strapping after 50 iterations, then $\Delta_{\rm optimal} \simeq 0.6$. However, after this rough estimation of the values of Δ and M, we can still play around these values to find the best combination, by minimizing the likelihood of the reconstructed results to the data. In the following, we use $\Delta = 0.6$ and we calculate the χ^2 of the reconstructed distance moduli to the data after each iteration, and we stop the boot-strapping process after reaching the minimum value of χ^2. This effect, that χ^2 of the reconstructed results goes to a minimum value and increases again with iteration is a reflection of the problem of some iterative reconstruction algorithms which are not error-sensitive. In these cases the noise will be added to the reconstructed results after certain number of iterations and the iterative process should be stopped after reaching the minimum value of χ^2 to get the best result. Similar effect has been studied in the next chapter in the Richardson-Lucy deconvolution algorithm to reconstruct the form of primordial power spectrum from CMB data .

In appendix C we show that the results are not sensitive to the chosen value of Δ and also to the assumed initial guess model.

2.1.5 Results from the Gold Dataset

The recently released Gold sample [46], consist of 182 supernovae type Ia which have been gathered from five different subsets of data, observed during the last 16

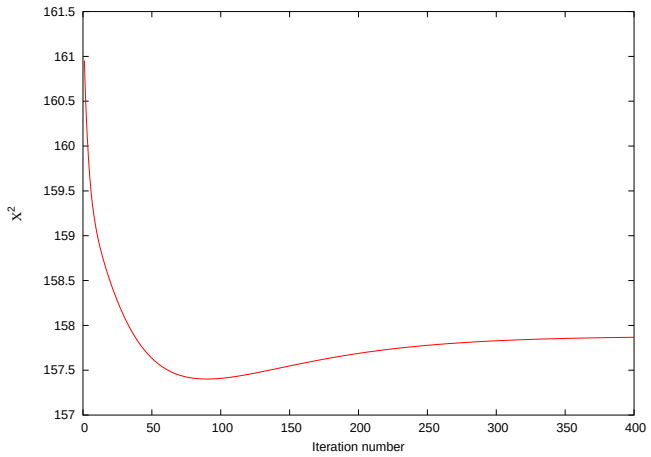

Figure 2.8: Computed χ^2 for the reconstructed results at each iteration, using Gold sample.

years. The range of redshift for these supernovae are between 0.024 and 1.75. In this section we use this dataset to reconstruct $h(z)$, estimate the value of Ω_{0m}, and then reconstruct $w(z)$. We choose a flat ΛCDM model with $\Omega_{0m} = 0.30$ as the initial guess model in our calculation and we fix the value of Δ (width of smoothing) to be 0.6. After each iteration, we compute the χ^2 and we stop the boot-strapping process once χ^2 reaches its minimum value. The χ^2 at any iteration is calculated from the formula(see appendix E),

$$\chi^2_{rec,j}(H_0) = \Sigma_i \frac{(\mu_{rec,j}(H_0, z_i) - \mu_{obs}(z_i))^2}{\sigma_i^2} \tag{2.13}$$

and is followed by marginalizing over H_0. We have marginalized over H_0 by integrating over the probability density $p \propto exp(-\chi^2/2)$ for all values of H_0. In eqn (2.13), $\mu_{rec,j}(H_0, z_i)$ is the reconstructed result at the jth iteration for the distance moduli at redshift z_i, assuming the value of H_0, and $\mu_{obs}(z_i)$ is the Gold sample data given by [46]. In figure 2.8 we show the χ^2 of the reconstructed results at different iterations, after marginalizing over H_0. As we see, the χ^2 has a minimum around $j = 89$ and after this, χ^2 is slowly increasing. So we stop the boot-strapping process at this iteration and determine $h(z)$. We can also see that for the initial guess ΛCDM model, the $\Delta\chi^2$ of the best recovered result is less than 4 which means that the flat ΛCDM model is in agreement with the Gold sample within 2σ.

By marginalizing over the Hubble parameter, we carry out a similar treatment on the data as it has been done by [46] to calculate the χ^2 for different cosmological models. As the Gold data are based on a Hubble parameter of 65 km/sec/Mpc, the

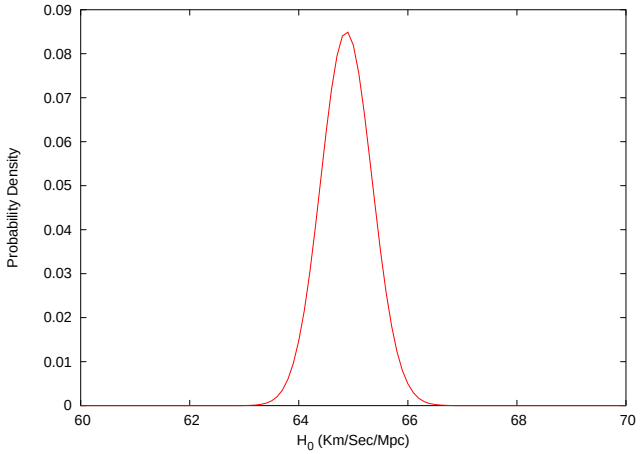

Figure 2.9: Probability density of the best reconstructed result from Gold data for different values of Hubble parameter.

reconstruction method should be able to recover this value for the Hubble constant. In fact the peak of the probability density of the reconstructed result for different values of the Hubble parameter should be close to $H_0 = 65$ km/sec/Mpc. In figure 2.9 we show the probability density of the best reconstructed result from Gold data for different values of the Hubble parameter. We see that the probability density has a sharp peak around H_0 =65 km/sec/Mpc.

We should also note here, that the reduced χ^2 of the reconstructed results seems to be consistently below 1 (however it is not trivial to define the degree of freedom in our smoothing method and hence the reduced χ^2, but we can see that the resultant χ^2 of the reconstructed results is around 25 less than the number of data points). We can also see in figure 2.8 that the reduced χ^2 of the first initial guess model, which is a ΛCDM model, is also below 1. It shows that the error-bars of the supernovae data points are quite large and many different reconstructed results may have a reduced χ^2 of less than 1. In this analysis we only calculate the χ^2 of the reconstructed results and we compare different results by calculating the $\Delta\chi^2$ to the best result with a minimum χ^2.

In figure 2.10, left panel, we show the reconstructed $h(z)$ for the Gold data set. The red solid line has the highest likelihood and is our best reconstruction. All the other lines are within 1σ away from the best recovered result. These lines are recovered results from our smoothing method by using different numbers of iterations in the boot-strapping process. The $\Delta\chi^2$ for all of these lines is less than 1, and so we can consider them to lie within 1σ of the best result. We should note

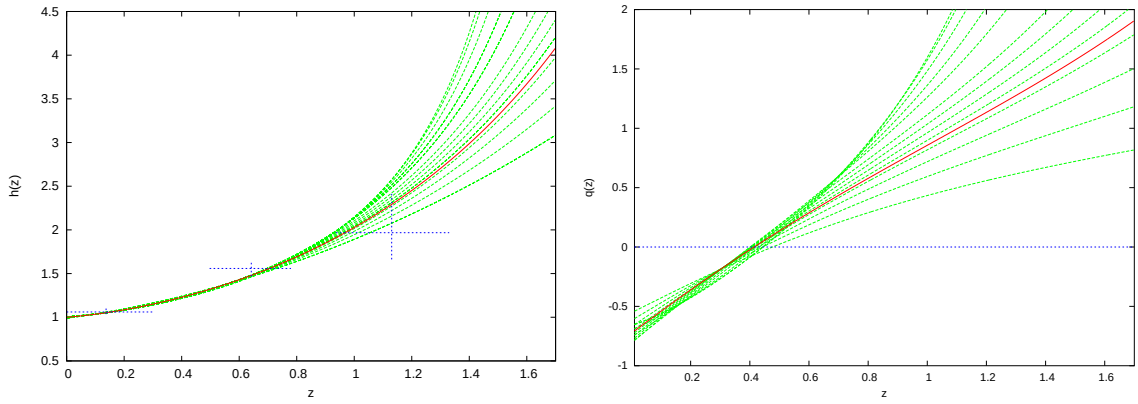

Figure 2.10: Reconstructed $h(z)$ (left) and $q(z)$ (right) by using Gold dataset. Red solid line is the best recovered result and the green dashed lines are within 1σ away from the best result. Based on our results, the transition between deceleration and acceleration phases of the universe occurs at $0.38 < z < 0.48$ within 1σ error-bar from the best recovered result. In the left panel we can also see 3 uncorrelated and independent measurements of $h(z)$ from the Gold sample (blue dotted crosses from [46]) for comparison with our reconstructed results.

that these green dashed lines in figure 2.10 are in fact a non-exhaustive sample of results which are within 1σ away from the best recovered result. As we see in the figure 2.10, the reconstructed $h(z)$ at high redshift has a very big degeneracy. This is expected since there is only a single supernova beyond redshift 1.4!

In this figure we can also see 3 uncorrelated and independent measurements of $h(z)$ from the Gold sample (blue dotted crosses from [46]) for comparison with our results. We can see that these two results are consistent with each other within their 1σ limits. However we should mention here that in the [77] method used by [46] for uncorrelated estimates of the expansion history, there is a slight bias in the reconstruction of $h(z)$ and the higher derivatives of the data. It is mainly because of using the average of the measured quantity $h(z)^{-1}$, which typically is not a straight line. So as it has been mentioned in [77], the measured average of $h(z)^{-1}$ (and hence $h(z)$) over a redshift bin will generally lie either slightly above or below the actual curve at the bin center. This can be the reason that why the centers of the crosses in figure 2.10, left panel, for uncorrelated estimates of the expansion history, are slightly above or below our reconstructed curve for the $h(z)$.

To reconstruct the Hubble parameter, $h(z)$, we do not need to know the value of Ω_{0m}. Another important cosmological quantity which we can derive from the

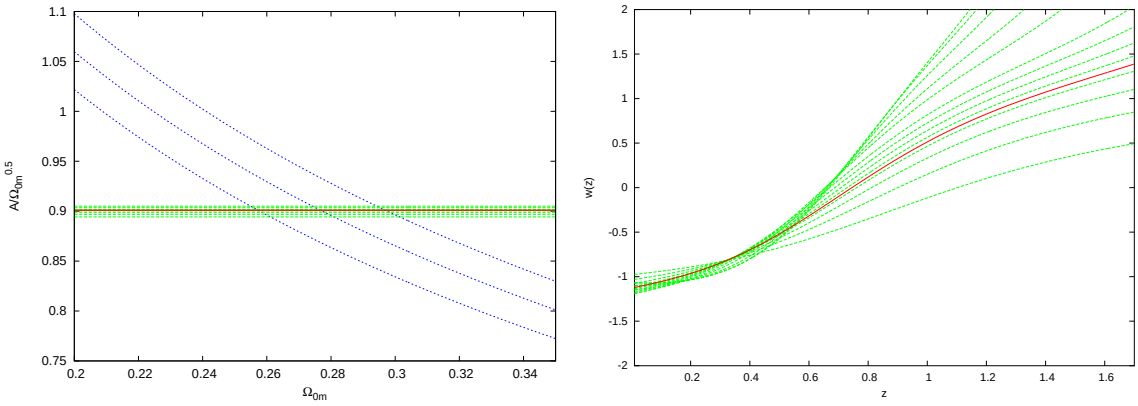

Figure 2.11: Left panel: The derived value of $A/\sqrt{\Omega_{0m}}$ from supernovae Gold data within its 1σ error-bars (red solid line and green dashed lines) in comparison with its measured value from observation of LRGs within its 1σ error-bars (blue dotted lines) for different values of Ω_{0m}. Right panel: Reconstructed $w(z)$ for the Gold dataset. Red solid line is the best recovered result and the green dashed lines are within 1σ away from the best result. To get these results, we have marginalized over $\Omega_{0m} = 0.277 \pm 0.022$.

reconstructed $h(z)$ (independent of the value of Ω_{0m}), is the deceleration parameter, $q(z)$,

$$q(z) = (1+z)\frac{H'(z)}{H(z)} - 1. \tag{2.14}$$

In figure 2.10, right panel, we show reconstructed $q(z)$. For the Gold data our method shows that the transition between deceleration and acceleration occurred at $0.38 < z < 0.48$ (at 1σ). The best reconstruction shows the redshift of transition to be $z_a \simeq 0.42$. This is in agreement with results obtained using parametric methods [97, 98].

To derive the equation of state of dark energy $w(z)$, one needs to know the value of Ω_{0m}, as we see in eqn (2.4). To estimate the value of Ω_{0m}, without using any parameterization and in a model-independent way, we can use the results of the detection of the baryon acoustic oscillation peak [96, 99]. The distance factor A up to redshift 0.35, measured by observation of luminous red galaxies (LRG) in detection of baryon acoustic oscillation peak (which have been claimed to be relatively independent of the model of dark energy), can be derived directly for

different values of Ω_{0m} by using the reconstructed $h(z)$,

$$A = \frac{\sqrt{\Omega_{0m}}}{h(z_1)^{1/3}} \left[\frac{1}{z_1} \int_0^{z_1} \frac{dz}{h(z)} \right]^{2/3}, \tag{2.15}$$

where the measured value of A is $A = 0.469(\frac{n}{0.98})^{-0.35} \pm 0.017$ at $z_1 = 0.35$. The 3-year WMAP results, when combined with the results of baryon acoustic oscillations, yield $n = 0.951$ for the spectral index of the primordial power spectrum [100,101]. By using the best reconstructed results for $h(z)$, we get $A/\sqrt{\Omega_m} = 0.901$. In figure 2.11, left panel, we see the derived value of $A/\sqrt{\Omega_m}$ from supernovae data in comparison with its measured value from observation of LRGs for different values of Ω_{0m}. It is clear that these two independent observations which are completely different by nature, are very much in agreement if $0.255 < \Omega_{0m} < 0.299$. This derived value of Ω_{0m} is completely independent of any dark energy model assumption (within the framework of standard general relativity) and is in very close agreement with the results from large scale structure measurements from 2dF [102] and SDSS [103]. This derived value of Ω_{0m} is also in good agreement with the results from [104], where a different model-independent method of reconstruction has been used.

Now by marginalizing over $\Omega_{0m} = 0.277 \pm 0.022$, which is the range of agreement between the two observations, we can reconstruct $w(z)$ from our previously reconstructed $h(z)$. In figure 2.11, right panel, we show the reconstructed $w(z)$, marginalized over Ω_{0m} for the Gold dataset. We see that the data prefer evolving dark energy to the cosmological constant. The degeneracy for the equation of state of dark energy at high redshifts is very large and it is almost impossible to say much about $w(z)$ at high redshifts.

2.1.6 Results from the SNLS dataset

In this section we use the same procedure as we used in the previous section to deal with SNLS supernovae data [47]. The SNLS dataset contains 115 data points in the range of $0.1 < z < 1.0$. We use this dataset, first to reconstruct the Hubble parameter, $h(z)$, and the deceleration factor, $q(z)$, up to redshift 1. Then by using the results of detection of baryon acoustic oscillation peak we derive the value of Ω_{0m}, following which we recover the form of $w(z)$. We use the distance modules of the supernovae available in Tables 8 and 9 in [47] as our dataset in this section.

In figure 2.12 we see the computed χ^2 for the reconstructed results using smoothing method at each iteration. As we see, the χ^2 diverges to its minimum

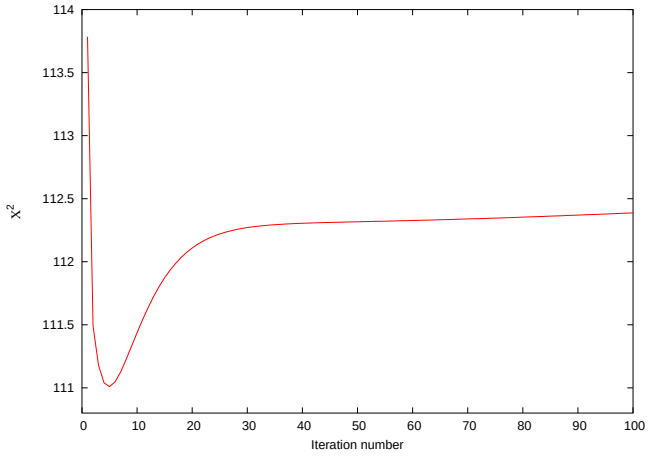

Figure 2.12: Computed χ^2 for the reconstructed results at each iteration for the SNLS dataset.

value very fast at just the 5th iteration. In figure 2.13 we show the reconstructed $h(z)$ (left panel) and $q(z)$ (right panel) for the SNLS dataset. The red solid line has the best likelihood, which is our best reconstructed result. All the other lines are within 1σ away from the best recovered result. We should like to emphasize here that these results (green dashed lines) are not representative of all the possibilities which give the likelihood within 1σ of the best recovered result. However they can show the overall behavior of the quantities which we have studied. Our results for SNLS data show that the transition from deceleration to acceleration phase of the universe occurs at redshifts higher than 0.7. The fact that we cannot put an upper limit to the redshift of the commence of acceleration is due to the absence of supernovae data at $z > 1$ in SNLS dataset.

As we have discussed earlier in the previous section, we use the results of detection of baryon acoustic oscillation peak to determine the value of Ω_{0m}. Then by marginalizing over the recovered value of Ω_{0m}, we derive the dynamics of $w(z)$. In figure 2.14 we see the derived value of Ω_{0m} and the reconstructed form of $w(z)$. We see that the ΛCDM model is in much better agreement with SNLS data than with Gold data.

By comparing the recovered results from the SNLS and Gold datasets, we can clearly see an inconsistency between these two supernovae datasets. This inconsistency is obvious by looking at the reconstructed $q(z)$ and $w(z)$ in the middle and high redshift ranges. Gold data suggest the redshift of the commencement of acceleration at $z_a \simeq 0.42$ while SNLS data suggest $z_a \simeq 0.80$. The reconstructed $w(z)$

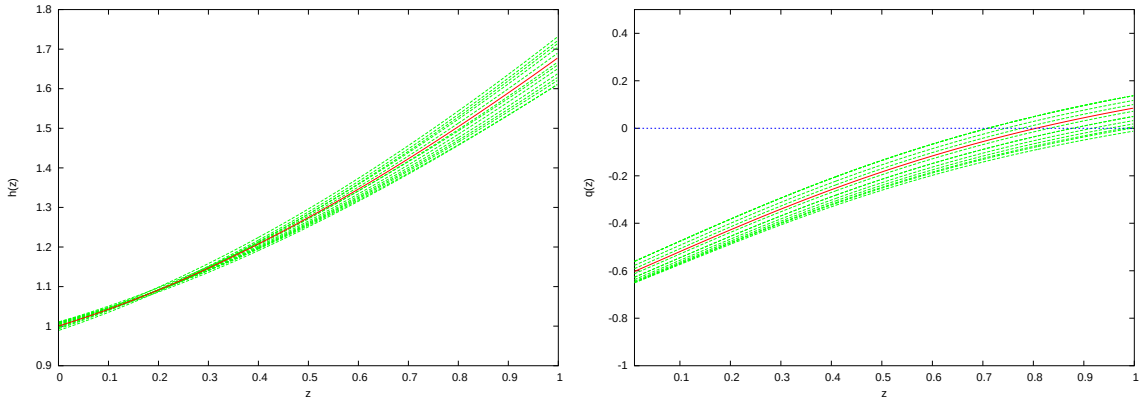

Figure 2.13: Reconstructed $h(z)$ (left) and $q(z)$ (right) by using SNLS dataset. Red solid line is the best recovered result and the green dashed lines are within 1σ away from the best result. Based on our results, the transition between deceleration and acceleration phases of the universe occurs at $z > 0.70$ within 1σ error-bar from the best recovered result.

from these two datasets also shows a very different behavior in the middle and high redshift ranges. The discord between Gold and SNLS supernovae datasets has been reported and studied earlier by [105], and a similar discord between Gold supernovae data and other cosmological observations like CMB observations from WMAP and observations of cluster abundance, has also been reported earlier by [106]. However SNLS supernovae data seem to be in good agreement with the other cosmological observations. Based on all these results and analysis, we may conclude that some significant systematics in the Gold data (or in a part of the data) might be the reason for these inconsistencies.

Interestingly, the recovered values of Ω_{0m} from Gold and SNLS data (by using the results of detection of baryon acoustic oscillation peak), are in very close agreement. In both cases the derived value of Ω_{0m} is around 0.276 ± 0.022. We should note here that the two data sets rely on pretty much the same nearby supernovae samples and that is why the results are similar in this range. It is something which we logically expect to get. But in fact it shows one of the advantages of this method over the functional fitting methods. By using a functional fitting method, the recovered results at any redshift would be equally dependent on the data set in the whole redshift range. But here, by using our smoothing method, we can clearly see that despite the significant differences between the reconstructed results from Gold and SNLS datasets in the middle and high redshift regions, the reconstructed results

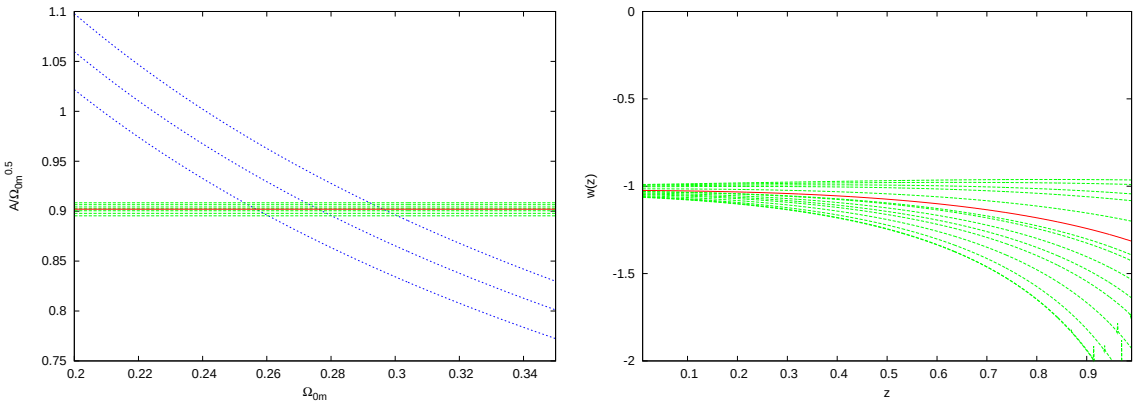

Figure 2.14: Left panel: The derived value of $A/\sqrt{\Omega_{0m}}$ from supernovae SNLS data within its 1σ error-bars (red solid line and green dashed lines) in comparison with its measured value from observation of LRGs within its 1σ error-bars (blue dotted lines) for different values of Ω_{0m}. The consistency of this result with the result from the Gold sample is obvious. Right panel: Reconstructed $w(z)$ for the SNLS dataset. Red solid line is the best recovered result and the green dashed lines are within 1σ away from the best result. To get these results, we have marginalized over $\Omega_{0m} = 0.276 \pm 0.023$.

for the expansion history at low redshifts (which we use to estimate the value of matter density), are not affected by the big differences between the two datasets at the higher redshifts.

2.2 Diagnostics of dark energy

Theoretical models for DE include the famous cosmological constant, Λ, suggested by Einstein in 1917 [1] and shown to be associated with the vacuum energy $\langle T_{ik}\rangle_{\rm vac} \propto \Lambda g_{ik}$ several decades later [107, 108]. Indeed, the cosmological constant appears to occupy a privileged position amongst DE models by virtue of the fact that its equation of state $w = -1$ is Lorentz invariant and so appears the same to any inertial observer. However, within the context of cosmology, an explanation of DE in terms of Λ faces one drawback, namely, in order for the universe to accelerate today the ratio of the energy density in the cosmological constant to that in radiation must have been minuscule at early times, for instance $\rho_\Lambda \simeq 3 \times 10^{-58}\rho_{\rm EW}$ at the time of the electroweak phase transition. Although vacuum energy may conceivably be associated with small numbers such as the neutrino mass ($\rho_\Lambda \sim m_\nu^4$) or even the fine structure constant ($\rho_\Lambda \propto m_P^4 \times \exp(-2/\alpha)$), a firm theoretical prediction for the value

of Λ is currently lacking, allowing room for alternatives including models in which both the DE density and its equation of state (EOS) evolve with time. Alternatives to the cosmological constant include scalar field models called quintessence which satisfy $w > -1$, as well as more exotic 'phantom' models with $w < -1$.

Although most recent studies show that a cosmological constant + cold dark matter (LCDM) is in excellent agreement with observational data, as we have seen in the previous section, dynamical dark energy can explain the data too [12,19,20,27,46,47,54,61,64–68,76,97,100,104,105,109–115]. Indeed, the enormous variety of DE models suggested in the literature has been partially responsible for the burgeoning industry of model independent techniques aimed at reconstructing the properties of dark energy directly from observations [20]. It is well known that model independent methods must be wary of several pitfalls which can subvert their efficacy. These relate to priors which are sometimes assumed about fundamental cosmological quantities such as the EOS and the matter density. As first pointed out in [58], an incorrect prior for the EOS can lead to gross misrepresentations of reality. The same applies to the value of the matter density. Indeed, as we shall demonstrate later in this section, an incorrect assumption about the value of Ω_m can lead to dramatically incorrect conclusions being drawn about the nature of dark energy. Clearly the need of the hour, then, is a diagnostic which is able to differentiate LCDM from 'something else' with as few priors as possible being set on other cosmological parameters.

In this section we introduce three new diagnostics. The first diagnostic, – *Om*, is constructed from observations of the Hubble parameter and provides a *null test* of the LCDM hypothesis. We show that *Om* is able to distinguish dynamical DE from the cosmological constant in a robust manner without reference to the value of the matter density, which can be a significant source of uncertainty for cosmological reconstruction. The *Om* diagnostic is in many respects the logical companion to the statefinder $r = \dddot{a}/aH^3$ [53,69]. We remind the reader that $r = 1$ for LCDM while $r \neq 1$ for evolving DE models. Hence $r(z_1) - r(z_2)$ provides a *null test* for the cosmological constant. Similarly, the unevolving nature of $Om(z)$ in LCDM furnishes $Om(z_1) - Om(z_2)$ as a *null test* for the cosmological constant. Like the statefinder, *Om* depends only upon the expansion history of our universe. However, while the statefinder r involves the third derivative of the expansion factor, *Om* depends only upon $\dot{a}$ and is therefore much easier to reconstruct from observations, as we demonstrate in this section.

The second diagnostic – *Acceleration probe*, is constructed out of the Hubble

parameter and the lookback time. (Like *Om* it does not depend upon the current value of the matter density.) We apply *Acceleration probe* to current data and show that it provides an independent test of an accelerating universe.

The third diagnostic – *w-probe*, is calculated from the first derivative of the data, Hubble parameter, and is a weighted average of the equation of state of dark energy which can provide us some direct information about the equation of state of dark energy without calculating the second derivative of the data. We find that this diagnostic is reconstructed accurately for different reconstruction methods even if Ω_m is marginalized over. *Om* and *w-probe* can be used to successfully distinguish between ΛCDM and other models of dark energy to a high degree of accuracy.

2.2.1 Influence of Ω_m on properties of dark energy

Given the many alternative models of dark energy it is useful to try and understand the properties of DE in a model independent manner. An important model independent quantity is the expansion history, $H(z)$, whose value can be reconstructed from observations of the luminosity distance, D_L, via a single differentiation [48–52] eqn (2.3). The equation of state, $w(z)$, of DE is more cumbersome to reconstruct since it involves two derivatives of $D_L(z)$ and is therefore a noisier quantity than $H(z)$. An additionally source of uncertainty relating to $w(z)$ is caused by the fact that the value of the matter density, Ω_{0m} enters into the determination of $w(z)$ explicitly, through the expression in eqn (2.4). Clearly an uncertainty in Ω_m propagates into the EOS of dark energy even if $H(z)$ has been reconstructed quite accurately. This fact has been emphasized in several papers [20, 58, 97, 116, 117] and is illustrated in figure 2.15, which shows how an erroneous estimate of Ω_m adversely affects the reconstructed EOS by making a LCDM model appear as if it were quintessence (if $\Omega_m^{erroneous} < \Omega_m^{true}$) or phantom (if $\Omega_m^{erroneous} > \Omega_m^{true}$).

The influence of dark matter on dark energy persists if a parametric ansatz such as CPL [55, 60], eqn (2.12),

$$w(z) = w_0 + w_1 \frac{z}{1+z}$$

is employed in the determination of

$$H^2(z) = H_0^2[\Omega_m(1+z)^3 + \Omega_{\rm DE}]$$
$$\Omega_{\rm DE} = (1-\Omega_m)\exp\left\{3\int_0^z \frac{1+w(z')}{1+z'}dz'\right\}. \qquad (2.16)$$

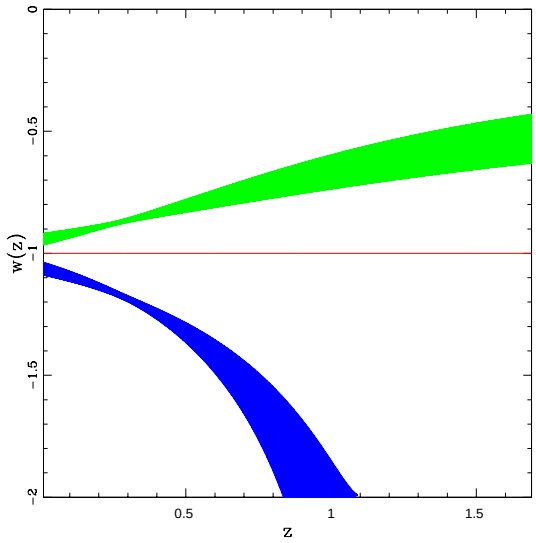

Figure 2.15: The equation of state of a fiducial LCDM model ($w = -1, \Omega_m^{true} = 0.27$) is reconstructed using an incorrect value of the matter density. For $\Omega_m^{erroneous} = 0.22$ the resulting EOS shows quintessence-like behavior and its $1-\sigma$ contour is shown in green. In the opposite case, when $\Omega_m^{erroneous} = 0.32$, the EOS is phantom-like and its $1-\sigma$ contour is shown in blue. Note that in both cases the true fiducial model (red) is excluded in the reconstruction. (The parametric reconstruction scheme, eqn (2.12), suggested in [53,69] was applied to SNAP-quality data to construct this figure.)

In this case, if Ω_m is wrongly specified then, in a maximum likelihood approach, the DE parameters w_0, w_1 will adjust to make $H(z)$ as close to its real value as possible, leading once more to an erroneous reconstruction of the cosmic equation of state.

These two factors: the larger errors caused by the double differentiation of a noisy quantity (D_L) and the strong dependence of $w(z)$ on an uncertain quantity (Ω_m) adversely impact the cosmological reconstruction of the EOS making it difficult to differentiate a cosmological constant from evolving DE from an analysis of $w(z)$ alone.

2.2.2 The Om diagnostic

In this section we suggest an alternative route which enables us to distinguish LCDM from other DE models without directly involving the cosmic EOS. Our starting point is the Hubble parameter which is used to determine the *Om* diagnostic

$$Om(x) \equiv \frac{h^2(x) - 1}{x^3 - 1}, \quad x = 1 + z\,, \tag{2.17}$$

where $h(x) = H(x)/H_0$.

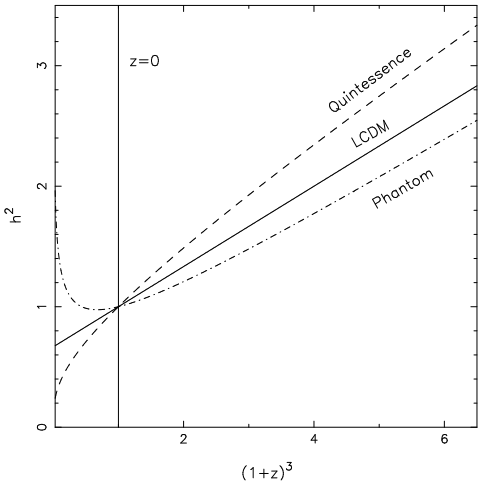

Figure 2.16: The Hubble parameter squared is plotted against the cube of $1 + z$ for Quintessence ($w = -0.7$, dashed), LCDM ($w = -1$, solid) and Phantom ($w = -1.3$, dot-dash). The universe is assumed to be spatially flat and $\Omega_{\rm DE} = 2/3$ in all models. For LCDM the plot h^2 vs $(1 + z)^3$ is a straight line whereas for P and Q this line is curved in the interval $-1 < z \leq 1$. This forms the basis for the observation that $Om(x_1, x_2) = 0$ in LCDM, while $Om(x_1, x_2) > 0$ in quintessence and $Om(x_1, x_2) < 0$ in Phantom. (At $z < 0$ the Hubble parameter for Phantom diverges at a 'big crunch' future singularity, while for Quintessence $h(z) \to 0$ as $z \to -1$. LCDM approaches de Sitter space at late times.)

For dark energy with a constant equation of state

$$h^2(x) = \Omega_{0m} x^3 + (1 - \Omega_{0m}) x^\alpha, \quad \alpha = 3(1 + w)\,, \tag{2.18}$$

(we assume that the universe is spatially flat for simplicity). Consequently,

$$Om(x) = \Omega_{0m} + (1 - \Omega_{0m}) \frac{x^\alpha - 1}{x^3 - 1}\,, \tag{2.19}$$

from where we find

$$Om(x) = \Omega_{0m}\,, \tag{2.20}$$

in LCDM, whereas $Om(x) > \Omega_{0m}$ in quintessence ($\alpha > 0$) while $Om(x) < \Omega_{0m}$ in phantom ($\alpha < 0$). This is a simple consequence of the fact that $h^2(x)$ plotted against x^3 results in a straight line for LCDM, whose slope is given by Ω_{0m}, as shown in figure 2.16. For other DE models the line describing $Om(x)$ is curved, since the equality

$$\frac{dh^2}{dx^3} = constant\,, \tag{2.21}$$

(which always holds for LCDM) is satisfied in quintessence/phantom type models only at redshifts significantly greater than unity, when the effects of DE on the expansion rate can safely be ignored. As a result the efficiency of the Om diagnostic improves at low $z \leq 2$ precisely where there is likely to be an abundance of cosmological data in the coming years !

In practice, the construction of Om requires a knowledge of the Hubble parameter, $h(z)$, which can be determined using a number of model independent approaches [53,69,77,116]. In figure 2.17 we show the Om diagnostic reconstructed from SNAP-quality data using the non-parametric prescription of [115,116]. One clearly sees that for quintessence as well as phantom the line describing $Om(x)$ is curved, which helps distinguish these models from LCDM even if the value of the matter density is not accurately known.

We have reconstructed the Om diagnostic and the cosmic EOS for two Sne data sets: SNLS [47] and Union [27].

The Union dataset [27] is a new compilation of SNe Ia and consists of 307 SNe after selection cuts, includes the recent samples from the SNLS [47] and ESSENCE Surveys [12], older datasets, as well as the recently extended dataset of distant supernovae observed with HST [46].

Results for the SNLS dataset, shown in figure 2.18, indicate that while the EOS is quite sensitive to the value of the matter density, the Om diagnostic is not. Note that the three distinct models of dark energy in figure 2.18 result in virtually the same luminosity distance since: (i) $\chi^2 = 110.93$ for $\Omega_m = 0.32$ (Phantom), (ii) $\chi^2 = 110.99$ for $\Omega_m = 0.28$ (LCDM), (iii) $\chi^2 = 111.02$ for $\Omega_m = 0.22$ (Quintessence). This shows that different values of Ω_m and $w(z)$ can provide an excellent fit to the same set of data, as originally pointed out by [58]. The Om diagnostic is unaffected by this degeneracy (between Ω_m and w) since its form appears to be virtually independent of the input value of Ω_m (and is suggestive of LCDM) as shown in the upper panel of figure 2.18. This leads us to conclude that Om is a robust indicator of DE.

Figure 2.19 shows results for the more recent Union dataset. Again we see that the behavior of the EOS can range from being quintessence-like (for $\Omega_m = 0.22$) to being phantom-like (for $\Omega_m = 0.32$). The behavior of Om is less sensitive to the value of the matter density and leads us to conclude that while a cosmological constant appears to be strongly preferred by SNLS, constraints from the Union dataset allow evolving DE as well as Λ.

Clearly, differencing the value of Om at two independent redshifts can lead to insights about the nature of DE even if the value of Ω_{0m} is not accurately known.

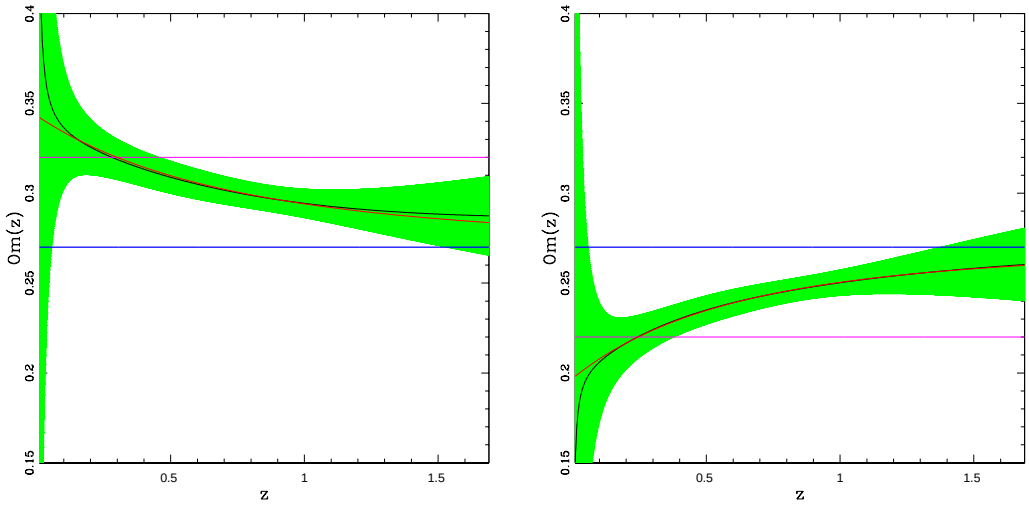

Figure 2.17: The *left panel* shows the $Om(z)$ diagnostic reconstructed for a fiducial **quintessence** model with $w = -0.9$ and $\Omega_m = 0.27$ (black line, green shaded region shows 1σ CL, the red line is the exact analytical result for Om). The horizontal blue line shows the value of Om for a ΛCDM model with the same value of Ω_m as quintessence. Note that any horizontal line in this figure represents ΛCDM with a *different value of* Ω_m. For instance ΛCDM with $\Omega_m = 0.32$ is shown by the horizontal magenta line. As this figure shows, the negative curvature of quintessence allows us to distinguish this model from (zero-curvature) ΛCDM independently of the current value of the matter density. The *right panel* shows the $Om(z)$ diagnostic reconstructed for a fiducial **phantom** model with $w = -1.1$ and $\Omega_m = 0.27$ (black line, green shaded region shows 1σ CL). The positive curvature of phantom allows us to distinguish this model from (zero-curvature) ΛCDM independently of the current value of the matter density. For instance, phantom can easily be distinguished from ΛCDM both with the correct $\Omega_m m = 0.27$ (horizontal blue) as well as incorrect $\Omega_m = 0.22$ (horizontal magenta) ! (The non-parametric smoothing reconstruction scheme suggested in the previous section has been employed on SNAP quality data for this reconstruction.)

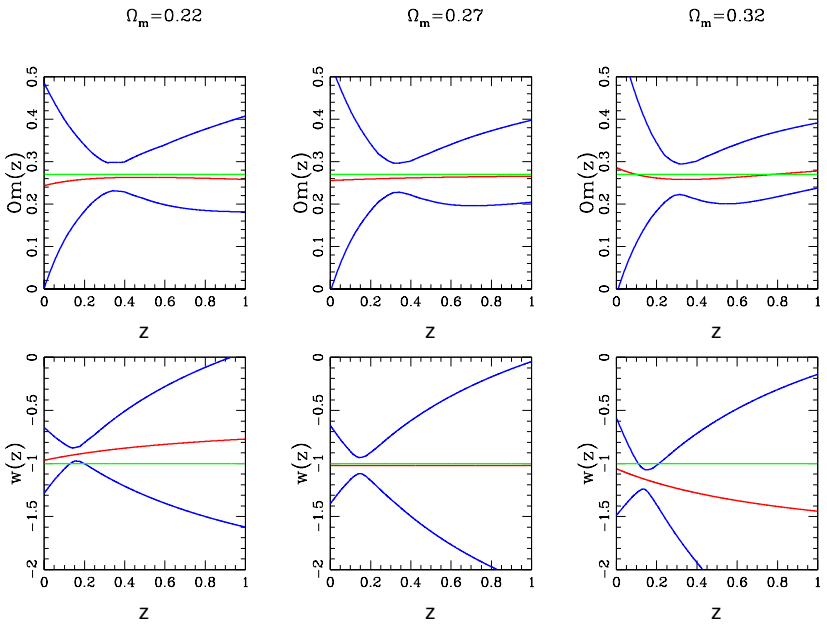

Figure 2.18: Reconstructed $Om(z)$ and $w(z)$ from SNLS supernovae data using the CPL ansatz eqn (2.12) and assuming three different values $\Omega_m = 0.22, 0.27, 0.32$ for the matter density. Notice that while the best fit value of $Om(z)$ is virtually independent of the redshift (top panel, red curve) and is therefore consistent with LCDM (green line), the reconstructed EOS strongly depends upon the value of the matter density. Thus, for the same data set, the best fit value of $w(z)$ is suggestive of quintessence for $\Omega_m = 0.22$, LCDM for $\Omega_m = 0.27$ and phantom for $\Omega_m = 0.32$, while $Om(z)$ favors LCDM throughout. Note that the small variations in $Om(z)$ in the three upper panels are a consequence of the CPL ansatz which requires, as input, the value of the matter density Ω_m. A non-parametric ansatz such as [116] would have led to a uniquely reconstructed $Om(z)$ with no dependence on Ω_m. Blue lines show 1σ error bars.

Thus

$$Om(x_1, x_2) \equiv Om(x_1) - Om(x_2) = (1 - \Omega_{0m}) \left[\frac{x_1^\alpha - 1}{x_1^3 - 1} - \frac{x_2^\alpha - 1}{x_2^3 - 1} \right] , \qquad (2.22)$$

can serve as a *null* test of the cosmological constant hypothesis, since

$$Om(x_1) = Om(x_2) \quad (\Lambda - term) . \qquad (2.23)$$

In contrast, for DE with a constant EOS, $Om(x_1) > Om(x_2)$ for quintessence while $Om(x_1) < Om(x_2)$ for phantom ($x_1 < x_2$). Thus the value of Om determined at two redshifts can help distinguish between DE models *without reference either to the value of the matter density or* H_0 !

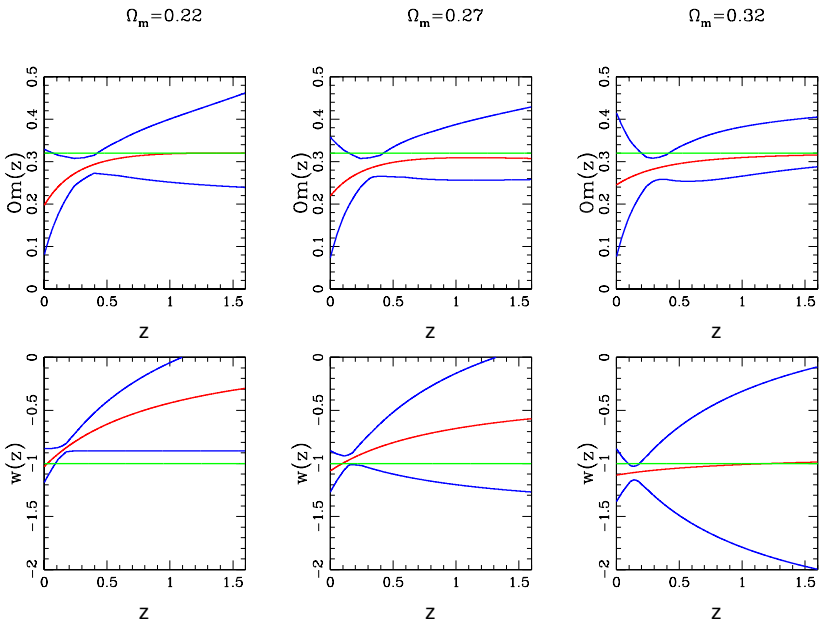

Figure 2.19: Reconstructed $Om(z)$ and $w(z)$ from recent Union supernovae data using the CPL ansatz eqn (2.12) and assuming three different values $\Omega_m = 0.22, 0.27, 0.32$ for the matter density. $Om(z)$ appears to be much more robust against variation in Ω_m in comparison with $w(z)$. The horizontal green line in the top panel indicates value of $Om(\equiv \Omega_m) = 0.32$ for LCDM model. The blue lines show 1σ error bars. Though LCDM is still consistent with the Union data, this consistency is not quite as strong as it was for the SNLS data shown in the previous figure. The top panel clearly indicates that evolving DE is also perfectly consistent with Union data.

One can also hone the efficiency of the Om diagnostic eqn (2.22) by determining it selectively in regions where there is better quality data. The error in the reconstructed value of the Hubble parameter is [82]

$$\frac{\delta H}{H}(z) \propto \frac{\sigma}{N(z)^{1/2}}\,, \tag{2.24}$$

where $N(z)$ is the number of supernovae in a given redshift interval and σ is the noise of the data. Since $N(z)$ is never likely to be a perfectly uniform distribution, there will always be regions where $N(z)$ is larger and $H(z)$ better reconstructed. Consequently, by determining $Om(z_1, z_2)$ selectively in such regions, one can improve the efficiency of this diagnostic by 'tuning it' to the data.

Dark Energy Metamorphosis

An important example of quintessence is provided by tracker models, which give rise to cosmic acceleration at late times while earlier, during the radiative and matter dominated epochs, the density in the tracker remains proportional to the background matter density [95,118]. This last property leads to $\rho_{\rm track}/\rho_{\rm B} \simeq constant \ll 1$ at $z > z_t$, where $\rho_{\rm B}$ is the background density of matter or radiation and z_t is the redshift when tracking ends. As an example consider the double exponential model [118] $V(\phi) = M^4[\exp(-\alpha\phi) + \exp(-\beta\phi)]$ with $\alpha \gg \beta$, $\beta \ll 1$, which has the attractor solution $\Omega_\phi = 3(1+w_B)/\alpha^2$, $w_\phi = w_B$, at high redshift $z > z_t$, while $w_\phi \simeq -1 + \alpha^2/3$ at the present time. Since these models behave like quintessence at late times, their behavior is similar to that shown in figure 2.17 for a typical quintessence model. Consequently these models may be distinguished from LCDM by applying the Om diagnostic shown in figure 2.17. An interesting limiting case corresponds to *metamorphosis* models which have $w_0 \simeq -1$ today and $w \to 0$ at earlier times [68,119].

For such models $Om(x) = \Omega_{0m}$ for $x < x_t$ and $Om(x) = \tilde{\Omega}_{0m}$, for $x \gg x_t$ where

$$\tilde{\Omega}_{0m} \simeq \Omega_{0m} + \frac{1-\Omega_{0m}}{(1+z_t)^3}\,. \tag{2.25}$$

Consequently, the Om diagnostic applied to data at low and high redshift, may help distinguish between tracker DE and LCDM as shown in figure 2.20. Tracker behavior can also arise in modified gravity theories such as Braneworld models [85,120] and scalar-tensor cosmology [121]. The growth of density perturbations provides a complementary means of distinguishing these models from LCDM.

An important property of the Om diagnostic is that the value of the cosmological density parameter Ω_m does not enter into its definition eqn (2.17) explicitly. As a result the diagnostic relation $Om(x_1, x_2) = 0$ (LCDM) does not require an a-priori knowledge of the matter density and therefore provide a means of differentiating the cosmological constant from evolving DE models even if uncertainties exist in the value of Ω_m. (Current observations suggest an uncertainty of at least 25% in the value of Ω_m [110].) For a constant EOS the dependence of Om on the value of the matter density can be altogether eliminated by constructing the ratio

$$\mathcal{R} = \frac{Om(x_1,x_2)}{Om(x_3,x_4)} \equiv \frac{\left[\frac{x_1^\alpha - 1}{x_1^3-1} - \frac{x_2^\alpha-1}{x_2^3-1}\right]}{\left[\frac{x_3^\alpha-1}{x_3^3-1} - \frac{x_4^\alpha-1}{x_4^3-1}\right]}\,, \tag{2.26}$$

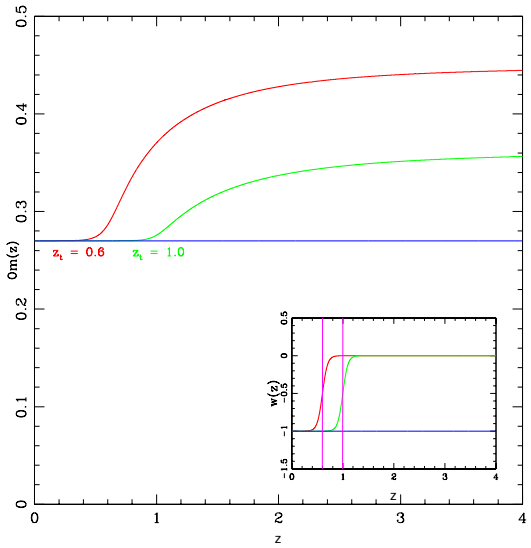

Figure 2.20: The *Om* diagnostic is shown for two tracker models which mimic LCDM at low redshift and dark matter at high $z > z_t$. The horizontal blue line shows LCDM. The inset shows the EOS for the tracker's as a function of redshift.

from where we see that the EOS encoded in the parameter $\alpha = 3(1 + w)$ can be determined from $\mathcal{R}$ without any reference whatsoever to the value of Ω_m !

Influence of spatial curvature on *Om*

The preceding analysis, which showed how the *Om* diagnostic could distinguish between alternative models of DE, was based on the assumption that the universe was spatially flat. While this may well be true, especially within the framework of the inflationary scenario which predicts an exponential decline of the curvature term during inflation leading to a vanishingly small value of Ω_k today, it is also worthwhile to consider the opposite possibility, namely that the curvature is small but finite, such as $\Omega_k \simeq -0.0175$, which is in marginal agreement with WMAP5 results $-0.0175 < \Omega_k < 0.0085$ at the 95% CL [110]. In this case eqn (2.22) is modified to

$$Om(x_1, x_2) = \Omega_{\rm DE}\left[\frac{x_1^\alpha - 1}{x_1^3 - 1} - \frac{x_2^\alpha - 1}{x_2^3 - 1}\right] + \Omega_k\left[\frac{x_1^2 - 1}{x_1^3 - 1} - \frac{x_2^2 - 1}{x_2^3 - 1}\right],$$
$$x = 1 + z, \tag{2.27}$$

and we assume $x_2 > x_1$.

The influence of the curvature term can be estimated by a simple 'back of the envelope' calculation which we carry out for quintessence (Q) and phantom (P). We assume $\Omega_{\rm DE} = 0.7$, $\Omega_k = -0.0175$, $z_1 = 0.1, z_2 = 1$ and $w = -0.9$ for Q while $w = -1.1$ for P. In the case of Quintessence we find $Om(x_1, x_2) = 0.042$ when the curvature term is included in eqn (2.27) and $Om(x_1, x_2) = 0.038$ when it is excluded. Thus the inequality $Om(x_1, x_2) > 0$, which generically holds for quintessence models, appears to be quite robust, since the contribution (read 'contamination') from the curvature term is only a fraction (9%) of the 'signal' from DE. Similar results are obtained for Phantom: $Om(x_1, x_2) = -0.037$ when the curvature term is included and $Om(x_1, x_2) = -0.041$ when it is not. The presence of curvature leads, once more, to a 9% change in our estimation of Om leading us to conclude that the phantom inequality $Om(x_1, x_2) < 0$ is robust. (Of course, as $w_{\rm DE} \to -1$, the relative influence of curvature in eqn (2.27) becomes significant and can dominate the 'signal' from DE models which are very close to LCDM; see also [122].)

2.2.3 The Acceleration probe

In the previous section we saw how the difference between the value of the Hubble parameter at nearby redshifts could be used to construct a null diagnostic for the LCDM model. In this section we construct another dimensionless quantity which could prove useful for determining the onset of cosmic acceleration in DE models which has also been the focus of other studies [123–125].

Our diagnostic, *acceleration probe*, is the mean value of the deceleration parameter

$$\bar{q} = \frac{1}{t_1 - t_2} \int_{t_2}^{t_1} q(t) dt \ . \tag{2.28}$$

Since

$$q(t) = \frac{d}{dt}\left(\frac{1}{H}\right) - 1 \ , \tag{2.29}$$

it follows that *acceleration probe* can be written in the following simple form

$$1 + \bar{q} = \frac{1}{\Delta t}\left(\frac{1}{H_1} - \frac{1}{H_2}\right) \ , \tag{2.30}$$

where $\Delta t = t_1 - t_2 \equiv (t_0 - t_2) - (t_0 - t_1)$, and

$$t_0 - t(z) = \int_0^z \frac{dz}{(1+z)H(z)} \ , \tag{2.31}$$

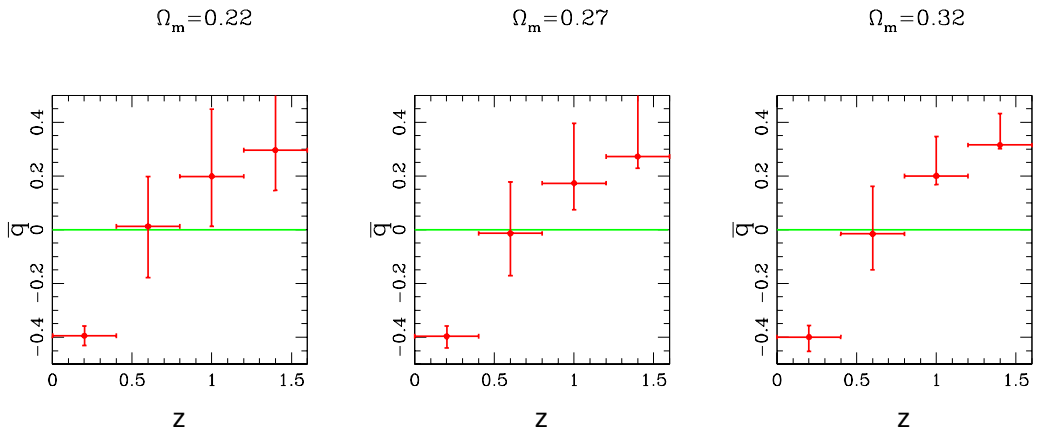

Figure 2.21: The diagnostic $\bar{q}$ is plotted in 4 bins using the recent Union supernovae data. The CPL ansatz has been used for three different values of the matter density. Error-bars in y-axis show $1-\sigma$ CL. Note that the value of the acceleration redshift $0.4 \leq z_a \leq 0.8$ appears to be robust.

is the cosmic look-back time (also see [66, 124–129]).

Equation (2.30) expresses the mean deceleration parameter in terms of the look-back time and the value of the Hubble parameter at two distinct redshifts. From expressions eqn (2.30) and eqn (2.31) we find that, like the *Om* diagnostic, the acceleration probe $\bar{q}$ does not depend upon the value of Ω_m, and is therefore robust to uncertainties in the value of the matter density.

In figure 2.21 we show $\bar{q}$ obtained using Union supernovae and the CPL ansatz. The behavior of $\bar{q}$ suggests $0.4 \leq z_a \leq 0.8$ for the redshift at which the universe began to accelerate. This result is independent of the value of the matter density. Close to the acceleration redshift, $\bar{q} \simeq 0$, and one obtains a very simple relationship linking the look-back time with the Hubble parameter

$$\Delta t = \frac{1}{H_1} - \frac{1}{H_2}\,, \tag{2.32}$$

where H_1 and H_2 lie on 'either side' of the acceleration redshift z_a. Since both the look-back time and the Hubble parameter can be reconstructed quite accurately

(see for instance [20,66,126]), it follows that one might be able to obtain the redshift of the acceleration epoch in a model independent manner using eqn (2.32).

It is worth noting that the value of $\bar{q}$ can also be obtained from an accurate determination of galactic ages. In this case we do not require a continuous form of $H(z)$ to compute the look-back time. We simply subtract the galactic ages at two distinct redshifts bins to determine Δt. The same information can also be used to derive $H(z)$ since

$$H(z) = \frac{-1}{1+z}\frac{dz}{dt}, \tag{2.33}$$

which is then used to determine $\bar{q}$. However at present the errorbars on the observed galactic ages are large and the number of data is small, so it is unlikely that this method will be useful for determining $\bar{q}$ at this stage. In the future, with the better quality and quantity of data, $\bar{q}$ can be used as a model independent probe of the acceleration of the universe using distinct and uncorrelated cosmological data.

Note that the acceleration epoch is quite sensitive to the underlying DE model. For DE with a constant equation of state

$$1 + z_a = \left(\frac{|1+3w|\Omega_{0DE}}{\Omega_m}\right)^{\frac{1}{|3w|}}, \tag{2.34}$$

and so an accurate determination of z_a using eqn (2.32) could provide useful insights into the nature of DE.

2.2.4 w-probe

In this subsection we explore the possibility of extracting information about the equation of state of dark energy from the reconstructed Hubble parameter by considering a weighted average of the equation of state, which we call the *w-probe*. An important advantage of this approach is that there is no need to go to the second derivative of the luminosity distance for information on the equation of state. Instead, we consider the weighted average of the equation of state [68]

$$1 + \bar{w} = \frac{1}{\delta \ln(1+z)} \int (1 + w(z)) \frac{dz}{1+z}, \tag{2.35}$$

Table 2.2: The reconstructed *w-probe* ($\bar{w}$), determined using eqn (2.36) (and its 1σ error) is listed for 1000 realizations of SNAP data. Three fiducial models are used : $w = -1/(1+z)$, $w = -1$ (ΛCDM) and $w = -0.5$. We deploy the method of double smoothing with $\Delta = 0.24$ to determine $\bar{w}$.

	$w = -1/(1+z)$		$w = -1$		$w = -0.5$	
Δz	$\bar{w}$	$\bar{w}_{\rm exact}$	$\bar{w}$	$\bar{w}_{\rm exact}$	$\bar{w}$	$\bar{w}_{\rm exact}$
$0 - 0.414$	-0.839 ± 0.019	-0.845	-1.001 ± 0.017	-1.0	-0.489 ± 0.025	-0.5
$0.414 - 1$	-0.595 ± 0.033	-0.598	-1.009 ± 0.038	-1.0	-0.506 ± 0.039	-0.5
$1 - 1.7$	-0.471 ± 0.069	-0.432	-1.017 ± 0.087	-1.0	-0.493 ± 0.075	-0.5

which can be directly expressed in terms of the difference in dark energy density $\tilde{\rho}_{DE} = \rho_{DE}/\rho_{0c}$ (where $\rho_{0c} = 3H_0^2/8\pi G$) over a range of redshift as

$$1 + \bar{w}(z_1, z_2) = \frac{1}{3}\frac{\delta \ln \tilde{\rho}_{DE}}{\delta \ln(1+z)} = \frac{1}{3}\ln\left[\frac{H^2(z_1) - \Omega_{0\rm m}(1+z_1)^3}{H^2(z_2) - \Omega_{0\rm m}(1+z_2)^3}\right] \Big/ \ln\left(\frac{1+z_1}{1+z_2}\right) \qquad (2.36)$$

where δ denotes the total change of a variable between integration limits. Thus, even if the equation of state is noisy, the $\bar{w}$ parameter may be obtained accurately provided the Hubble parameter is well constructed.

The parameter $\bar{w}$ has the interesting property that for the concordance ΛCDM model, it equals -1 in all redshift ranges while for other models of dark energy it is non-zero. For (non-ΛCDM) models with constant equation of state, this parameter is a constant (but not equal to -1), while for models with variable equation of state, it varies with redshift. The fact that ΛCDM is a fixed point for this quantity may be utilized to differentiate between the concordance ΛCDM model and other models of dark energy. Therefore the parameter $\bar{w}$ may be used as a new diagnostic of dark energy which acts as a discriminator between ΛCDM and other models of dark energy. We call this diagnostic the *w-probe*.

We now calculate the *w-probe* for the three models described in the previous sections using the method of double smoothing. In table 2.2, we show the values of $\bar{w}$ obtained in different redshift ranges after applying double smoothing on SNAP-like data. The ranges of integration are taken to be approximately equally spaced in $\ln(1+z)$. Two points of interest should be noted here: a) $\bar{w}$ is very close to $\bar{w}_{\rm exact}$ at all redshifts for all three models of dark energy; and b) as expected, this parameter is good at distinguishing between ΛCDM and other dark energy models.

In the above analysis, we have assumed that the matter density is known

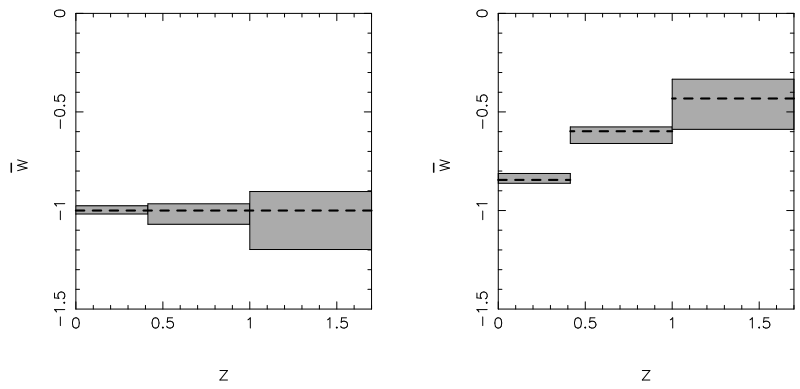

Figure 2.22: The w-probe is reconstructed for the unevolving ΛCDM model with $w = -1$ (left panel) and an evolving DE model with $w = -1/(1+z)$ (right panel). 1000 realizations of SNAP-like data have been used. The thick dashed line in both panels indicates the exact value of $\bar{w}$ for the fiducial model, the dark gray boxes in each panel indicate the 1σ confidence levels on $\bar{w}$ reconstructed for the two models using the double smoothing scheme with $\Delta = 0.24$ and marginalizing over $\Omega_m = 0.3 \pm 0.07$. This figure illustrates that the w-probe works remarkably well for both ΛCDM (left panel) and for evolving DE (right panel). The details for this figure are given in table 2.3.

exactly, $\Omega_m = 0.3$. As noted before a small uncertainty in the value of Ω_m may affect the reconstruction exercise quite dramatically. The Hubble parameter is not affected to a very high degree by the value of matter density, because it can be calculated directly as the first derivative of the luminosity distance, which is the measured quantity. However, when calculating the equation of state of dark energy, the value of Ω_m appears in the denominator of the expression (2.4), hence any uncertainty in Ω_m is bound to affect the reconstructed $w(z)$. We have seen this effect in figure 2.15.

One of the main results of this chapter is that, although the equation of state $w(z)$ may be reconstructed badly if Ω_m is not known accurately, the uncertainty in Ω_m does not have such a strong effect on the reconstruction of the *w-probe*($\bar{w}$). This is because $\bar{w}$ in eqn (2.36) is a difference of two terms, both involving Ω_m. As a result, uncertainty in Ω_m does not affect $\bar{w}$ as much as it affects $w(z)$. Therefore, even when Ω_m is not known to a high degree of accuracy, the *w-probe* may still be reconstructed fairly accurately.

We now demonstrate this by showing the results obtained using our smoothing scheme after marginalizing over the matter density. We simulate SNAP like data for two models: (a) ΛCDM and (b) a $w = -1/(1+z)$ 'metamorphosis' model. When applying the smoothing scheme, we assume that Ω_m follows a Gaussian probability distribution with mean $\overline{\Omega_m} = 0.3$ and variance $\sigma = 0.07$ (the error being commensurate to that expected from the current CMB and Large Scale Structure

Table 2.3: The reconstructed *w-probe* $\bar{w}$ (eqn (2.36)) over specified redshift ranges (and its 1σ error) is shown for 1000 realizations of SNAP data. Two fiducial models are used : the $w = -1/(1+z)$ 'metamorphosis' model and $w = -1$ (ΛCDM). We deploy the method of double smoothing with $\Delta = 0.24$ and marginalize over $\Omega_m = 0.3 \pm 0.07$.

	$w = -1/(1+z)$		$w = -1$	
Δz	$\bar{w}$	$\bar{w}_{\rm exact}$	$\bar{w}$	$\bar{w}_{\rm exact}$
$0 - 0.414$	-0.837 ± 0.025	-0.845	-1.003 ± 0.021	-1.0
$0.414 - 1$	-0.618 ± 0.042	-0.598	-1.018 ± 0.052	-1.0
$1 - 1.7$	-0.461 ± 0.127	-0.432	-1.051 ± 0.147	-1.0

data [103]). In figure 2.22 and table 2.3, we show the results for the *w-probe* calculated for the two models. We find that the *w-probe* ($\bar{w}$) is determined to a high degree of accuracy for both the models even when we marginalize over Ω_m! The value of $\bar{w}$ for the ΛCDM model is approximately equal to -1, while that for the metamorphosis model shows clear signature of evolution. Thus, even if the matter density of the universe is known uncertainly, this uncertainty does not affect the accuracy of the reconstructed *w-probe* significantly. This is a powerful result since it indicates that unlike the equation of state, the *w-probe* is not overtly sensitive to the value of Ω_m for SNAP-quality data.

From the above results, we see that the *w-probe* is very effective as a diagnostic of dark energy, especially in differentiating between ΛCDM and other models of dark energy. We summarize some important properties of the *w-probe* below:

1. $\bar{w}(z_1, z_2)$ is determined from the *first* derivative of the luminosity distance. Its reconstructed value is therefore less noisy than the equation of state $w(z)$ (which is determined after differentiating $d_L(z)$ twice; compare eqn (2.4) and eqn (2.36)).

2. $\bar{w}(z_1, z_2) = -1$ *uniquely* for concordance cosmology (ΛCDM). For all other dark energy models $\bar{w} \neq -1$. This remains true when $\bar{w}$ is marginalized over Ω_m.

3. $\bar{w}$ is robust to small uncertainties in the value of the matter density. As we saw earlier this uncertainty can induce large errors in determinations of the cosmic equation of state $w(z)$. The weak dependence of $\bar{w}$ on the value of Ω_m in the range currently favored by observations $0.2 \leq \Omega_{0m} \leq 0.4$ implies that the *w-probe* can cope very effectively with the existing uncertainty in the

value of the matter density for SNAP-quality data. Furthermore, since $\bar{w}$ is constructed directly from $\rho_{\rm DE}$, any method which determines either the dark energy density or the Hubble parameter from observations can be used to also determine $\bar{w}$. Note that several excellent methods for determining $\rho_{\rm DE}$ and $H(z)$ have been suggested in the literature [54, 61, 68, 75–77], and any of these could be used to great advantage in determining the *w-probe*.

Thus we expect that the *w-probe* may be used as a handy diagnostic for dark energy, especially in discriminating between ΛCDM and other models of dark energy. Its efficacy lies in the fact that it is not very sensitive to both the value of the present matter density and also the reconstruction method used.

2.2.5 Determining *Om* and the *acceleration probe* from SNe, BAO and CMB

In this section we determine two of our new diagnostics, *Om* and $\bar{q}$, from a combination of: (i) the Union supernovae data set [27], (ii) data from baryon acoustic oscillations (BAO) [96], (iii) WMAP5 CMB data [3].

Acoustic oscillations in the photon-baryon plasma prior to recombination give rise to a peak in the correlation function of galaxies. This effect has recently been measured in a sample of luminous red galaxies observed by the Sloan Digital Sky Survey, (see eqn (2.15)), and leads to the value [96] $A = 0.469\left(\frac{n}{0.98}\right)^{-0.35} \pm 0.017$. The 5 year Wilkinson Microwave Anisotropy Probe (WMAP5) results, when combined with the results from BAO yield $n = 0.961$ for the spectral index of the primordial power spectrum [3, 101].

We also use the following value for the CMB 'shift parameter' (the reduced distance to the last scattering surface) deduced from WMAP5

$$R = \sqrt{\Omega_m}\int_0^{z_{\rm ls}} \frac{dz}{h(z)} = 1.715 \pm 0.021\ , \tag{2.37}$$

where $z_{\rm ls} = 1089$. We use the two constraints, A, R together with the Union SNe data set to determine $Om(z)$ and $\bar{q}$. The CPL ansatz eqn (2.12) has been used to parametrize the expansion history, and all three parameters in this ansatz Ω_m, w_0 and w_1 are treated as free in our maximum likelihood routine. Our results are summarized in figure 2.23. We find that LCDM is in excellent agreement with the data but other DE models fit the data too. These include quintessence and phantom models, some of which are shown in figure 2.24.

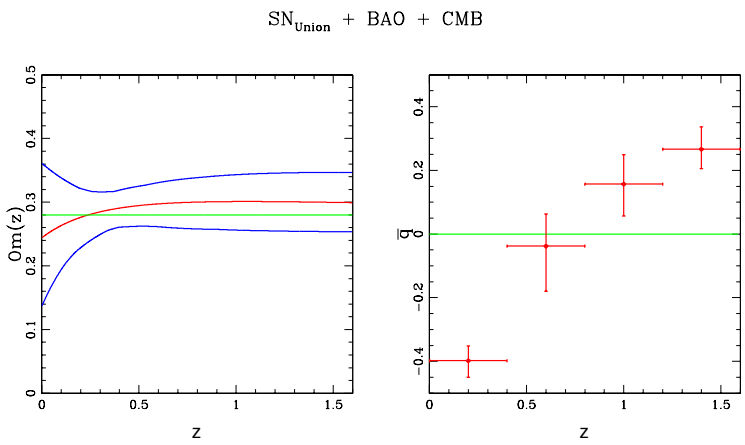

Figure 2.23: Two new diagnostics, $Om(z)$ (left panel) and $\bar{q}$ (right panel) are plotted using combination of supernovae, BAO and CMB data. CPL ansatz have been used here assuming matter density also as a free parameter. Blue lines in left panel and red crosses in right panel show 1σ errorbars.

2.3 Summary and Conclusion

This major chapter of the thesis, presents a new approach to analyzing supernova data and uses it to extract information about cosmological functions, such as the expansion rate of the universe $H(z)$ and the equation of state of dark energy $w(z)$. In this approach, we deal with the data directly and do not rely on a parametric functional form for fitting any of the quantities $d_L(z), H(z)$ or $w(z)$. Therefore, we expect the results obtained using this approach to be model independent. A Gaussian kernel is used to smooth the data and to calculate cosmological functions including $H(z)$ and $w(z)$. The smoothing scale used for the kernel is related to the number of supernovae, errors of observations and derived errors of the parameters by a simple formula, eqn (2.5). For a given supernova distribution, the smoothing scale determines both the errors on the parameters and the bias of the results (see appendix A). Δ cannot be increased arbitrarily as this would diminish the reliability of the results. We use a value of Δ which gives results which have reasonably small bias as well as acceptable errors of $H(z)$ for the SNAP quality data used in our analysis (see section 2.1.2). As can be seen from eqn (2.5), when the data improves (i.e., the number of data points increases and/or measurement errors decrease), we expect that the same value of Δ would result in smaller errors on $H(z)$.

We demonstrate that this method is likely to work very well with future SNAP-like SNe data, especially in reconstructing the Hubble parameter, which encodes the

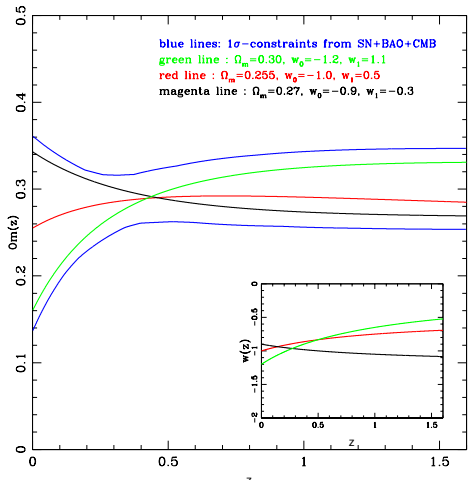

Figure 2.24: The blue lines in the main figure show 1σ constraints on $Om(z)$ from a combination of Sne, BAO and CMB data. Also shown are values for $Om(z)$ from three DE models all of which are consistent with the data at the 1σ level. The green line is DE with $\Omega_m = 0.3, w_0 = -1.2, w_1 = 1.1$, this model crosses the phantom divide at $w = -1$. The red line shows a metamorphosis model with $\Omega_m = 0.255, w_0 = -1.0, w_1 = 0.5$, while magenta shows quintessence with $\Omega_m = 0.27, w_0 = -0.9, w_1 = -0.3$. In all cases the CPL ansatz eqn (2.12) has been used and the bottom-right corner of the figure shows the EOS for these diverse DE models.

expansion history of the universe. Moreover, our successful reconstruction of the Hubble parameter can also be used to distinguish between cosmological models such as ΛCDM and evolving dark energy. The method can be further refined, if one wishes to reconstruct the cosmic equation of state to greater accuracy, by double smoothing the data– smoothing the Hubble parameter, after it has been derived from the smoothed luminosity distance, so as to reduce noise in $w(z)$ (as in section 2.1.2). The results obtained using the smoothing scheme compare favorably to results obtained by other methods of reconstruction. Another quantity which may be reconstructed to great accuracy is the look-back time of the universe.

We therefore conclude that the proposed reconstruction method by smoothing the supernova data appears to be sufficiently accurate and, when applied to SNAP-type observations, should be able to distinguish between evolving dark energy models and a cosmological constant.

The method proposed by us can also be used for other forms of data which deliver the luminosity (or angular size) distance.

In the next step of our studies in this chapter of the thesis, we have shown that by improving the efficacy of the smoothing method, we can reconstruct the expansion

history of the universe in a model-independent way, using current supernovae data. We have used the smoothing method to reconstruct the expansion history of the universe, $h(z)$, the deceleration parameter, $q(z)$, the value of Ω_{0m} and the equation of state of dark energy, $w(z)$, independently of any assumption of the theoretical model of the universe, within the framework of standard general relativity. This is an advantage of this method over the functional fitting methods where the results are usually biased by the form of the functional fitting or the assumed theoretical model. We dealt with two recent datasets, Gold and SNLS in our analysis. In determining the value of Ω_{0m}, we found excellent agreement between Gold and SNLS datasets. This determination is directly related to the supernovae data points at redshifts lower than $z = 0.35$ and also the results from baryon acoustic oscillation. We have got $\Omega_{0m} \approx 0.276 \pm 0.023$ for both Gold and SNLS datasets, which is in good agreement with results of SDSS and 2dF large scale structure observations, and also with results of Chandra X-ray observations of the relaxed galaxy clusters [130]. This derived value of Ω_{0m} also agree with the recent WMAP 5 years CMB data, if we assume the broken scale invariant spectrum for the form of the primordial spectrum [180](as we will see in the next chapter). In the derivation of $q(z)$ and the stage of transition from deceleration to acceleration in the dynamics of the universe, we found disagreement between Gold and SNLS datasets. Gold data suggest the redshift of the commence of acceleration at $z_a \simeq 0.42$ while SNLS data suggest $z_a \simeq 0.80$.

After marginalizing over the derived value of Ω_{0m}, we have reconstructed $w(z)$. The inconsistency between Gold and SNLS supernovae datasets is also obvious by looking at the reconstructed $w(z)$ from these two datasets. The derived form of $w(z)$ from SNLS dataset, is in good concordance with ΛCDM model, while Gold dataset prefers an evolving form of dark energy (however ΛCDM is still in agreement with the Gold dataset to within 2σ). This discrepancy between Gold and SNLS datasets has been reported earlier by other groups ([97, 105]). As the Gold sample is also relatively in disagreement with the other cosmological observations like CMB and observations of cluster abundance ([106]), we may conclude that the effect of systematics in the Gold dataset (or at least in a part of the data) is significant.

The large error-bars at the high redshifts for the reconstructed results, reflect the significant lack of data points. This effect may not be seen if we use some of the parametric methods of analysis, but as we deal with the data directly here, we notice that the lack of data points at high redshifts limits our ability to say much about the behavior of the Universe at the early stages at high redshifts. This is another

important feature of our smoothing method in which the reconstructed results at any redshift rely mostly on the supernovae data points at the same redshift range.

In the second major section of this chapter of the thesis, we proposed three new diagnostics for determining the properties of dark energy. The first of these, $Om(z)$, is constructed from the Hubble parameter and results in the identity $Om(z) = \Omega_m$ for LCDM. For other DE models $Om(z)$ is a function of the redshift. This allows one to construct a simple null test to distinguish the cosmological constant from evolving DE. The second diagnostic, *acceleration probe* ($\bar{q}$), is the mean value of the deceleration parameter over a small redshift interval. The *acceleration probe* depends upon the value of the Hubble parameter and the look-back time. We use the current SNe data in conjunction with BAO and CMB results to estimate the values of $Om(z)$ and $\bar{q}$. We find our results to be consistent with LCDM as well as evolving DE models including phantom and quintessence.

Another important result of this chapter of the thesis is the discovery that the *w-probe* provides us with an excellent diagnostic of dark energy. We summarize some of the attractive features of this diagnostic below.

(a) The *w-probe* defined in eqns (2.35) and (2.36) is obtained from the luminosity distance by means of a *single* differentiation. Therefore, it avoids the pitfalls of $w(z)$ which is obtained from the luminosity distance through a double differentiation – see eqn (2.4), and hence is usually accompanied by large errors (see also [132]).

(b) The *w-probe* is robust to small uncertainties in the value of Ω_{0m}. This attractive property allows us to get around observational uncertainties in the value of Ω_{0m} currently known to an accuracy of about 30%. Indeed, when marginalized over Ω_{0m}, the *w-probe* can be used to great advantage to distinguish between ΛCDM and other dark energy models.

We therefore conclude that the proposed reconstruction method by smoothing the supernova data appears to be sufficiently accurate and should be able to distinguish between evolving dark energy models and a cosmological constant. The three new proposed diagnostics of dark energy, Om, $\bar{q}$ and *w-probe* also seem to be very versatile and could help distinguish between ΛCDM and other models of dark energy with least dependency on the value of dark matter density. These diagnostics can be used by any reconstruction method (parametric or non-parametric) with a very good accuracy.

Chapter 3

Primordial power spectrum from cosmic microwave background data

3.1 Introduction

Increasingly accurate measurements of the anisotropy in the temperature of the cosmic microwave background (CMB) have ushered in an era of precision cosmology. A golden decade of CMB anisotropy measurements by numerous experiments was topped by the results from the data obtained by the Wilkinson Microwave Anisotropy Probe (WMAP) [3, 109, 110, 133–138]. Under simple hypotheses for the spectrum of primordial perturbations, exquisite estimates of the cosmological parameters have been obtained from the angular power spectrum measurement by WMAP combined with other cosmological observations [3, 109, 137]. Although the assumed, scale free (with mild deviations), initial power spectra may be a generic prediction of the simplest scenarios of generation of perturbations during inflation, initial spectra with radical deviations are known to arise from very reasonable extensions, or, refinements to the simplest scenarios [22, 23, 139–144]. Consequently, cosmological parameter estimation from the CMB anisotropy and the matter power spectrum obtained from redshift surveys, weak gravitational lensing and Ly-α absorption, depends sensitively on the dimensionality, nature and freedom in the parameter space of initial conditions [145].

The angular power spectrum, C_l, is a convolution of the initial power spectrum $P(k)$ generated in the early universe with a radiative transport kernel, $G(l, k)$,

that is determined by the current values of the cosmological parameters. The remarkably precise observations of the angular power spectrum C_l by WMAP, and the concordance of cosmological parameters measured from different cosmological observations opens up the avenue to directly recover the initial power spectrum of the density perturbation from the observations.

The direct numerical deconvolution has clear advantages over the other prevalent approach of obtaining the most likely parameter values for a parametric model primordial spectra [1]. First, as emerges from our work, the direct method can reveal features that are not anticipated by the parametric model spectra, hence would be completely missed out in the latter approach. Second, in the absence of an accepted early universe scenario (more narrowly, a favored model of inflation), it is difficult to *a priori* set up and justify the chosen space of initial conditions. The complex covariances between the cosmological and the initial parameters are sensitive to the parameterization of the space of initial spectra adopted. Efforts along these lines are further obscured by issues such as the applicability of the Occam's razor to dissuade extension of the parameter space of initial conditions. Such deliberations have been recently framed in the more quantitative language of Bayesian evidence to evaluate and select between possible parameterizations [152]. However, this approach cannot really point to a preferred parameterization. Whereas, in the direct approach we can evade the issue of appropriate parameterization of the initial power spectrum.

In this chapter we show that the Richardson-Lucy(RL)deconvolution method is a promising and powerful method to measure the power spectrum of initial perturbations from the CMB angular power spectrum [146]. We have also devised and implemented an improvement to the RL scheme, whereby the iterative deconvolution algorithm is designed to converge and match the measurements only within the given error-bars.

Then we apply the method to the CMB anisotropy spectrum measured by WMAP. For a given set of cosmological parameters, our method obtains the primordial power spectrum that 'maximizes' the likelihood. Hence, the space of parameters remains that of the (more widely accepted and agreed up on) cosmological parameters alone. The most prominent feature of the recovered spectrum is a sharp infra-red cut-off on the horizon scale. It also has a localized excess just above the cut-off which leads to great improvement of likelihood over the simple

[1] Estimate of the power spectrum in k space 'bins' carried out with WMAP data is a somewhat model independent [147–149]. Direct deconvolution with different method [150] has been attempted [151].

monotonic forms of model infra-red cut-off spectra considered widely in the post-WMAP-1 literature. Interestingly, similar features were also detected by method of regularized least squares [153]. The significant improvement in the likelihood clearly shows the importance of features in the primordial power spectrum.

Then, in the fifth section of this chapter, we demonstrate the application of wavelets in identifying the statistically significant features in a deconvolved power spectrum. We use Discrete Wavelet Transform (henceforth DWT) to identify features in the recovered primordial power spectrum at different resolutions and at different locations in k space. Starting from the coarsest primordial power spectrum we systematically add variations on different resolutions and obtain the angular power spectrum. We then compute the likelihood of the reconstructed primordial power spectrum by comparing the angular power spectrum with the WMAP data. The improvement in the likelihood allows us to quantify the significance of different features.

In the last part of this chapter we apply the method to the CMB anisotropy spectrum given by WMAP 3 year data. We employ Discrete Wavelet Transform (DWT) for smoothing the raw recovered spectrum from the binned data. In this work we first present detailed results of an automated computation of the primordial power spectrum for 6 distinct points in the cosmological parameter space for flat ΛCDM models using WMAP 3 year data. Each of these 6 points in the parameter space has specific characteristics of interest. We also present the preliminary results of the cosmological parameter estimation optimized over the form of the primordial spectrum in a coarsely sampled volume of the parameter space. In this case, instead of simply computing the likelihood for a given model of initial power spectrum, one obtains the initial power spectrum that maximizes the likelihood at a point and assigns that likelihood to that point in the space of cosmological parameters. However our results for the cosmological parameter estimation, have a coarse resolution in spacing of the parameters and is also limited in volume of the parameter space covered. In principle it is possible to extend this work to explore the "entire" space of cosmological parameters with high resolution along the lines being done routinely [2].

[2]It is possible that very unlikely cosmological parameters get picked out due to suitably tailored initial power spectrum. In this case, one can employ appropriately strong priors from other observation or beliefs to ensure that unlikely, unphysical, ill-motivated are down weighted.

3.2 Method of reconstruction

3.2.1 Integral equation for CMB anisotropy

In this subsection we recall the integral equation for the angular power spectrum of CMB anisotropy and set up the inverse problem that we solve using a deconvolution method. The observed CMB anisotropy $\Delta_T(\mathbf{n})$ is one realization of a random field on the surface of a sphere and can be expressed in terms of the random variates a_{lm} that are the coefficients of a Spherical Harmonic expansion given by

$$\Delta_T(\mathbf{n}) \;=\; \sum_{l=2}^{\infty} \sum_{m=-l}^{m=l} a_{lm}\, Y_{lm}(\mathbf{n}) \tag{3.1}$$

where $Y_{lm}(\mathbf{n})$ are the Spherical Harmonic functions. For an underlying isotropic, Gaussian statistics, the angular power spectrum, C_l defined through

$$\langle a_{lm} a^*_{l'm'} \rangle = C_l \delta_{ll'} \delta_{mm'}\,, \tag{3.2}$$

completely characterizes the CMB anisotropy.

In a flat universe the temperature fluctuation in the CMB photons at the location $\mathbf{x}$ at the present conformal time η_0 propagating in a direction $\mathbf{n}$ is

$$\Delta(\mathbf{n}) \equiv\; \Delta(x_0, \mathbf{n}, \eta_0) \;=\; \int d^3k\, e^{i\,\mathbf{k}\cdot\mathbf{x}}\, \Delta(k, \mathbf{n}, \eta_0). \tag{3.3}$$

For globally isotropic cosmology, the temperature fluctuation $\Delta(\mathbf{k}, \mathbf{n}, \eta_0) \equiv \Delta(\mathbf{k}\cdot\mathbf{n}, \eta_0)$ can be expanded in terms of Legendre polynomials leading to

$$\Delta_T(x, \mathbf{n}, \eta_0) \;=\; \int d^3k\, e^{i\,\mathbf{k}\cdot\mathbf{x}} \sum_{l=0}^{\infty} (-i)^l\, (2l+1) \Delta_l(k, \eta_0) P_l(\mathbf{k}\cdot\mathbf{n})\,. \tag{3.4}$$

The angular power spectrum C_l given by the coefficients of Legendre expansion is then expressed as

$$C_l \;=\; (4\pi)^2 \int \frac{dk}{k}\, P(k)\, |\Delta_{Tl}(k, \eta_0)|^2 \tag{3.5}$$

where $P(k)$, the power spectrum of the *primordial (scalar) metric* initial perturbation $\psi_{\rm prim}$, is given by

$$\langle \psi_{\rm prim}(\mathbf{k})\, \psi^*_{\rm prim}(\mathbf{k'}) \rangle \;=\; \frac{P(k)}{k^3}\, \delta(\mathbf{k} - \mathbf{k'}) \tag{3.6}$$

because the k space modes are uncorrelated in a homogeneous space. The spectrum $P(k)$ represents the *r.m.s.* power in the scalar metric perturbations per logarithmic interval dk/k at a wavenumber k. It is related to power spectrum of the primordial modes of density perturbations, δ_k, as $P(k) \propto |\delta_k|^2/k$. For the conventional scale free parameterization, the spectral index n_s is defined through $|\delta_k|^2 = Ak^{n_s}$. The power spectrum $P(k)$ is a constant for the scale invariant Harrison-Zeldovich spectrum (corresponds to $n_s = 1$).

The harmonics of the temperature fluctuations at the current epoch, $\Delta_{Tl}(k, \eta_0)$, is obtained from the solution to the Boltzmann equation for the CMB photon distribution. In this work we use $\Delta_{Tl}(k, \eta_0)$ computed by the CMBfast software [154]. Numerically, a suitably discretized space of wave-numbers, k_i is used where the following discrete version of integral eqn (3.5) is applicable

$$C_l = \sum_i G(l, k_i)\, P(k_i)$$

$$G(l, k_i) = \frac{\Delta k_i}{k_i} |\Delta_{Tl}(k_i, \eta_0)|^2 . \tag{3.7}$$

In the above equation, the *'target'* angular power spectrum, $C_l \equiv C_l^D$, is the data given by observations, and the radiative transport kernel, $G(l, k)$ is fixed by the cosmological parameters of the *'base'* model. (The kernel $G(l, k)$ also includes the effect of geometrical projection from the three dimensional wavenumber, k, to the harmonic multipole, l on the two dimensional sphere.) For a given $G(l, k)$, obtaining the primordial power spectrum, $P(k)$ from the measured C_l is clearly a deconvolution problem. An important feature of our problem is that C_l^D, $G(l, k)$ and $P(k)$ are all positive definite. However, to get reliable results from the deconvolution, we require high signal to noise measurements of C_l^D over a large range of multipoles with good resolution in multipole, preferably, from a single experiment to avoid the uncertainties of relative calibration [3].

Ideally, it will be best to measure each C_l^D independently. In practice, incomplete sky coverage and other effects limit the resolution in multipole space. All experiments provide band power estimates, $\bar{C}_b(l_{\rm eff}) = \sum_l W_l^{(b)} C_l$ which are averaged linear combinations of the underlying C_l. Since eqn (3.7) is linear, a similar

[3] Binned C_l^D data that combined the heterogeneous CMB band power obtained from different experimental data sets are not always as reliable due to relative calibration uncertainties. Application of our method to binned data of [155] did not give robust or convincing results [146]. However, in principle nothing rules out using binned data from heterogeneous data sets that have good cross-calibration.

equation holds for all the band powers with a kernel, $\bar{G}(l_{\rm eff}, k_i) = \sum_l W_l^{(b)} G(l, k_i)$. For simplicity and brevity of notation, we retain the notation C_l^D and $G(l,k)$ for band power estimates with l denoting the bin center. We also implicitly assume a discrete wavenumber k instead of carrying the clumsy notation, k_i.

As mentioned in more detail in section 3.3.1, the CMB angular power spectrum from WMAP ranges from the quadrupole, $l = 2$ to 1000. Moreover, the 'full sky' coverage of WMAP implies good resolution in multipole space. We use WMAP TT (temperature-temperature) binned power spectrum as C_l^D in eqn (3.7). We use CMBfast software to compute the the $G(l,k)$ matrix for the post-WMAP 'best fit' cosmological parameters. We emphasize that although the $P(k)$ is recovered using binned data, the significance (performance) of the recovered spectrum is evaluated using the WMAP likelihood of entire unbinned C_l properly accounting for covariances. The likelihood is computed using the numerical code, data and its error covariance provided by the WMAP collaboration with the release of the first year and three year data.

In this work we limit our attention to the angular spectrum of the temperature anisotropy, C_l^{TT}. Including the polarization of CMB photons, equations similar to eqn (3.5) can be also written for the three additional angular power spectra, C_l^{TE}, C_l^{EE} and C_l^{BB} involving their corresponding kernels. It will certainly be interesting to include these when more complete polarization data is available in the future. At present, the C_l^{TE} and C_l^{EE} spectrum published by the WMAP team are not of a very good quality hence, not ideally suited for our method. However, once C_l^{EE} data is made available with a high quality, our method can readily accommodate both C_l^{TE} and C_l^{EE} together since combinations such as $C_l^{TT} \pm 2C_l^{TE} + C_l^{EE}$ are positive definite [4].

3.2.2 Deconvolution method

The Richardson-Lucy (RL) algorithm was developed and is widely used in the context of image reconstruction in astronomy [156, 157]. However, the method has also been successfully used in cosmology, to deproject the 3-D correlation function and power spectrum from the measured 2-D angular correlation and 2-D power spectrum [158, 159]. We employ an improved RL method to solve the inverse problem for $P(k)$ in eqn (3.7). The advantage of RL method is that positivity of the

[4] Recently the "QUAD" CMB data [202] got released which provides a high resolution polarization data and it seems to be proper for our purpose as a future work.

recovered $P(k)$ is automatically ensured, given $G(l,k)$ is positive definite and C_l's are positive.

The RL method is readily derived from elementary probability theory on distributions [156]. To make this connection, we consider normalized quantities [5]

$$\sum_l \tilde{C}_l \;=\; 1; \quad \sum_k \tilde{P}(k) \;=\; 1; \quad \sum_l \tilde{G}(l,k) \;=\; 1\,. \tag{3.8}$$

This allows us to view the functions, $P(k)$ and C_l as one dimensional distributions, and $G(l,k)$ as a conditional probability distribution. Further, for convenience (not necessity) of writing an infinitesimal measure dl we view l to be continuous. The integrand in the integral eqn (3.5) suggests defining two other probability distributions $Q(l,k)$ and $L(l,k)$, such that

$$G(l,k)\,P(k)\,dldk \;=\; Q(l,k)\,dldk \;=\; L(k,l)\,C_l\,dldk \tag{3.9}$$

Dividing the both side of eqn (3.9) by $C_l\,dldk$ we obtain

$$L(k,l) \;=\; \frac{P(k)}{C_l}\,G(l,k)\,. \tag{3.10}$$

The normalization conditions imply

$$P(k) \;=\; \int Q(l,k)\,dl \;=\; \int C_l\,L(k,l)dl\,, \tag{3.11}$$

which in the discrete l space reads

$$P(k) \;=\; \sum_l Q(l,k) \;=\; \sum_l L(k,l)\,C_l\,. \tag{3.12}$$

The RL method iteratively solves the eqns (3.10) and (3.12). Starting from an initial guess $P^{(0)}(k)$, L is obtained using eqn (3.10) as the first step. The second step is to obtain a revised $P^{(1)}(k)$ using eqn (3.12). These two steps are repeated iteratively with the $P^{(i)}(k)$ obtained after iteration i feeding into the iteration $i+1$. In principle, the final answer could depend on the initial guess but in practice, for a large variety of problems, RL is known leads to the correct answer even a crude estimation of the initial guess. In particular, for our problem the RL rapidly converges to the same solution $P(k)$ independent of the initial guess $P^{(0)}(k)$. This is demonstrated in

[5] In what follows we assume that the quantities are normalized and omit the overhead tilde in the notation. The normalization to unity not required and it is possible to use other normalizations, such as, $\sum(2l+1)C_l = constant$.

Appendix D.1.

The iterative method can be neatly encoded into a simple recurrence relation. The power spectrum $P^{(i+1)}(k)$ recovered after iteration $(i+1)$ is given by

$$P^{(i+1)}(k) - P^{(i)}(k) \;=\; P^{(i)}(k) \sum_l G(l,k)\, \frac{C_l^D - C_l^{(i)}}{C_l^{(i)}} \tag{3.13}$$

where C_l^D is the measured data (target) and $C_l^{(i)}$ is the angular power spectrum at i^{th} iteration obtained from eqn (3.7) using the recovered power spectrum $P^{(i)}(k)$. Eqn (3.13) with eqn (3.7) for obtaining $C_l^{(i)}$ from $P^{(i)}(k)$ completely summarizes the standard RL method.

Due to noise and sample variance, the data C_l^D is measured within some non-zero error bars σ_l. The standard RL method does not incorporate the error information at all. Consequently, a well known drawback of the standard RL method is that at large iterations the method starts fitting features from the noise. Modified forms of RL that address this issue have been proposed (e.g., see damped RL method in [160]). In our problem, this problem manifests itself as very non-smooth deconvolved spectrum $P(k)$ that has poor likelihood with the full WMAP spectrum data. We devise a novel method to make the RL method sensitive to the error σ_l by modifying eqn (3.13) to

$$P^{(i+1)}(k) - P^{(i)}(k) \;=\; P^{(i)}(k) \sum_l G(l,k)\, \frac{C_l - C_l^{(i)}}{C_l^{(i)}} \;\; \tanh^2\left[\frac{(C_l^D - C_l^{(i)})^2}{{\sigma_l}^2}\right]. \tag{3.14}$$

The idea is to employ a 'convergence' function to progressively weigh down the contribution to the correction $P^{(i+1)} - P^{(i)}$ from a multipole bin where $C_l^{(i)}$ is close C_l^D within the error bar σ_l. This innovation significantly improves the WMAP likelihood of the deconvolved spectrum. For certain $G(l,k)$, the improvement is so dramatic that using IRL becomes very crucial to successful recovery of the spectrum (see section 3.3.3). The final results are not sensitive to the exact functional form of the convergence function. The choice given in eqn (3.14) works well but is not unique in any sense.

At every iteration of the IRL scheme, we compute the χ^2 of the $C_l^{(i)}$ with respect to the binned data C_l^D. We have found that the IRL iterations (as well as the RL) march almost monotonically toward improved (smaller) χ^2. We halt the iterations when the χ^2 does not change appreciably in subsequent iterations of IRL.

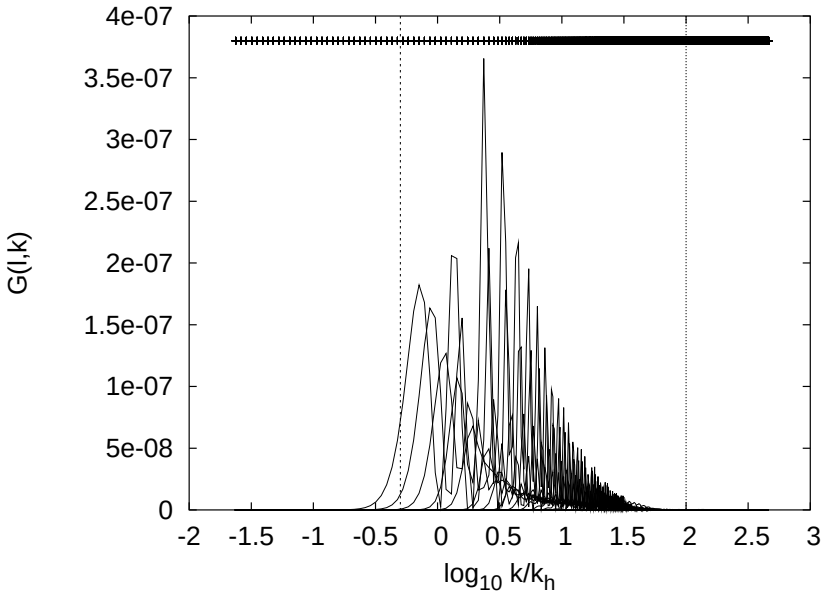

Figure 3.1: The curves are $\bar{G}(l,k)$ versus wavenumber k used in our work. $\bar{G}(l,k)$ is averaged over $G(l,k)$ within multipole bins used by WMAP. The two vertical lines roughly enclose the region of k-space strongly probed by the kernel where the primordial spectrum can be expected to be recovered reliably. The k-space sampling used is indicated by the line of '+' symbols at the top of the plot.

3.2.3 Post processing the deconvolved spectrum

The deconvolution algorithm produces a 'raw' $P(k)$ that has to be processed further. The raw deconvolved spectrum has spurious oscillations and features arising largely out of the k space sampling and binning in l space. These numerical artifacts are common to all recovered spectra recovered with same $G(l,k)$. Figure 3.1 shows the plot of the binned kernel $G(l,k)$ for the l-space bins used by WMAP [134, 135]. The wavenumbers are scaled by horizon scale, $k_h = 2\pi/(\eta_0 - \eta_{\rm rec})$. The sampling of k space used here is also indicated in the figure. We find that removing these artifacts and smoothing the resultant spectrum improves the WMAP likelihood of the corresponding C_l.

We illustrate the steps of removing the numerical artifacts and smoothing with test case examples of synthetic C_l from known test primordial spectrum. The first column of figure 3.2 shows the 'raw' spectrum obtained. A comparison with the known spectra shows similar numerical noise and artifacts in all the cases, especially, the rise at very low and very high wave numbers. As shown in appendix D.3, the main artifacts at the low and high k ends can be understood and modeled

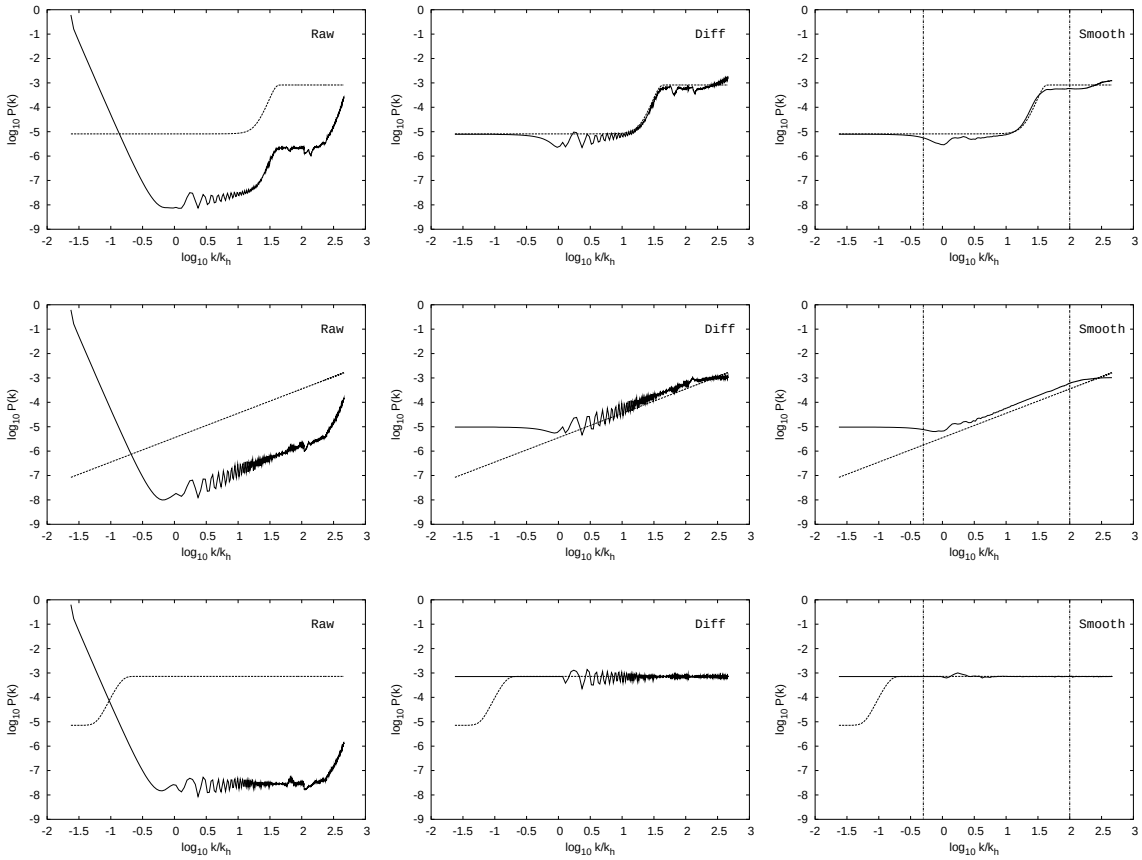

Figure 3.2: Each of the three rows in the panel of figures illustrates the recovery the primordial power for a test case using C_l arising from a known non-scale invariant primordial spectrum. The first column compares the raw deconvolved spectrum with the input spectrum. Note the similar artifacts in the all the raw spectra at the low and high k end discussed in the text. The feature is outside the range of $G(l,k)$ and is completely missed in the third case. The second, column is the differenced spectrum obtained by dividing out by a raw reference spectrum. The differenced spectrum resembles the input spectrum (top two cases) with small oscillations. The third column shows that the final recovered spectrum obtained by smoothing the differenced spectrum matched the input spectrum very well.

analytically. However we find it easier to remove them constructing a numerically generated template reference spectrum that also takes care of small features which appear due to changes in the k spacing. To remove these numerical artifacts, we generate a synthetic C_l using a Harrison-Zeldovich spectrum and then apply the deconvolution method to recover a 'reference' spectrum $P_{\rm ref}(k)$. We divide every 'raw' spectrum by $P_{\rm ref}(k)$ to obtain a 'differenced' spectrum that does not have numerical artifacts as seen in middle column ("diff.") of figure 3.2.

The difference spectra are a noisy version of the test spectra. Hence, the exercise with the test spectra suggests that the differenced spectrum needs to be 'suitably' smoothed to recover the true power spectrum. A simple smoothing procedure with simple fixed width window function leads to a satisfactory recovery of the test spectrum. (A 'Bowler hat' window constructed with hyperbolic tangent functions is used for smoothing.)

The last column in figure 3.2 shows the remarkably successful recovery of the test spectra in the top two case. As expected, the $P(k)$ is recovered best in the k space (within the vertical lines in bottom row of figure 3.2) where the kernel $G(l,k)$ is significant (marked by the vertical lines in figure 3.1 and 3.2). In the bottom row, the feature in the test spectrum is outside the range of the kernel $G(l,k)$, and, as expected, the recovery process misses it completely. For the top row, if we ignore the region where there is no power for $G(l,k)$ the recovered spectrum is well matched with the test spectrum. The match may be further improved by using more elaborate, adaptive smoothing procedure.

For application to real data, the phrase 'suitable smoothing procedure' may appear ambiguous. But the smoothing is in fact very well defined for real data by demanding that the smoothed $P(k)$ produces a theoretical C_l that has higher likelihood given the data. We find that this approach works extremely well. The deconvolution algorithm uses the binned C_l data, hence the theoretical C_l corresponding to the recovered $P(k)$ fits the binned data very well. However, the WMAP likelihood of the theoretical C_l suffers owing to spurious oscillations in the differenced spectra. The WMAP likelihood improves as the differenced spectra, $P_{\rm diff}(k)$ is smoothed. We smooth the differenced spectrum so that WMAP likelihood of the corresponding theoretical C_l is maximized. Although it is difficult to establish that the final result is the unique solution with maximum likelihood, in practice, our simple scheme does lead to a well defined result (no distinct degenerate solutions were found). Since our smoothing procedure is simple minded, possible avenues for improvement with more elaborate smoothing procedure remain open. Work is

in progress to employ wavelet decomposition for the smoothing procedure.

3.3 Application to the WMAP CMB anisotropy spectrum

In this part we apply the method described in the previous section to the angular power spectrum obtained with the first year of WMAP data publicly released in February 2003 [133] to recover the primordial power spectrum. In section 3.3.1, the publicly available WMAP data and how it is used in our work is discussed. We also describe the choice of the 'base' cosmological model. The recovered primordial power spectrum for this model is presented in section 3.3.2. The next section 3.3.3 presents the effect of varying the cosmological parameters (within 1 σ error bars) on the recovered primordial power spectrum. We also present the primordial spectrum for a set of cosmological models with large optical depths ($\tau = 0.1, 0.17, 0.25$) corresponding to possible the early reionization scenarios suggested by the WMAP temperature-polarization (TE) cross-spectrum.

3.3.1 WMAP anisotropy spectrum and the cosmological model

Accurate measurements of the angular power spectrum of CMB anisotropy was derived from the first year WMAP data [134]. The spectrum obtained by averaging over 28 cross-channel power measurements is essentially independent of the noise properties of individual radiometers. The power at each multipole ranging from $l = 20$ to 900 was estimated together with the covariance [6]. The instrumental errors are smaller than the cosmic variance up to $l \sim 350$, and the signal to noise per mode is above unity up to $l \sim 650$.

The angular power spectrum estimate and covariance matrix are publicly available at the LAMBDA data archive [7]. The WMAP team has also made available a suite of F90 codes that computes the likelihood for a given theoretical C_l spectrum given the full angular power spectrum included the covariance measured by WMAP. We use the TT likelihood code for computing the likelihood of C_l obtained from the recovered power spectrum and refer to these numbers as the 'WMAP likelihood'.

In addition, the WMAP team has also obtained a binned angular power spectrum where an average C_l is defined over bins in multipole space. The binned C_l

[6] The C_l are uncorrelated for an ideal full-sky map, but in practice, the covariances between neighboring multipole arise due to non-uniform/incomplete sky coverage, beam non-circularity, etc..

[7] Legacy Archive of Microwave Background DAta – http://lambda.gsfc.nasa.gov/

estimates can be treated as independent data points since the covariance between binned estimates is negligible. We use this binned spectrum as C_l^D in the deconvolution of eqn (3.7). (We are aware of but do not consider the revised estimates of the low multipoles made by other authors after the WMAP results [161, 162])

The variance of C_l measurements is given by

$$\sigma_l^2 = \frac{2}{(2l+1)f_{\rm sky}} \left[C_l^T + \sigma_N^2 \omega_p^2 B_l^{-2}\right]^2 , \tag{3.15}$$

where σ_N is the noise per pixel, ω_p the angular pixel size, $f_{\rm sky}$ is the fraction of sky covered and B_l is the transform of the experimental beam [163]. It is important to note that contribution to the error from cosmic variance is proportional to the underlying theoretical/true C_l^T spectrum. To obtain the total error bars σ_l used in the IRL deconvolution eqn (3.14), we should add the cosmic variance for the theoretical $C_l^{(i)}$ to the the statistical error bars given with the binned data. However, $C_l^{(i)}$ rapidly iterates to C_l^D within the error bars in the IRL method and the simpler option of using C_l^D instead $C_l^{(i)}$ for computing the cosmic variance works equally well since σ_l in eqn (3.14) simply regulates the convergence of IRL [8].

We consider a flat Λ-CDM universe, with Hubble constant, $H_0 = 71\,{\rm km.s^{-1}/Mpc.}$, Baryon density, $\Omega_b h_0^2 = 0.0224$, a cosmological constant corresponding to $\Omega_\Lambda = 0.73$, with the remaining balance of matter to critical density in cold dark matter. This is the 'concordance' cosmological model suggested by the WMAP parameter estimation. While we mainly focus attention on a cosmological model without early reionization (optical depth to reionization, $\tau = 0$) we do present in section 3.3.3 the recovered primordial spectra for models with early reionization with opacity going up to $\tau = 0.25$. The case for a large optical depth τ comes from the temperature-polarization cross correlation. For simplicity, we limit ourselves to the temperature anisotropy spectrum and avoid undue attention to the cosmology suggested by the yet incomplete polarization data. The polarization spectrum is expected to be announced by WMAP soon. It is then easy to extend our method to include both the temperature and polarization anisotropy spectra.

[8] The contribution to the error from cosmic variance given in the WMAP binned power data is computed using the C_l^T for the best fit Λ-CDM model with a power law primordial spectrum. Our error bars are computed using C_l^D.

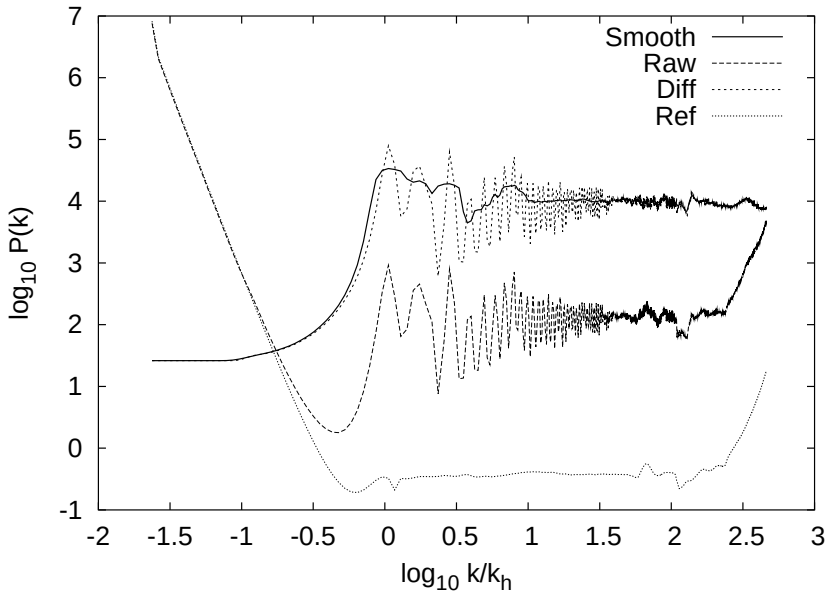

Figure 3.3: The three stages leading to the final recovered spectrum for a base cosmological model ($\tau = 0.0$, $h = 0.71$, $\Omega_b h^2 = 0.0224$ and $\Omega_\Lambda = 0.73$) is shown. The lower dashed line is the raw deconvolved power. The upper dashed line is the differenced spectrum obtained by dividing out by the reference spectrum shown as a dotted line. The solid line is the final result after smoothing that gives the best likelihood. Here we have used WMAP 1 year data.

3.3.2 Primordial power spectrum from WMAP

We apply the method described in the previous section to the WMAP data. Figure 3.3 shows the raw deconvolved spectrum, the reference spectrum, the differenced spectrum and the final recovered spectrum after smoothing obtained at each step of our method outlined in section 3.2.2.

We discuss the advantage of using improved Richardson-Lucy (IRL) in appendix D.2. The effect of IRL method is also evident in figure 3.4. The C_l from the recovered $P(k)$ matches the binned C_l^D only within the error-bars. The C_l spectrum corresponding to the differenced and smoothed $P(k)$ is shown in figure 3.4. Although, the former has better χ^2 for the binned data, the WMAP likelihood of the latter is much better. The poor likelihood of the differenced spectrum arises because there is no check on fluctuations in C_l at intermediate multipoles between the bin centers arising from the spurious numerical effects of k-space and l-space sampling. Better WMAP likelihood is more relevant than good χ^2 for the binned data since the former incorporates the estimation of each C_l and the full error covariance. Thus the smoothing step our method is carried out with a well defined goal of maximizing

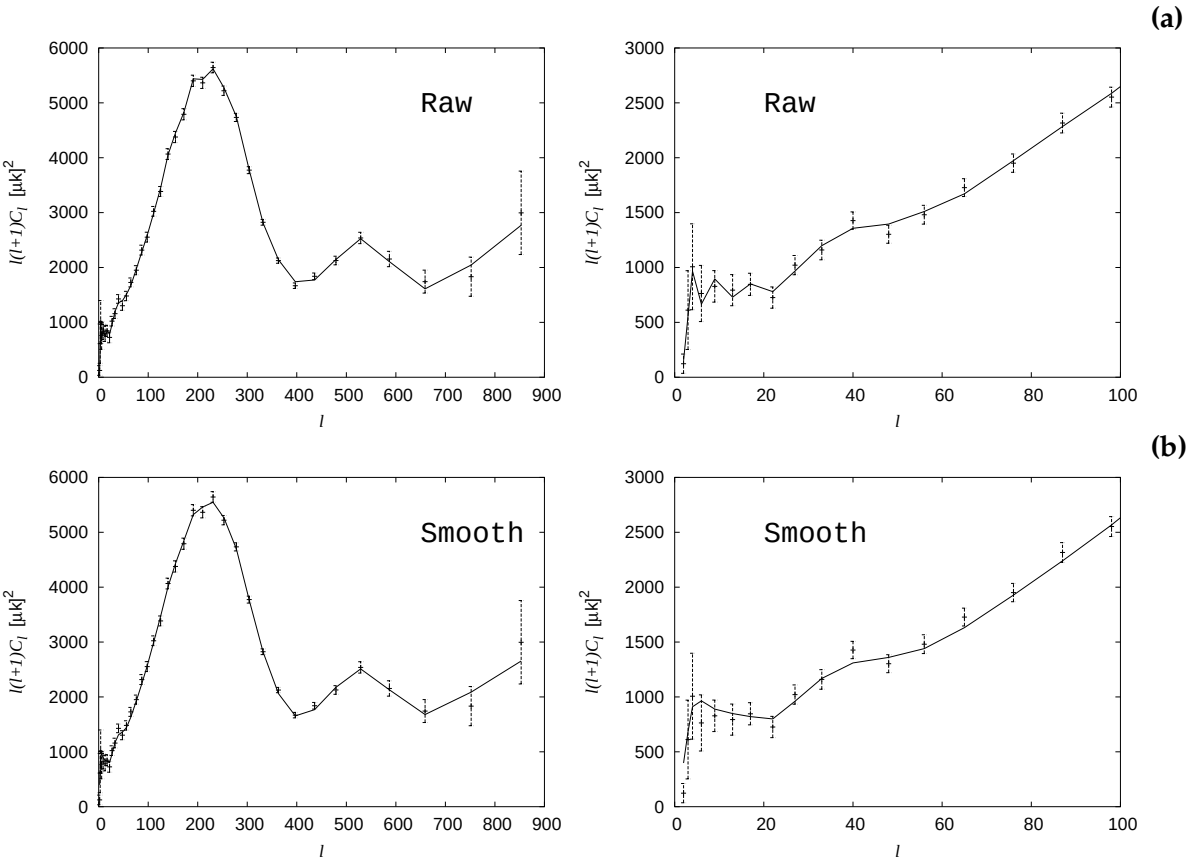

Figure 3.4: The recovered C_l corresponding to the raw $P(k)$ are shown in the upper row and that corresponding to the final smoothed $P(k)$ spectrum are shown in the lower row. The left panels show the full range of multipole, while the right hand panels zoom into the low multipoles. The C_l's from the raw as well as final $P(k)$ fit the binned C_l^D well ($\chi^2 \sim 10$ and $\chi^2 \sim 20$, respectively for 38 points). However, the jagged form of the C_l between the l bins (apparent in the low multipoles on the right) leads to poor WMAP likelihood for the C_l from the raw $P(k)$. The differencing and smoothing procedure irons out the jagged C_l dramatically improving the WMAP likelihood for the final smoothed $P(k)$. The WMAP likelihood is more relevant since it incorporates the estimation of each C_l and the full error covariance. Here WMAP 1 year data have been used.

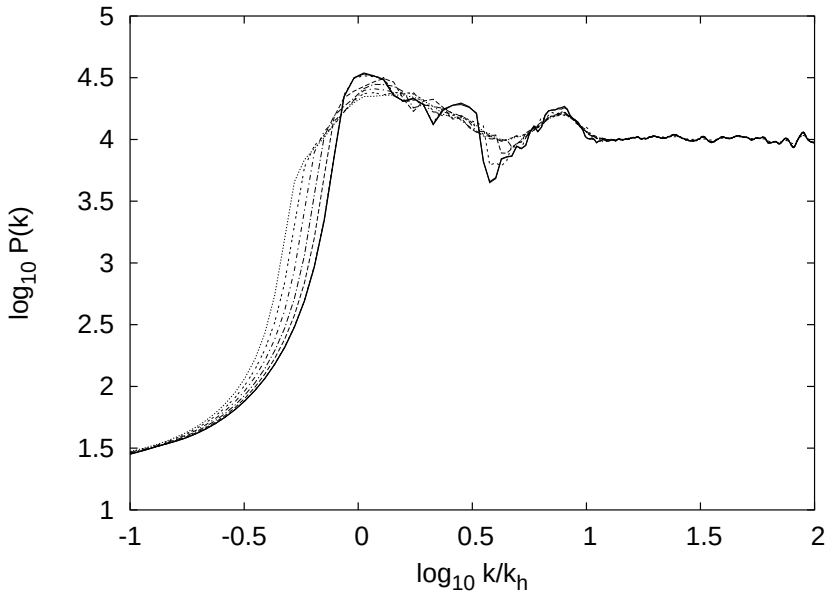

Figure 3.5: The final recovered spectrum for the base cosmological model ($\tau = 0.0, h = 0.71$, $\Omega_b h^2 = 0.0224$ and $\Omega_\Lambda = 0.73$) is compared with set of $P(k)$ with WMAP likelihood within $\sim 2\ \sigma$. The thick line gives the best likelihood equal to -478.2 and the other lines gives the likelihood bigger than -480. We can see that the sharp infra-red cut off is common to all these recovered spectra. The infra-red cutoff is remarkably close to the horizon scale and appears to be a robust feature. Another significant and robust feature is the bump just above the cut-off (reminiscent of the oscillation from under-damped transient). The difference between these spectra are in the smoothing and removing the noises from the raw deconvolved spectrum. Here WMAP 1 year data have been used.

the WMAP likelihood.

The primordial spectra recovered from WMAP data is again shown in figure 3.5. The dark solid line is the primordial spectrum that has the best WMAP log-likelihood of $\ln \mathcal{L} = -478.20$ for the base cosmological model described in the previous section. The other lines have likelihood $\ln \mathcal{L} > -480$, i.e., roughly within $2\ \sigma$ of the best one. For comparison, the same cosmological model with a scale invariant (Harrison-Zeldovich) primordial spectrum has $\ln \mathcal{L} = -503.6$, and, with a tilted scale free primordial spectrum $n = 0.95$, the likelihood improves to $\ln \mathcal{L} = -489.3$. (A comparison of likelihood numbers for various primordial spectra is given in table 3.1.) The improvement in likelihood for the recovered spectra is striking.

The most prominent feature of the recovered spectrum is the infra-red cutoff in the power spectrum remarkably close to the horizon scale ($k_c \sim k_h \equiv 2\pi/\eta_0$) chiefly in response to the low quadrupole measured by WMAP. Another notable point is

Table 3.1: The effective chi-square, $\chi^2_{\rm eff} \equiv -2\ln\mathcal{L}$, of the C_l corresponding our recovered spectrum is compared with a number of model primordial spectrum (with or without the infra-red cutoff. Limited attempt has been made to search for the best parameter values and the $\chi^2_{\rm eff}$ for the model spectra should be treated as indicative and are strictly upper bounds.

Power spectrum	$\chi^2_{\rm eff} \equiv -2\ln\mathcal{L}$	k_c/k_h[9] ($k_h = 4.5\times10^{-4}$Mpc.$^{-1}$)
Direct Recovered	956.76	0.71
Flat Harrison Zeldovich	1007.28	–
Power Law ($n_s = 0.95$)	978.60	–
Exponential cutoff ($n_s = 0.95$, $\alpha = 3.35$)	978.08	0.64
Exponential cutoff ($n_s = 0.95$, $\alpha = 10$)	977.84	0.64
Starobinsky break ($n_s = 0.95$, $r = 0.01$)	973.86	0.32
Vilenkin & Ford (VF-I) ($n_s = 0.95$)	976.88	0.43
Vilenkin & Ford (VF-II) ($n_s = 0.95$)	978.66	0.96

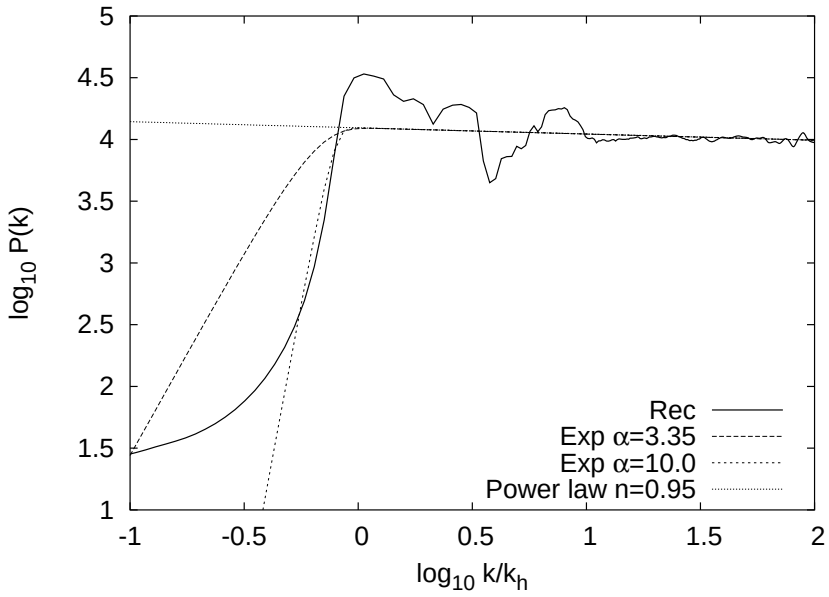

Figure 3.6: Comparison between our recovered $P(k)$ and exponential form of infra-red cut off to explain the suppressed quadrupole of WMAP angular power spectrum [21, 164]. We note that the infra-red cut-off of the recovered spectrum is very steep. The power excess just above the cutoff in the recovered is extremely significant in the remarkably enhanced likelihood. The power spectrum ($n = 0.95$) shows that our method does recover the preferred tilt obtained by WMAP team parameter estimation with power law spectrum [109]. The recovered $P(k)$ is based on WMAP 1 year data.

the slight tilt ($n \sim 0.95$) of the plateau in the recovered spectrum at large k which is consistent with the best fit n obtained by WMAP for power law primordial spectra. After the WMAP results, model power spectra with infra-red cutoffs of the form

$$P(k) \; = \; A_s \, k^{1-n_s} \left[1 - e^{-(k/k_*)^\alpha}\right] \tag{3.16}$$

invoked to explain the suppressed low multipoles of WMAP have had limited success [21, 164]. While the effective $\chi^2_{\rm eff} \equiv -2 \ln \mathcal{L}$ improved by at least 22 over a power law model, the model infra-red cutoff eqn (3.16) could improve the $\chi^2_{\rm eff}$ merely by ~ 3 [164]. Figure 3.6 compares the recovered spectrum with these model infra-red spectra. The power law spectrum shown in the figure also highlights the small tilt ($n \sim 0.95$) recovered by our method.

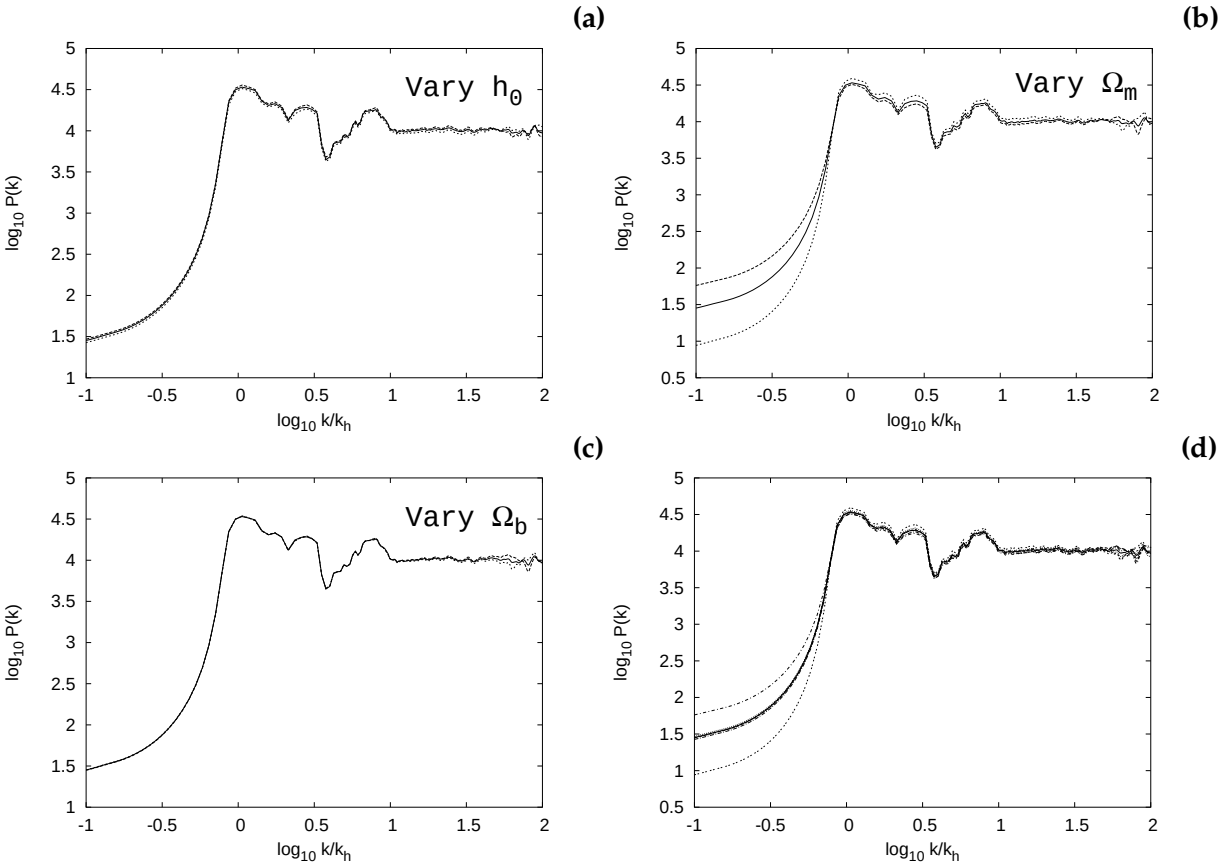

Figure 3.7: The panel of figures shows the robustness of the recovered $P(k)$ for variations in the cosmological parameters. Each parameter is varied within the 1 σ range indicated by the WMAP parameter estimates [109]. In figure (*a*), the Hubble constant $h_0 = 0.68$, $h_0 = 0.71$ and $h_0 = 0.75$ in the three curves. In figure (*b*) the values of vacuum density $\Omega_\Lambda = 0.69$, $\Omega_\Lambda = 0.73$ and $\Omega_\Lambda = 0.77$ in the three curves. In figure (*c*), the Baryonic density $\Omega_B = 0.040$, $\Omega_B = 0.044$ and $\Omega_B = 0.048$ in the three curves. The figure (*d*) combines all the distinct curves in other figures to give a consolidated perspective on the dependence of the recovered spectrum on cosmological parameters. Note that the x-axis is the wavenumber is scaled in units of the $k_h = 2\pi/\eta_0$ which reduces the scatter considerably in the curves for variations in H_0 and Ω_Λ.

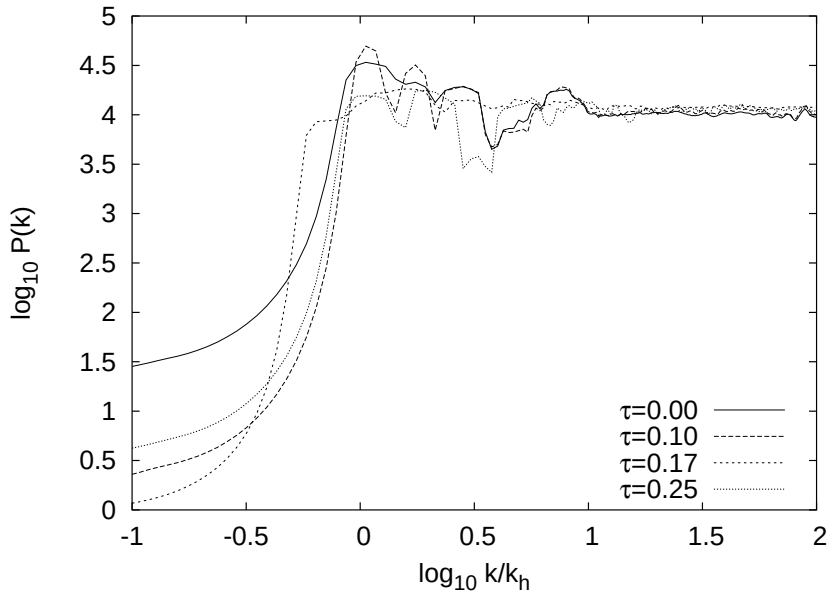

Figure 3.8: The recovered $P(k)$ for different values of optical depth ($\tau = 0.00, 0.10, 0.17$ and 0.25). The width of smoothing used is different for different cases. This is the main cause of the small shift in the location of the infra-red cutoff. Here we have used WMAP 1 year data.

3.3.3 Dependence on the cosmological parameters

The primordial spectrum is recovered for a set of 'best fit' cosmological parameters defining the 'base' model. We have varied each cosmological parameter by the quoted 1 σ error-bars of the WMAP estimates [109]. Figure 3.7 shows the dependence of the recovered power spectrum on small changes to cosmological parameters varied one at a time keeping the others fixed at their central value. We find that recovered spectrum is insensitive to variations Hubble constant, H_0, modulo an overall shift due to the change in the horizon size, η_0. The WMAP likelihood of the corresponding C_l are $\ln \mathcal{L} = -477.79$ and -478.83 at $h_0 = 0.68$ and 0.75, respectively. The variation of Baryon density around its middle value $\Omega_B = 0.044$ yields almost identical primordial power spectra with a minor change in likelihood – $\ln \mathcal{L} = -477.97$ and -478.53 for $\Omega_B = 0.040$ and $\Omega_B = 0.048$, respectively. The variation of Ω_Λ (or equivalently, Ω_m, for flat models) modulo a shift due to change in η_0, affects only the amplitude of the infra-red cut-off. The WMAP likelihood of the corresponding C_l are $\ln \mathcal{L} = -478.93$ and -478.25 for $\Omega_\Lambda = 0.69$ and $\Omega_\Lambda = 0.77$, respectively.

We note that the likelihood at the central values are not necessarily the best.

This suggests that, as it will be discussed later, one can explore the entire space of cosmological parameters and compute the likelihood after optimizing with 'best' recovered primordial spectrum.

Finally, we also consider the effect of a cosmological model with significant optical depth to reionization, $\tau = 0.17$, such as suggested by the angular power spectrum of the temperature-polarization (TE) cross correlation from WMAP [136]. It has been pointed out that the estimated τ increases when the primordial spectrum has an infra-red cut-off. We compute the primordial power spectrum for base cosmological models with $\tau = 0.10, 0.17, 0.25$. The standard RL deconvolution performs poorly for these models, and, the improved RL method was crucial for these models. Figure 3.8 compares the recovered primordial spectra for early reionization models which all show an infra-red cutoff at the horizon scale [10].

3.4 Theoretical implication of the recovered spectra

The direct recovery of the primordial power spectrum has revealed an infra-red cutoff of a very specific form. Model spectra with monotonic infra-red cutoff such as that in eqn (3.16) do not improve the WMAP likelihood significantly. While, to match the low value of the quadrupole, a very sharp cut-off (such as $\alpha \sim 10$, see figure 3.6) is required, such a steep monotonic cut-off tends to pull down the power in the next few higher multipoles above the quadrupole and octopole as well. Our recovered spectrum has a compensating excess which allows a steep cut-off to match the low quadrupole and octopole without suppressing the higher multipoles. Naively, one would think that a designer infra-red cutoff would 'cost' in the language of Bayesian evidence due to the introduction of extra parameters. That is is not necessarily so. An infra-red cut-off of the form we recover does not necessarily have more parameters than an infra-red cut-off of the form in eqn (3.16). Moreover, it is striking that the location of the cut-off is close to a well known scale – the horizon scale.

In this section we show that infra-red cut-off of the form we recover arises from very simple scenarios in inflation. We explicitly mention two of them. Starobinsky [22] has shown that a kink (sharp change in the slope) in the inflaton potential can modulate the underlying primordial power spectrum $P_0(k)$ with a step like feature at a wavenumber k_*, eqn (1.41),

[10] For simplicity and consistency, we use the same smoothing for these cases. Better result can be obtained for $\tau = 0.17$ with different smoothing.

$$P(k) \;=\; P_0(k)\; \mathcal{D}^2(y, R_*)\,.$$

In the simpler form we restrict $P_0(k)$ to be a simple power law. However, in general, $P_0(k)$ can be of any form allowed by models of scalar field driven inflation. The transfer function, eqn (1.42),

$$\mathcal{D}^2(y, R_*) \;=\; [1 - 3\,(R_* - 1)\,\frac{1}{y}\,((1 - \frac{1}{y^2})\sin 2y + \frac{2}{y}\cos 2y) \;+\; \frac{9}{2}(R_* - 1)^2\frac{1}{y^2}(1 + \frac{1}{y^2}) \;\times$$
$$(1 + \frac{1}{y^2} + (1 - \frac{1}{y^2})\cos 2y - \frac{2}{y}\sin 2y)]\,,$$

with $y = k/k_*$. R_* is the ratio of the slope $dV/d\phi$ before and after kink in the inflaton potential. The power spectrum $P(k)$ in eqn (1.42) has a step up (going to larger k) for $R_* < 1$ and a step down feature for $R_* > 1$. An infra-red cut off is created with $R_* < 1$. Figure 3.9 shows a spectrum with a Starobinsky step eqn (1.42) that can not only mimic the sharp infra-red cutoff but also produces the required bump after it. Table 3.1 shows that a introducing an appropriate Starobinsky step gives a very good WMAP likelihood compared to eqn (3.16). Besides the location of the break, k_*, the Starobinsky step spectrum has only another parameter R_* that fixes the slope and the depth of the cut-off as well as the size of the bump. We have not systematically searched through the parameter space to arrive at a 'best-fit' model. Hence, it may be possible to get even better match to the WMAP data with Starobinsky breaks. Similar scenarios have been studied earlier [165] and has also been pointed to in the post-WMAP literature [166]. Multiple scalar field inflation provide ample scope for generating features in the primordial spectrum [22, 23, 139–144] and has been been invoked to model a sharp cut-off at horizon scale (see eg., [167, 168]). More exotic origin of an infra-red cut off in the scalar spectrum have also been investigated [169, 170].

Another compelling theoretical scenario for generating a feature of the form we have recovered is well-known. It is well known that radiation, or matter dominated era prior to inflation does affect the primordial power spectrum on scales that 'exit the horizon' soon after the onset of inflation. For a pre-inflationary radiation dominated epoch the power spectrum was given by Vilenkin and Ford (VF) [23], eqn (1.44),

$$P(k) = A_s\, k^{1-n_s}\,\frac{1}{4y^4}\left|e^{-2iy}(1 + 2iy) - 1 - 2y^2\right|^2$$

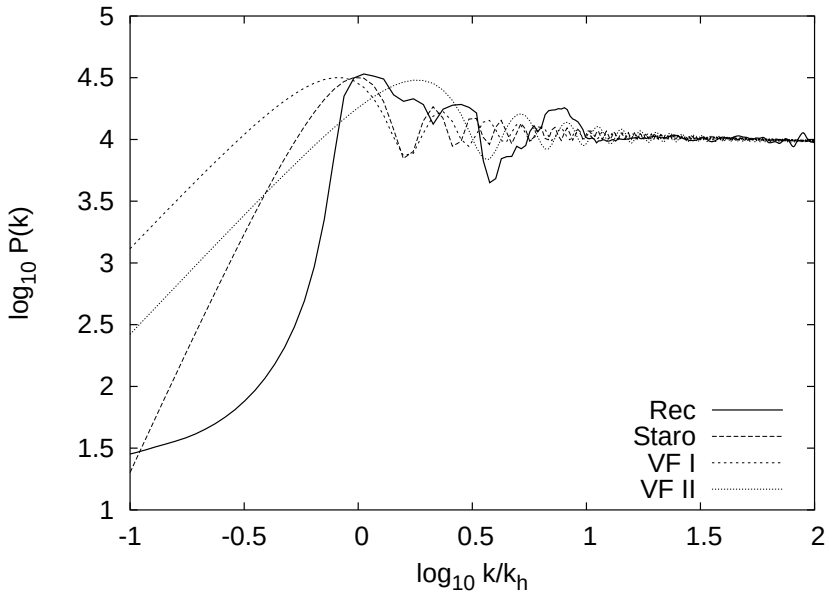

Figure 3.9: Comparison of our recovered $P(k)$ (solid) with the predictions two simple theoretical scenarios that remarkably match the gross features of the infra-red cutoff in the recovered spectrum. The 'staro' curve is the primordial spectrum when the inflaton potential has a kink– a sharp, but rounded, change in slope [22]. Fine tuning is involved in locating the kink appropriately. The 'VF' curves are the modification to the power spectrum from a pre-inflationary (here, radiation dominated) epoch [23]. This requires that the horizon scale, k_h, exits the Hubble radius very soon after the onset of inflation. Although, it appears fine tuned there is corroborating support for this within single scalar field driven inflation [171]. The theoretical $P(k)$ leads to C_l that enhanced WMAP likelihood given in table 3.1. The values of the parameters for the theoretical curves are given in the same table. The recovered $P(k)$ is based on WMAP 1 year data.

where $y = k/k_*$. Figure 3.9 shows that the VF spectrum eqn (1.44) can also provide an infra-red cutoff with required bump after it. Table 3.1 shows that a VF spectrum can give better WMAP likelihood compared to model spectra of the form eqn (3.16). The infra-red cut-off ($\propto k^2$) here is not very sharp. However, if the epoch prior to inflation is dominated by matter with some other equation of state, the slope would be different. A more complete analysis may give rise to spectra closer to the kind we have recovered. The scale k_* is set by the Hubble parameter at the onset of inflation. For this scenario to applicable to our results, the k_h-mode corresponding to the horizon scale must have crossed the Hubble radius very close to the onset of inflation. In a single scalar field inflation this would happen naturally [171].

Another possibility is that the infra-red cutoff arises due to non-trivial topology of the universe. A dodecahedral universe model that matches the low multipoles

of WMAP angular spectrum has been proposed [172]. However, non-trivial cosmic topology is expected to also violate the statistical isotropy of the CMB anisotropy and give rise of correlation features which are potentially detectable [173].

3.5 Wavelet analysis of the features in the recovered spectrum

In this section we analyze the features of the reconstructed primordial spectrum by using discrete wavelet transform.

3.5.1 Discrete wavelet transform

Wavelet transforms provide a powerful tool for the analysis of transient and non-stationary data and is particularly useful in picking out characteristic local variations at different resolutions. This linear transform separates a data set in the form of low-pass or average coefficients, which reflect the average behavior of the data, and wavelet or high-pass coefficients at different levels, which capture the variations at corresponding resolutions. As compared to Fourier or window Fourier transform, wavelets allow optimal "time-frequency" localization simultaneously in the real, as well as, Fourier domain. The vocabulary of DWT stems from applications in one dimensional time-stream signal trains, but has found wide application in signal in other domains and dimensions. Specifically in our case, the 'signal' being transformed is the power spectrum, $P(k)$, a one dimensional function of wavenumber, k.

Wavelets are an orthonormal basis of small waves, with their variations primarily concentrated in a finite region, which makes them ideal for analyzing localized 'transient' signals. Wavelets can be continuous or discrete. In the latter case, the basis elements are strictly finite in size, enabling them to achieve localization, while disentangling characteristic variations at different frequencies [174]. This is the primary reason for us to employ discrete wavelets for our analysis.

In the construction of the basis set for discrete wavelet transform, one starts with the scaling function $\varphi(x)$ (father wavelet) and the mother wavelet $\psi(x)$, whose height and width are arbitrary: $\int \varphi\, dx = A$, $\int \psi\, dx = 0$, $\int \varphi\, \psi\, dx = 0$, $\int |\varphi|^2\, dx = 1$, $\int |\psi|^2\, dx = 1$, where A is an arbitrary constant. In addition to the scaling and wavelet functions, their translates $\psi_{j,m} = 2^{j/2}\, \psi(2^j x - m)$, $\varphi_{j,m} = 2^{j/2} \varphi(2^j x - m)$, are also square integrable at different resolutions. Here, m and j respectively are the

translation and scaling parameters, both taking integral values with $-\infty \leq m \leq +\infty$. We start with the resolution value $j = 0$ and increase it by integral units. The original mother wavelet corresponds to $\psi_{0,0}$, and the father wavelet is given by $\varphi_{0,0}$. Higher values of j lead to the so called daughter wavelets which are of a similar form as the mother wavelet, except that their width and height differ by a factor of 2^j and $2^{j/2}$ respectively, at successive levels. The translation unit $m/2^j$ is also commensurate with the thinner size of the daughter wavelet at resolution j. In the limit $j \to \infty$, these basis functions form a complete orthonormal set. It needs to be pointed out that for a discrete data set with a finite number of points N the maximum value of j is the largest integer less than or equal to $\log_2 N$.

A signal $f(x)$ can then be expanded as

$$f(x) = \sum_{m=-\infty}^{+\infty} c_{0,m}\varphi_{0,m}(x) + \sum_{m=-\infty}^{+\infty}\sum_{j\geq 0} d_{j,m}\psi_{j,m}(x) \ . \tag{3.17}$$

Here, $c_{j,m}$'s are the low-pass coefficients and $d_{j,m}$'s are the high-pass or wavelet coefficients, respectively capturing the average part and variations of the signal at resolution j and location m. In practice, for a finite data set one starts with the highest level of resolution and progressively moves to resolution on grosser scales keeping in mind the physics of the problem and the size of the data set. The lowest level of resolution one chooses then corresponds to $j = 0$ and the higher levels correspond to larger values of j. For the discrete wavelets, the property of multi-resolution analysis (MRA) leads to $c_{j,m} = \sum_n h(n-2m)c_{j+1,n}$ and $d_{j,m} = \sum_n \tilde{h}(n-2m)c_{j+1,n}$, where $h(n)$ and $\tilde{h}(n)$ are respectively the low-pass (scaling function) and high-pass (wavelet) filter coefficients, which differ for different wavelets. Thus, both low-pass and high-pass coefficients at a resolution j can be obtained from the low-pass coefficients at a higher resolution $j + 1$. The low-pass coefficients $c_{j+1,m}$ are obtained though the convolution of the signal $f(x)$ with the scaling function $\varphi_{j+1,m} = 2^{(j+1)/2}\varphi(2^{j+1}x - m)$. For a fixed m, in the limit $j \to \infty$, the scaling function becomes a Dirac delta function and hence the corresponding low-pass coefficient is the signal itself at point m. This implies that, starting from the finest resolution of the signal, one can construct both scaling and wavelet functions, by convolution with the corresponding filter coefficients. Hence one can carry out the wavelet decomposition, as also the inverse transform, with the help of $h(n)$ and $\tilde{h}(n)$, without explicitly knowing the basis set. In this respect, wavelet transform is significantly different from the Fourier transform.

For the Haar wavelet, $h(0) = h(1) = \frac{1}{\sqrt{2}}$ and $\tilde{h}(0) = -\tilde{h}(1) = \frac{1}{\sqrt{2}}$. The Haar basis is unique, since it is the only wavelet which is symmetric and compactly supported. In a level one Haar wavelet decomposition, the level-I low-pass (average) and high-pass (wavelet or detail) coefficients are respectively given by the nearest neighbor averages and differences, with the normalization factor of $\frac{1}{\sqrt{2}}$. In the subsequent step, the average coefficients are divided into two parts, containing level-II high-pass and level-II low-pass coefficients. The high-pass coefficients now represent differences of averaged data points corresponding to a window size of two. Thus higher level coefficients represent lower frequency features. Wavelets belonging to the Daubechies family are designed such that the wavelet coefficients are independent of polynomial trends in the data. We have carried out a 10-level decomposition using Daubechies-4 wavelets for isolating fluctuations at different resolutions. Daubechies-4 wavelet satisfies $\int x\psi(x)dx = 0$, in addition to all other conditions. Because of this the wavelet coefficients capture fluctuations over and above the linear variations. Simple models of inflation predict that $\log P(k)$ vs $\log(k)$ will have a linear relation. The choice of Daubechies-4 wavelets is the *minimal* (simplest) wavelet that allows us to study variations about linear behavior in a window whose size increases with the level of decomposition.

Furthermore, to study the significance of features located at different wavenumbers and at different resolutions, fluctuations associated with wavelet coefficients of different levels are added to the average behavior captured by the low-pass coefficients in order to reconstruct a smoothened power spectrum. Then a likelihood analysis with respect to the WMAP data is performed.

If the data set is of size 2^N a maximum of N level decompositions can be carried out. In the case of fewer data points, one needs to supplement the data with additional points to carry out an N level decomposition. Due to the finite size of the filter coefficients, one also encounters boundary artifacts due to circular or other forms of extensions. In our case, for minimizing these boundary artifacts, we have carefully padded the data with constants at both ends, which were then removed after reconstruction. We worked with a data set of 8192 points for $\log P(k)$ vs $\log(k)$ recovered from WMAP-1 observations. The data set was arranged to be equally spaced, as required by wavelet programs.

3.5.2 Features of the primordial power spectrum

One of the most challenging questions of the modern cosmology is to find an inflationary scenario satisfying all the cosmological observations. The shape of the

primordial power spectrum has the key role in this investigation. In the previous sections we have used Richardson-Lucy deconvolution algorithm to find the shape of the primordial power spectrum using the cosmic microwave background data.

By using DWT, we decompose the recovered primordial power spectrum locally at different resolutions. We then calculate the angular power spectrum after including the variations in the primordial power spectrum at different resolutions. We subsequently compute the likelihood of the primordial power spectrum at each of these stages so as to quantify the effect of different features on the recovered angular power spectrum. We use WMAP-1 likelihood code available at the LAMBDA site and quote our likelihood $\mathcal{L}$ in terms of $\chi^2_{\rm eff} = -2\ln\mathcal{L}$.

The original primordial power spectrum which we use in this part is the final recovered primordial power spectrum obtained in the previous section (see figure 3.3) for a flat ΛCDM cosmological model with τ=0.0, h=0.71, $\Omega_b h^2$=0.0224 and Ω_Λ=0.73. The resultant C_l spectrum using this recovered spectrum has a likelihood far better than a scale invariant or a best fit power law spectrum. In this section we investigate how the features of this spectrum contribute to improving the likelihood.

First, we smooth the spectrum using DWT, and then we systematically include features at different resolutions and calculate the likelihood with respect to the WMAP data.

In figure 3.10, left panel (step A), we show the coarsest behavior of the data reconstructed using only the 10th level low-pass coefficients. The right panel shows the resultant C^r_l compared with the observed binned data C^d_l, and its error bars. The likelihood of the C^r_l at this stage corresponds to $\chi^2_{\rm eff}$ = 994.4 which is better than the $\chi^2_{\rm eff}$ for the H-Z spectrum. In the right panel (step B) we see that if we include 'low frequency' features as captured by the 10th level high-pass coefficients shown in the left panel (step B) to the previous spectrum at step A, the resultant C^r_l will be closer to the observed data. Hence we expect the likelihood to be improved. In fact this improves the likelihood significantly and the $\chi^2_{\rm eff}$ = 974.1 at this stage. This $\chi^2_{\rm eff}$ is better than the best fit power law spectrum with the $\chi^2_{\rm eff}$ = 978.6.

As we progressively add back more features at 'higher frequencies' to the spectrum the likelihood improves significantly. The 9th, 8th, 7th and 6th level wavelet coefficients are shown in the left column of figure 3.10 (steps C, D, E and F). The plots in the right panel of figure 3.10 show how we get closer to the observed data within the error bars as we include more wavelet coefficients. The likelihoods at these steps correspond to are $\chi^2_{\rm eff}$ = 964.8 at step C, $\chi^2_{\rm eff}$ = 961.0 at step D,

$\chi^2_{\rm eff}$ = 957.4 at step E, and $\chi^2_{\rm eff}$ = 956.5 at step F.

In figure 3.11 we compare the coarsest spectrum of step A and the spectrum after adding the features of step B, C and D. The local features which are responsible for the significant improvement of the likelihood are clearly seen. We note that most of these features are localized around the horizon scale. In figure 3.12, we see that after few stages of adding the more detailed features to the spectrum, the likelihood does not improve anymore and agreement with the observed data is not sensitive to these features.

3.6 Estimation of the primordial spectrum with post-WMAP 3 year data

The error-sensitive Richardson-Lucy (RL) method of deconvolution was shown in the previous sections to be a promising and effective method to recover the power spectrum of primordial perturbations from the CMB angular power spectrum. In this section, we have improved the deconvolution method by factoring out the normalization factors from the iteratively recovered primordial spectrum, $P(k)$, in the algorithm to remove the artifacts that were present at the two ends of the recovered spectrum in our previous work(corrected by template subtraction). For a given set of cosmological parameters, this method obtains the primordial power spectrum that 'maximizes' the likelihood to data.

In this part we apply the method to the CMB anisotropy spectrum given by WMAP 3 year data. We employ Discrete Wavelet Transform (DWT) for smoothing the raw recovered spectrum from the binned data. In this work we first present detailed results of an automated computation of the primordial power spectrum for 6 distinct points in the cosmological parameter space for flat ΛCDM models using WMAP 3 year data. Each of these 6 points in the parameter space has specific characteristics of interest. In continuation in the next section, we present the preliminary results of the cosmological parameter estimation optimized over the form of the primordial spectrum in a coarsely sampled volume of the parameter space. In this case, instead of simply computing the likelihood for a given model of initial power spectrum, one obtains the initial power spectrum that maximizes the likelihood at a point and assigns that likelihood to that point in the space of cosmological parameters. However our results for the cosmological parameter estimation, have a coarse resolution in spacing of the parameters and is also limited in volume of the parameter space covered. In principle it is possible to extend this

work to explore the "entire" space of cosmological parameters with high resolution along the lines being done routinely.

3.6.1 Modification in the deconvolution method

In this section we have improved the IRL method that we used the previous section to directly remove the artifacts at the two tails of the spectrum. Compared to our earlier implementation, we have eliminated the need to subtract a known model from the recovered spectrum to remove the artifacts at the two ends of the spectrum. We have achieved this by a slight change in the normalization procedure in the method, that corrects for the effect of very low amplitude of $G(l,k)$ at very small and very large k. In the previous section, the normalization factor ζ_k in eqn (3.18), was hidden in the finally deconvolved $P(k)$ and it was factored out at the end of the process. As we are dealing with an iterative process, every small artifact will affect the higher iterations more strongly. To avoid this, we separate the normalization factor ζ_k from the $P(k)$ from the beginning. This small modification gives rise to a big improvement in the method where the final form of the recovered spectrum is free from the artifacts at the two ends. Thus we do not need to use any template to remove these artifacts (as in the previous section). So in our revised iterative process we have modified eqn (3.14) to

$$P^{(i+1)}(k) - P^{(i)}(k) \;=\; P^{(i)}(k) \sum_l \tilde{G}(l,k)\,\zeta_k\,\frac{\tilde{C}_l^D - C_l^{(i)}}{C_l^{(i)}} \;\; \tanh^2\left[\frac{(\tilde{C}_l^D - C_l^{(i)})^2}{\tilde{\sigma}_l^2}\right], \qquad (3.18)$$

where the normalization factor, ζ_k, is explicitly present in the main iterative equation and we do not need to remove it from the final form of the $P(k)$ at the end of the process,

$$P(k) = P^{(n)}(k). \qquad (3.19)$$

The final form of the recovered spectrum was obtained after smoothing the spectrum by using Discrete Wavelet Transform.

In this part of our work, we use DWT to smooth the raw recovered spectrum obtained from the deconvolution using binned CMB spectrum data. The raw deconvolved spectrum has spurious oscillations and features arising largely due to the k space sampling and binning in l space. The main goal is to reconstruct the primordial spectrum which lead to an angular power spectrum with a high like-

lihood to the entire C_l data at each multipole including the covariance between them. The WMAP likelihood of the C_l suffers owing to the spurious oscillations in the spectra on scales smaller than l multipole space bins. The WMAP likelihood improves as the spectra, $P(k)$ is smoothed. We use DWT to smooth the recovered spectrum so that WMAP likelihood of the corresponding theoretical C_l is maximized. Strictly speaking, the best likelihood obtained in our method is a lower bound leaving open a mathematical possibility of obtaining a superior likelihood at the given point of the cosmological parameter space with a different primordial power spectrum [11]. Although it is difficult to establish that the final result is the unique solution with maximum likelihood, but numerous variations we have explored does suggest that it is perhaps very close to the best possible result. So we can claim that the improved reconstructed likelihoods which we drove for different points in the parameter space by assuming a broken scale invariant form of the primordial spectrum, put an upper limits for the best possible results.

For our smoothing purpose, we use DWT in a systematic way to separate the features of the raw recovered spectrum. We map the raw recovered spectrum which has 1400 discrete points to an array of 2^{11} points by padding at the two ends. By applying the discrete wavelet transform to the input file, we get corresponding 2^{11} wavelet coefficients. If we apply the inverse wavelet transform to whole set of derived wavelet coefficients, the orthonormality of the wavelet basis will lead back to the raw recovered spectrum. But if we exclude wavelet coefficients above a given level of resolution, then the inverse wavelet transform, leads to a smoothed power spectrum compared to raw deconvolved spectrum essentially filtering out spurious high resolution structures arising due to numerical effects [12].

At the first step, we use the original raw recovered spectrum to calculate the likelihood to the WMAP-3 data. It is in fact the inverse wavelet transform of the whole wavelet coefficients which has $2^n, n = 11$ coefficients. We call it the recovered spectrum at level 11. In the next step, we cut half of the coefficients and we use only the first 2^{10} coefficients. The derived results (recovered spectrum at level 10) would be smoother than the original spectrum. We continue the procedure for all different levels (n=2 to 11), and at each level we calculate the likelihood of the recovered results. The recovered result at a level which gives the best likelihood

[11] There are some indications that the RL method can be related to a zero-noise limit of ML estimation.

[12] It is important to note that the deconvolution is based on the binned C_l angular power spectrum, implying a finite resolution in multipole (2D wavenumber) space. Hence is clear from information theoretic/physical intuition that all structures in the (3-D) power spectrum on scales smaller than the corresponding size of the wavenumber bin are bound to be spurious.

would be our final result. Using discrete wavelet transforms has this important advantage of being a well defined smoothing procedure that also retains identify localized features in P(k) that contribute a significant improvement to the likelihood. Figure 3.13 shows the reconstructed $P(k)$ for a sample point in the cosmological parameter space, smoothed up to different wavelet levels. The inset of the likelihood as a function of smoothing resolution shows that there exists an 'optimal' level of smoothing which 'maximizes' the likelihood with respect to data. The blue line in figure 3.13 is related to the 9th wavelet level where the best likelihood to the data is achieved. We reiterate that this allow the entire procedure to be automated so that an "optimal" primordial spectrum is recovered given the cosmological parameters.

3.6.2 Primordial spectrum from WMAP 3 year data

In this section we reconstruct the primordial power spectrum optimized to get the best likelihood for six different sample points in the cosmological parameter space where each of these points has a special importance. We assume a flat ΛCDM model and the differences between these 6 cases are just in the values of the background cosmological parameters within this sub-space of parameters. In the next section we use our automated routine to perform the cosmological parameter estimation and explore a coarsely sampled but reasonable sized contiguous volume of the parameter space. In this part, we chose to compare all the reconstructed results with the best fit power law form of the primordial spectrum in the whole parameter space, referred to as "model G" (see "Reference model" in this section), rather than comparison with the result from the power law form of the spectrum for the same point in the parameter space. This highlights the effect of assuming the free form of the primordial spectrum and emphasizes on the significant improvement of the global likelihood.

Model A: Cosmological parameters from SDSS

In this case we consider a flat ΛCDM cosmological model with cosmological parameters motivated by, and consistent with, the results of large scale structure observations from Sloan Digital Sky Survey (SDSS) [102]. We use $h = 0.72$ (Hubble parameter), $\Omega_{dm} = 0.246$ (dark matter density), $\Omega_b = 0.050$ (baryonic matter density), $\Omega_\Lambda = 0.704$ (Λ energy density) and $\tau = 0.06$ (optical depth). These parameters are consistent with the best fit results from SDSS with $h\Omega_m = 0.213 \pm 0.023$ and $\Omega_b/\Omega_m = 0.17$ (where $\Omega_m = \Omega_{dm} + \Omega_b$) for a flat ΛCDM cosmological model. We

Table 3.2: Different points in the parameter space and the resultant effective likelihood from the reconstructed primordial spectrum using WMAP 3 year data. The $\Delta\chi^2_{\rm eff}$ is twice the logarithm of the relative likelihood with respect to the best result in the whole parameter space by assuming power law form of the primordial spectrum.

Model	H_0	Ω_{dm}	Ω_b	Ω_Λ	τ	$\Delta\chi^2_{\rm eff}$
Model A (compatible with SDSS)	72.0	0.246	0.050	0.704	0.06	-18.76
Model B (compatible with 2df)	63.0	0.251	0.041	0.708	0.06	-4.38
Model C (compatible with BAO)	68.0	0.229	0.052	0.719	0.06	-2.93
Model D (compatible with SN Ia + BAO)	72.0	0.229	0.046	0.725	0.06	-14.52
Model E (compare to WMAP1)	71.0	0.226	0.044	0.730	0.0	-13.40
Model F (compatible with flat CDM)	50.0	0.904	0.096	0.0	0.06	-26.70

have chosen $\tau = 0.06$ throughout this section, as it is one of the most reliable values for the optical depth at the present from observations of Lyman-α forest [176, 177]. We reconstruct the primordial power spectrum for this point in the parameter space. The reconstructed result for $P(k)$ and the resultant C_l^{TT} and C_l^{TE} are shown in figure 3.14 (Model A). The resultant C_l (including TT and TE polarization spectra) for this point in the parameter space given by the reconstructed primordial power spectrum, can improve the effective likelihood by $\Delta\chi^2_{\rm eff} = -18.67$ with respect to the reference likelihood of model G.

Model B: Cosmological parameters from 2DF Galaxy Redshift Survey

In this case we choose parameters consistent with the results from 2df galaxy redshift survey [103]. We use $h = 0.63$, $\Omega_{dm} = 0.251$, $\Omega_b = 0.041$, $\Omega_\Lambda = 0.708$ and $\tau = 0.06$. These parameters are consistent with the results from 2df with $h\Omega_m = 0.168 \pm 0.016$ and $\Omega_b/\Omega_m = 0.185 \pm 0.046$ for a flat ΛCDM cosmological model. However here we have used a marginally bigger value of matter density and marginally lower value of Hubble parameter in compare with the best fit result from 2df, but still these parameters are consistent with the 2df constraints within 1σ. The reconstructed result for $P(k)$ and the resultant C_l^{TT} and C_l^{TE} are shown in figure 3.14 (Model B). The resultant C_l for this point in the parameter space, can improve the effective likelihood by $\Delta\chi^2_{\rm eff} = -4.38$ with respect to the reference likelihood of model G.

Model C: Cosmological parameters from the results of detection of baryon acoustic peak oscillations

In this case we consider a flat ΛCDM cosmological model with cosmological parameters consistent with the results of measurements of the baryon acoustic oscillations(BAO) [96]. We use $h = 0.68$, $\Omega_{dm} = 0.229$, $\Omega_b = 0.052$, $\Omega_\Lambda = 0.719$ and $\tau = 0.06$. These parameters are consistent with the best fit results from BAO with $\Omega_m h^2 = 0.130 \pm 0.011$ and $\Omega_b h^2 = 0.024$ for a flat ΛCDM cosmological model. The reconstructed result for $P(k)$ and the resultant C_l^{TT} and C_l^{TE} are shown in figure 3.14 (Model C). The resultant C_l for this point in the parameter space given by the reconstructed primordial power spectrum, can improve the effective likelihood by $\Delta\chi^2_{\rm eff} = -2.93$ with respect to the reference likelihood of model G.

Model D: Cosmological parameters from observational constraints on the matter density using SN Ia and BAO data

Model independent estimation of the matter density by using supernovae [46, 47] and BAO [96] data by [115] is used in this section to set the cosmological parameters. The total matter density, independent of the model of dark energy is found to be $\Omega_m = 0.276 \pm 0.023$. This value is, in fact, the total sum of dark matter density and baryonic matter density. We can also choose the value of baryon density in a way to be consistent with the prediction of big bang nucleosynthesis where $\Omega_b h^2 \approx 0.02$ [178,179]. We use $h = 0.72$, $\Omega_{dm} = 0.229$, $\Omega_b = 0.046$, $\Omega_\Lambda = 0.725$ and $\tau = 0.06$. These parameters are consistent with the two constraints mentioned above. The resultant C_l for this point in the parameter space driven by the reconstructed primordial power spectrum, can improve the effective likelihood by $\Delta\chi^2_{\rm eff} = -14.52$ with respect to the reference likelihood of model G. The reconstructed result for $P(k)$ and the resultant C_l^{TT} and C_l^{TE} are shown in figure 3.14 (Model D).

Model E: Cosmological parameters from comparison with the results from WMAP 1 data

In this case we use the same parameters as we used before in section 3.3), where we introduced the improved Richardson-Lucy method and analyzed the WMAP 1 data. This is for comparison between our results from WMAP 1 and WMAP 3 years data. As in the section 3.3, here also we use $h = 0.71$, $\Omega_{dm} = 0.226$, $\Omega_{bm} = 0.044$, $\Omega_\Lambda = 0.730$ and $\tau = 0.0$ for the parameters of our background cosmology. The reconstructed primordial power spectrum for this point in the parameter space, can improve the effective likelihood by $\Delta\chi^2_{\rm eff} = -13.40$ with respect to the reference likelihood of model G. This result is consistent with the result by using WMAP 1 data and there is no significant difference in features of the reconstructed results. The reconstructed result for $P(k)$ and the resultant C_l^{TT} and C_l^{TE} are shown in figure 3.14 (Model E).

Model F: Cosmological parameters from Standard Cold Dark Matter (SCDM) model

In this case we assume a Cold Dark Matter universe (CDM) where the energy density of the dark energy is assumed to be zero. For $h = 0.50$, $\Omega_{dm} = 0.904$, $\Omega_b = 0.096$, $\Omega_\Lambda = 0.0$ and $\tau = 0.06$, we could improve the effective likelihood by $\Delta\chi^2_{\rm eff} = -26.70$ which shows that by assuming a free form of the primordial

spectrum, the standard CDM model of a flat universe can be very well fitted to the CMB data alone. Studies by [181] have shown that a CHDM model of the universe (which there is also no dark energy) also can have a good fit to the WMAP 3 years data. It is very interesting that for this point in the parameter space we could get a big improvement in the effective likelihood. We should note here that for this point in the parameter space, we have set $\Omega_b h^2 = 0.024$ which is in agreement with big bang nucleosynthesis however this point in the parameter space is not well fitted with other cosmological observations, like large scale structure observations or the supernovae data. Results are shown in figure 3.14 (Model F).

Model G (Reference model): cosmological parameters from best fit power law to the WMAP 3 year data

Interestingly, for this point in the parameter space, we could not significantly improve the effective likelihood by considering the free form of the primordial spectrum where we used $h = 0.732$, $\Omega_{dm} = 0.1967$, $\Omega_b = 0.0416$, $\Omega_\Lambda = 0.7617$ and $\tau = 0.089$. In fact adding features to the form of primordial spectrum for this point in the parameter space could not improve the resultant effective likelihood. We interpret this to arise from the fact the cosmological parameters themselves adjust with a large number of degrees of freedom to the fit comparable to the freedom in the primordial power spectrum (encoded in a finite number of wavelet coefficients). In short, all the cosmological parameters have been chosen in way to give us the best likelihood by strong assumption of power law form of the primordial spectrum. **In this section (and also in the next section), the resultant $\chi^2_{\rm eff}$ of different models are compared with this model as the reference model.**

Different assumed models with their parameters and their resultant likelihoods are shown in table 3.2.

3.7 Toward cosmological parameter estimation

It is very important to note that despite of allowing a free form for the primordial spectrum, not all cosmological models (i.e., all points in the parameter space) can be fitted to the data equally well. We clearly show that some points in the cosmological parameter space fit the WMAP 3 year CMB data better than the other points, by 'optimizing' the likelihood over a free form of the primordial spectrum. We conjecture that the positive definiteness of the primordial spectrum does not allow

us to fit all the points in the parameter space to the data equally well, and some points will have a better fit to the data. In this section we would like to present strong evidence that despite of allowing a free form of the spectrum, the derived likelihoods do strongly discriminate between different neighboring points in the parameter space. As an example, for a flat ΛCDM model, we fix the values of $H_0 = 72$, $\tau = 0.06$ and $\Omega_\Lambda = 0.70$ and we vary the values of Ω_b and Ω_{dm} keeping the total fixed at $\Omega_m = \Omega_b + \Omega_{dm} = 0.30$ and calculate the likelihood. We find a minimum in the value of the $\chi^2_{\rm eff}$ around $\Omega_b = 0.050$ and $\Omega_{dm} = 0.250$ which shows that the data prefers this combination among the models with $\Omega_m = 0.30$.

In parameter estimation, other cosmological observations can be used to put constraints on the parameter space. For example, some region of the parameter space may be in agreement with CMB data, but being ruled out strongly by other observations. However in our example, the best result seems to be well in agreement with all other cosmological observations, including large scale structure observations from SDSS [102], supernovae data by SNLS [47] and Gold [46], detection of baryon oscillations [96] and it is also in agreement with big bang nucleosynthesis. In figure 3.15 we see the resultant $\Delta\chi^2_{\rm eff}$ versus different values of baryonic matter (left panel-blue line) and the reconstructed $P(k)$ for the best combinations of Ω_b and Ω_{dm} assuming $\Omega_m = 0.30$ (right panel-blue line). The red curves in figure 3.15 have the same characteristic but $\Omega_\Lambda = 0.73$ and $\Omega_m = 0.27$. Clearly, 'optimizing' over the primordial power spectrum allows us to get significantly higher likelihood ($\Delta\chi^2 = -19.65$) for $\Omega_m = 0.30$ compared to $\Omega_m = 0.27$ ($\Delta\chi^2 = -11.55$).

Here we have only considered two limited 1-D slices in the cosmological parameter space, but our main aim is to do the cosmological parameter estimation for the whole volume of the parameter space. However as it has been mentioned before, doing a cosmological parameter estimation in the whole parameter space would be computationally very expensive. Recently few new methods of parameter estimation have been proposed which are claimed to be much faster than the usual methods of Monte Carlo Markov Chain or grid sampling. These new methods may be suitable for our purpose but they are still applicable for a one dimensional space and they need to be modified to be applied in our problem [182–185]. Though it is still difficult and beyond our abilities to do the cosmological parameter estimation in the whole parameter space and with a high resolution, still we can do it for a reasonably large contiguous volume of the parameter space. In this part, we present the results for the cosmological parameter estimation by fixing the value of $\tau = 0.06$ (which we have chosen throughout this section) and varying the values

of Ω_b, Ω_{dm} and h in a large volume of the parameter space. In our analysis we use the following priors: $35 < H_0 < 85$, $0.012 < \Omega_b h^2 < 0.030$, $0.04 < \frac{\Omega_b}{\Omega_{dm}} < 0.30$ and $0 < \Omega_\Lambda < 1$. Any of the given priors for Ω_b, Ω_{dm} and h has been divided by eight equally-spaced points whose combinations will generate our assumed initial sampling in the parameter space. Ω_Λ is derived from the other parameters assuming a flat universe. Our motivation to choose these wide priors are from the strong limits from other astronomical and cosmological observations. In figure 3.16 we see the resultant $-\Delta\chi^2_{\rm eff}$ (in Z axis and also in color indicated by the tool bar in the upper panel) versus different values of Hubble parameter (X axis in both upper and lower panel) and $\Omega_b h^2$ (Y axis in both upper and lower panel). The lower panel shows the relative values of the Ω_Λ in our parameter space (indicated by color in the lower panel).

The best likelihood has been derived for $\Omega_b = 0.084$, $\Omega_{dm} = 0.764$, $\Omega_\Lambda = 0.152$ and $H_0 = 50$ with $\Delta\chi^2_{\rm eff} = -29.282$ with respect to the reference likelihood of model G in section 3.6.2. Another point in the parameter space with $\Omega_b = 0.058$, $\Omega_{dm} = 0.416$, $\Omega_\Lambda = 0.526$ and $H_0 = 60$, which is more compatible with the other cosmological observations, also has a very good optimized likelihood with $\Delta\chi^2_{\rm eff} = -29.014$ with respect to the reference likelihood of model G in section 3.6.2 , which is very close to our best result.

Results also show that for a very wide range of Ω_Λ, even when its density is close to zero, we can have a very good fit to the WMAP 3 year data which is expected, as CMB data alone are not very much sensitive to the Λ density.

3.8 Summary and Conclusion

The CMB anisotropy is usually expected to be statistically isotropic and Gaussian [186]. In that case, the angular power spectrum of CMB anisotropy encodes all the information that may be obtained from the primary CMB anisotropy, in particular, the estimation of cosmological parameters. It is very important to note that cosmological parameters estimated from CMB anisotropy (and other similar observations of the perturbed universe) usually assume a simple parametric form of spectrum of primordial perturbations. It is clear, however, that estimation of cosmological parameters depends on the extent and nature of parameterization of the primordial (initial) perturbations included into the parameter space considered [145].

We proceed on a complimentary path of determining the primordial power

spectrum directly from the CMB anisotropy for a set of cosmological parameters. Assuming cosmological parameters, our method applied to the angular power spectrum measured by WMAP yields interesting deviations from scale invariance in the recovered primordial power spectrum. The recovered spectrum shows an infrared cut-off that is robust to small changes in the assumed cosmological parameters. The recovered spectrum points to the form of infra-red cut off that matches the low multipoles of WMAP. We also show that the such forms of infra-red cut-off can arise from simple well-known effects with inflation. It is important to recall that the angular power spectrum from the 'full' sky CMB anisotropy measurement by COBE-DMR [30] also indicated an infra-red cutoff [187]. Although we mostly emphasize the infrared cutoff, the final recovered spectrum shows a damped oscillatory feature after the infra-red break ('ringing'). It has been pointed out that such oscillations improve $\chi^2_{\rm eff}$ and could be possibly a signature of trans-Planckian effects [151, 188]. We have not assessed the significance and robustness of the features at large k/k_h that may be consistent with features deduced in the analysis of recent redshift surveys [189] [13].

In this work, we have used only the angular power spectrum of WMAP measured temperature fluctuations (TT). Once the E-polarization power spectrum (EE) is announced by any CMB polarization survey, our method can be extended to include TE and EE angular power spectra in obtaining the primordial power spectrum. For instance, the very recent "QUAD" data [202] can be used for this purpose. It is also possible extend our recovery of the primordial spectrum to larger wavenumbers by using the matter density power spectrum measured by large scale redshift surveys such as the Sloan Digital sky survey SDSS and 2degree Field survey, measurement from Ly-α absorption, and possibly, weak gravitational lensing in the near future [200, 201].

In this chapter we also present a detailed analysis of the recovered primordial power spectrum. The recovered spectrum has a likelihood far better than a simple scale invariant or a scale free spectra. In [153], similar features for the primordial spectrum have been detected by using a completely different method and the significance of the features have also been evaluated. We use Discrete Wavelet Transform

[13] Our analysis here is limited to flat models cosmological models. We have also ignored the contribution from tensor perturbations and assumed adiabatic perturbations in this theis. Although, inflation generically predicts a geometrically flat universe, the power spectrum of perturbations in non-flat universe models has been studied [190–193]. The effect of tensor perturbations on the CMB anisotropy spectrum is well studied [194–197] and so is the role of isocurvature perturbations [198,199]. Hence, it is straightforward to remove these limitations in a more comprehensive future analysis.

to decompose the features of the spectrum to quantify and understand their role in improving the likelihood. In addition to the infra-red cut-off around the horizon, which was proposed by many groups to explain the lack of power in very low multipoles of the observed angular power spectrum, we show that the features around the horizon are playing a crucial role in improving the likelihood. In fact, the effect of these features on improving the likelihood, are very significant (figure 3.11). We find that these strong features are localized around the horizon.

In the last part of this chapter, we present the reconstruction of an 'optimal' primordial power spectrum for flat ΛCDM cosmological models for different sample points in the parameter space by using WMAP 3 year data. We have chosen these sample of points to be consistent with different independent cosmological observations, or consistent with special theoretical models. Almost in all cases the recovered spectra improves the resultant effective likelihood significantly in comparison with the best fit power law form of the primordial spectrum in the whole parameter space. We also generalized our study to a much bigger sample of points where we performed the cosmological parameter estimation in a large volume of the parameter space.

There are some important conclusions that can be drawn from our results. Though the published results from WMAP team after release of WMAP 3 year data suggests the lower value of matter density in comparison with the other cosmological observations like large scale structure observations from SDSS, supernovae and detection of baryon acoustic peak oscillations, our analysis shows that by assuming a free form of the primordial spectrum, CMB data can be well fitted to the models with the higher value of matter density compatible with the other cosmological observations. Our preliminary studies in the parameter space, show some evidence that by assuming the free form of the primordial spectrum models with higher value of matter density are better fitted to the WMAP 3 year data than models with low value of matter density. Another important result is that a standard CDM (Cold Dark Matter) model of the universe, can also be very well fitted to the WMAP 3 year data by assuming the free form of the primordial spectrum. In fact for a SCDM model, we could get one of our best recovered results by improving the likelihood around $\Delta\chi^2_{\rm eff} = -27$ with respect to the best result for the power law form of the spectrum in the whole parameter space(reference likelihood of model G in section 3.6.2). The features of the recovered results for all these points in the parameter space have something in common. They all show a sharp cut of around the horizon and some significant features after the horizon scale. We have seen that

the effect of these features around the horizon are very important in improving the likelihood.

Assuming a free form of the primordial spectrum, we derived the best likelihood for a ΛCDM model at $\Omega_b = 0.084$, $\Omega_{dm} = 0.764$, $\Omega_\Lambda = 0.152$ and $H_0 = 50$ within the explored region with $\Delta\chi^2_{\text{eff}} = -29.282$ with respect to the reference likelihood of model G in section 3.6.2. Another point in the parameter space with $\Omega_b = 0.058$, $\Omega_{dm} = 0.416$, $\Omega_\Lambda = 0.526$ and $H_0 = 60$, which is more compatible with the other cosmological observations, also has a very good optimized likelihood with $\Delta\chi^2_{\text{eff}} = -29.014$ with respect to the reference likelihood of model G.

The differences between our results in parameter estimation and the results from WMAP team assuming a power law form of the primordial spectrum motivates us to work towards precise cosmological parameter estimation allowing full freedom to the form of the primordial spectrum, with a higher resolution in the spacing of the parameters and also considering the whole parameter space.

In this work, we use the modestly determined quality of CMB polarization spectra from WMAP (TE and EE) simply as a consistency check. However, CMB polarization (EE) spectra from Planck Surveyor is expected to be good enough to allow us to extend our deconvolution method simultaneously to CMB temperature and polarization.

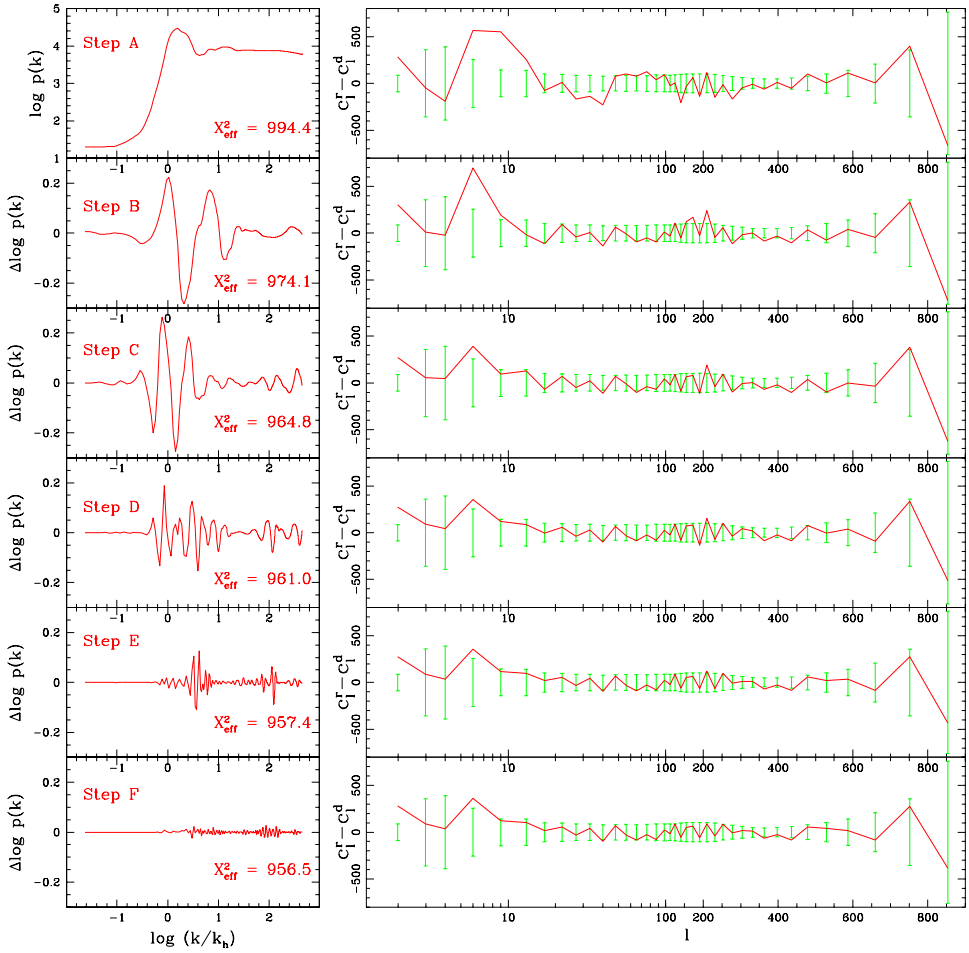

Figure 3.10: The left panels show the DWT decomposition of the features of the primordial power spectrum. Step A shows the reconstructed primordial power spectrum using the 10th level low-pass coefficients. Steps B, C, D, E and F show the localized variations due to the wavelet coefficients at the 10th, 9th, 8th, 7th and the 6th levels respectively. These variations in the primordial power spectrum are most prominent close to the horizon scale and are significant only in the first few panels, corresponding to 'low frequency' variations. The panels on the right compare the resultant angular power spectrum, C_l^r with the binned WMAP-1 angular power spectrum data. Going down from the top we progressively add features from different levels of wavelet coefficients (left) to the primordial power spectrum and show the difference, $C_l^r - C_l^d$ and error bars for C_l^d (right).

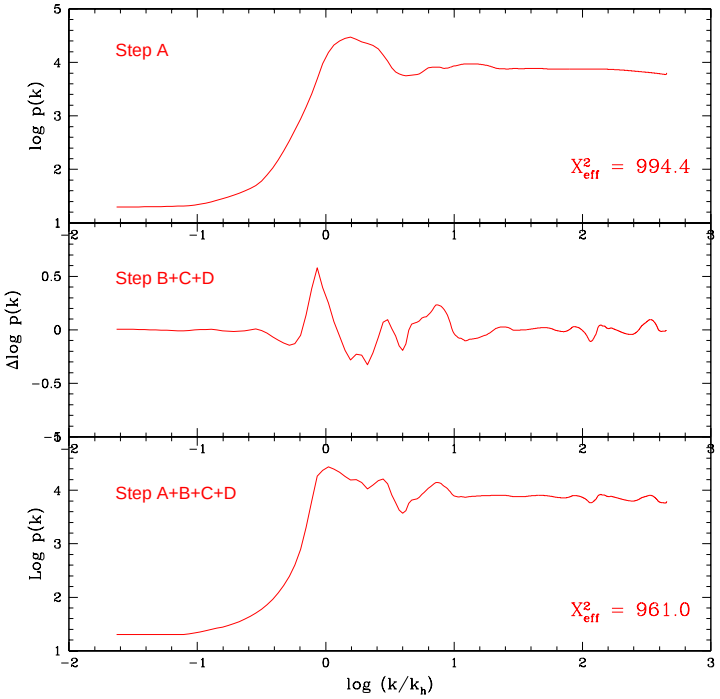

Figure 3.11: The primordial power spectrum reconstructed with the low-pass coefficients is shown in the top panel. Addition of features of steps *B*, *C* and *D* is shown in the middle panel. The combination of both these panels is shown in the bottom panel. Note the significant effect of the features on the likelihood. Results are based on WMAP 1 year data.

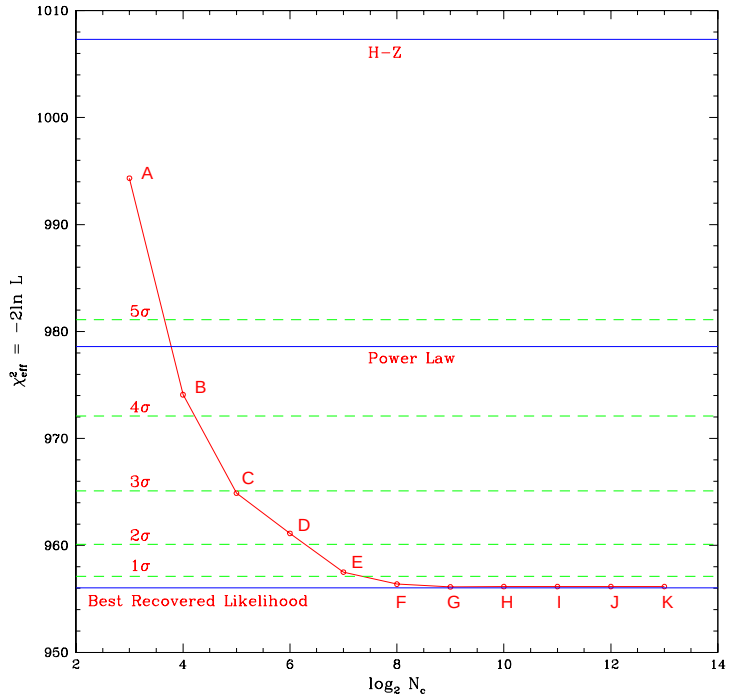

Figure 3.12: The likelihood values improve as detailed features are added to the primordial power spectrum reconstructed with low-pass coefficients. A corresponds to the primordial power spectrum reconstructed with low-pass coefficients only. $B - K$ correspond to the primordial power spectrum with the contribution of wavelet coefficients of levels 10-1 progressively added to the coarse spectrum A. There is no significant improvement in the likelihood beyond level 6 (step F). Green-dashed lines mark the Gaussian equivalent σ-levels of the likelihood relative to the best recovered spectrum. Results are compared with the best likelihood given by Power Law and Harrison-Zeldovich spectrum. N_c is the number of coefficients (low-pass and high-pass) used to define the primordial spectrum at each step. Results are based on WMAP 1 year data.

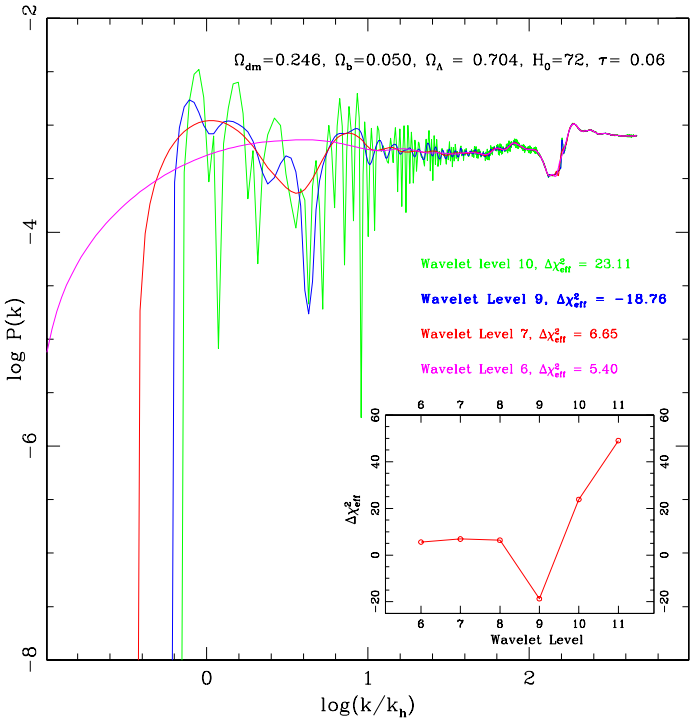

Figure 3.13: Resultant $P(k)$ for a sample point in the cosmological parameter space is shown in the blue curve. The other curves show the P(k) recovered at different levels of DWT smoothing. The blue line which is the reconstructed result obtained by retaining all wavelet coefficients up to the 9th wavelet level has the best likelihood with $\Delta\chi^2_{\rm eff} = -18.76$ with respect to the best fit power-law primordial spectrum in the whole parameter space. We used $H_0 = 72, \Omega_{dm} = 0.246, \Omega_b = 0.05, \Omega_\Lambda = 0.704, \tau = 0.06$ as the cosmological parameters. The plot in the inset shows the resultant $\Delta\chi^2_{\rm eff}$ of the reconstructed results at different wavelet levels. The 'optimality' of the $n = 9$ level DWT smoothing in this case is clearly demonstrated. Here we have used WMAP 3 year data.

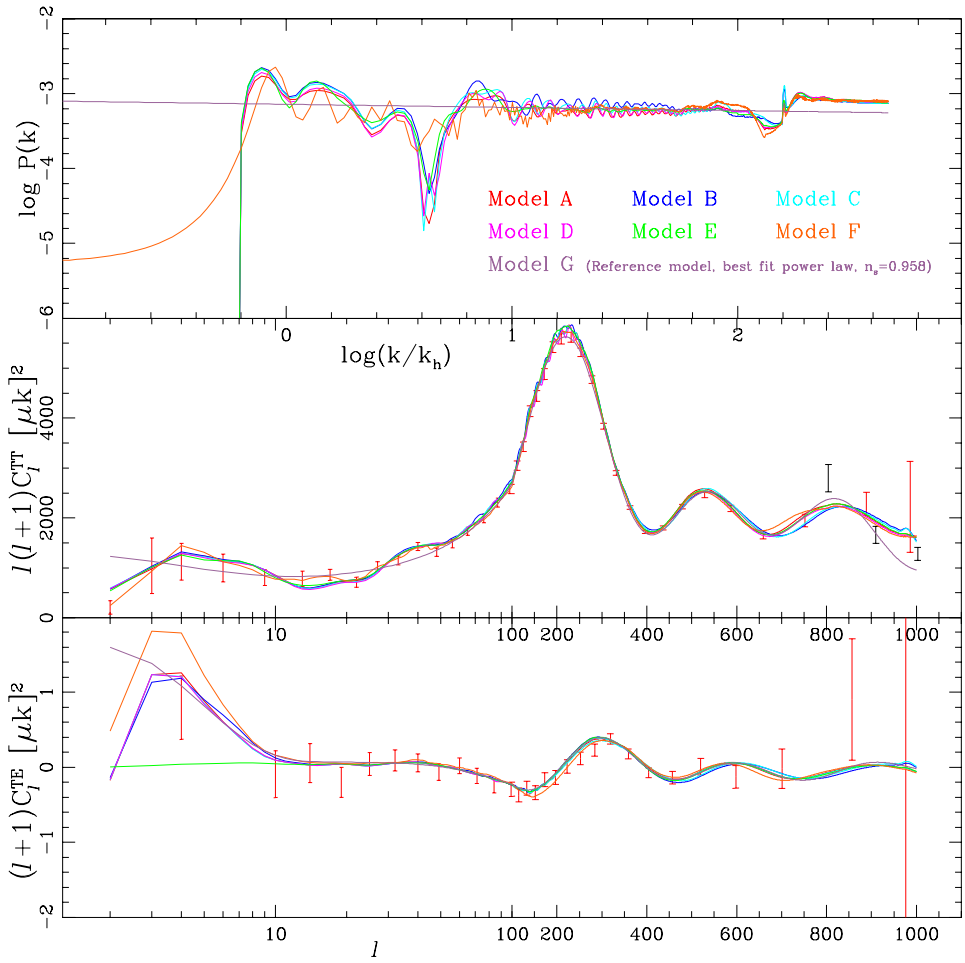

Figure 3.14: Reconstructed primordial spectrum (top panel) and the resultant C_l^{TT} (middle panel) and C_l^{TE} (lower panel) angular power spectra are plotted for 6 different points in the parameter space assuming a flat ΛCDM cosmological model. Cosmological parameters of *Model A*: $H_0 = 72, \Omega_{dm} = 0.246, \Omega_b = 0.05, \Omega_\Lambda = 0.704, \tau = 0.06$ and the recovered results for this model gives $\Delta\chi^2_{\rm eff} = -18.76$. Cosmological parameters of *Model B*: $H_0 = 63, \Omega_{dm} = 0.251, \Omega_b = 0.041, \Omega_\Lambda = 0.708, \tau = 0.06$ and the recovered results for this model gives $\Delta\chi^2_{\rm eff} = -4.38$. Cosmological parameters of *Model C*: $H_0 = 68, \Omega_{dm} = 0.229, \Omega_b = 0.052, \Omega_\Lambda = 0.719, \tau = 0.06$ and the recovered results for this model gives $\Delta\chi^2_{\rm eff} = -2.93$. Cosmological parameters of *Model D*: $H_0 = 72, \Omega_{dm} = 0.229, \Omega_b = 0.046, \Omega_\Lambda = 0.725, \tau = 0.06$ and the recovered results for this model gives $\Delta\chi^2_{\rm eff} = -14.52$. Cosmological parameters of *Model E*: $H_0 = 71, \Omega_{dm} = 0.226, \Omega_b = 0.044, \Omega_\Lambda = 0.730, \tau = 0.0$ and the recovered results for this model gives $\Delta\chi^2_{\rm eff} = -13.40$. Cosmological parameters of *Model F*: $H_0 = 50, \Omega_{dm} = 0.904, \Omega_b = 0.096, \Omega_\Lambda = 0.0, \tau = 0.06$ and the recovered results for this model gives $\Delta\chi^2_{\rm eff} = -26.70$. *Model G* **is the** *reference model* **against which all calculated** $\Delta\chi^2_{\rm eff}$**s are with respect to this model. This represents the best fit power law primordial spectrum in the whole parameter space.** The red error-bars in the middle and lower panels represents the binned angular power spectrum from WMAP 3 year data. The black error-bars at the middle panel at the high l, are from ACBAR experiment [175]. The excess of power and the bump in the recovered $P(k)$ at the high k ($logk/k_h \approx$), seems to be related to the higher measurements of the angular power spectrum at high l's in WMAP 3 year data in comparison with the other experiments such as ACBAR.

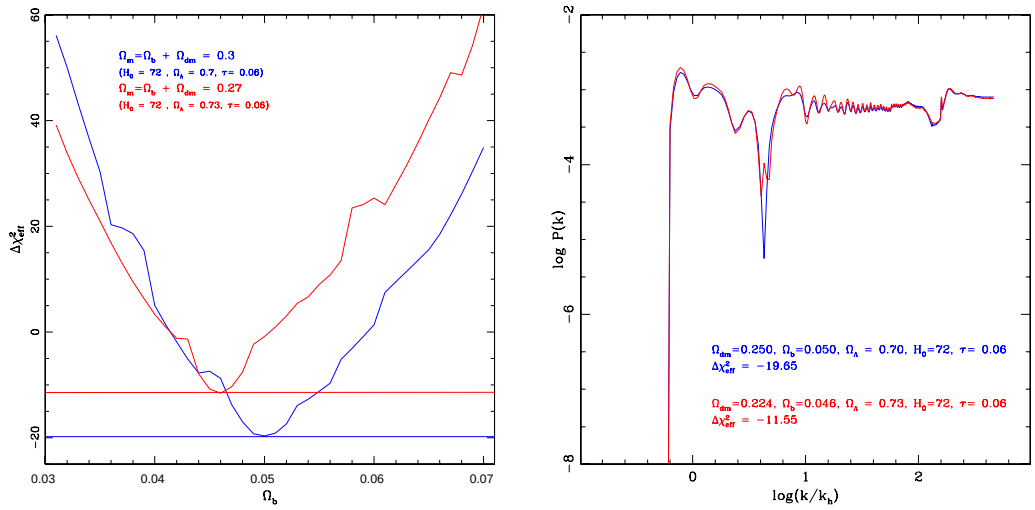

Figure 3.15: A 1-D slice (Ω_m = *constant*) through the cosmological parameter space demonstrates that the data retains strong discriminatory power in the cosmological parameter space even when there is full freedom in choosing the primordial power spectrum. **Left panel:** Plot of $\Delta\chi^2_{\rm eff}$ of the reconstructed results with respect to the reference likelihood of model G in section 3.6.2 by assuming free form of the primordial spectrum, for a flat ΛCDM model with $h_0 = 0.72$, $\tau = 0.06$ and $\Omega_\Lambda = 0.70$ and $\Omega_m = \Omega_b + \Omega_{dm} = 0.30$ for different values of Ω_b (blue line). The red curve is for similar models except for $\Omega_m = \Omega_b + \Omega_{dm} = 0.27$. Clearly, 'optimizing' over the primordial power spectrum allows us to get significantly higher likelihood ($\Delta\chi^2 = -19.65$) for $\Omega_m = 0.30$ compared to $\Omega_m = 0.27$ ($\Delta\chi^2 = -11.55$). This demonstrates that even though we allow a free form of the primordial spectrum, the data does show very strong preference for particular values of cosmological parameters. **Right panel:** Reconstructed primordial spectrum, $P(k)$, for a flat ΛCDM model with $\Omega_b = 0.050, \Omega_{dm} = 0.25, h_0 = 0.72, \tau = 0.06$(blue line). For these parameters of Ω_b and Ω_{dm}, we could get the best likelihood for $\Omega_m = 0.30$. The red line is the reconstructed $P(k)$ for a flat ΛCDM model with $\Omega_b = 0.0460, \Omega_{dm} = 0.224, h_0 = 0.72, \tau = 0.06$. For these parameters of Ω_b and Ω_{dm}, we could get the best likelihood for the $\Omega_m = 0.27$. It is clear that the reconstructed $P(k)$ for these two points in the cosmological parameter space are very similar. However the resultant $\Delta\chi^2_{\rm eff}$ for these two points in the parameter space shows a big difference. Here we have used WMAP 3 year data.

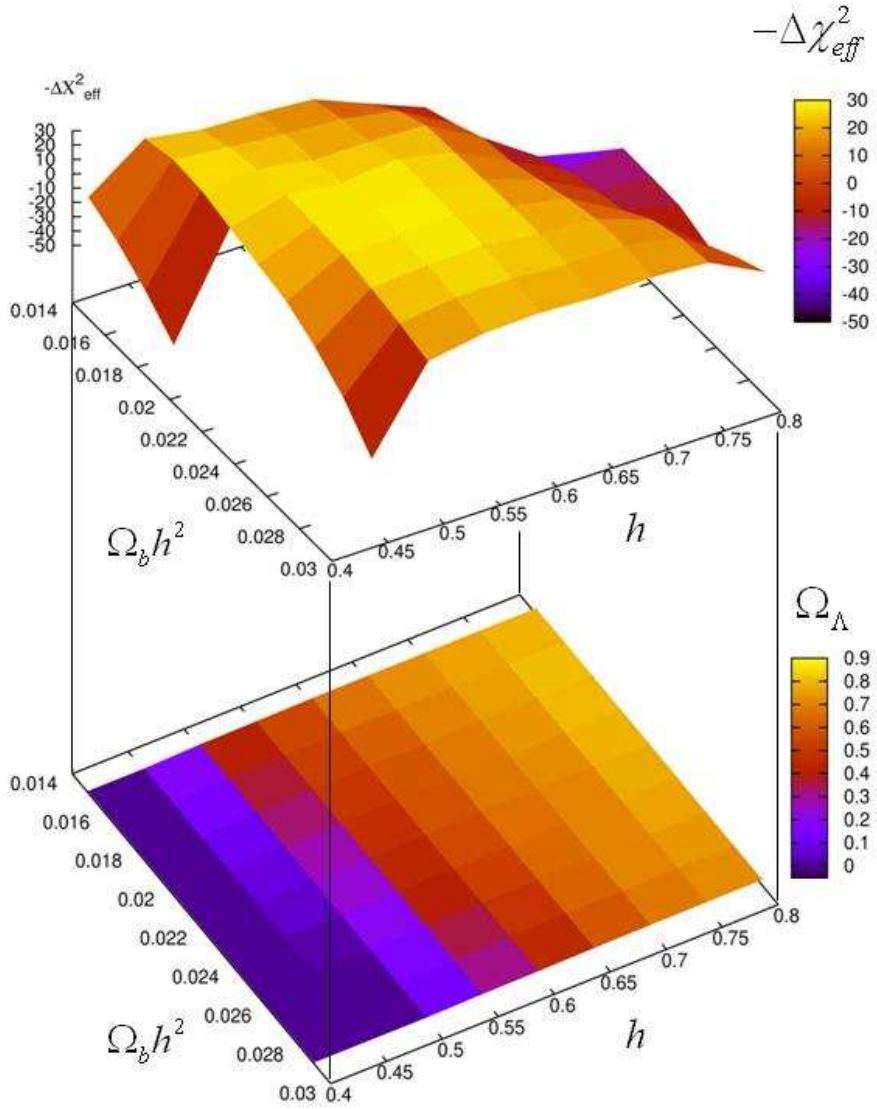

Figure 3.16: A coarse resolution and limited volume exploration of the cosmological parameter space demonstrates that the data retains strong discriminatory power in the cosmological parameter space even when there is full freedom in choosing the primordial power spectrum. The resultant $-\Delta\chi^2_{\rm eff}$ is shown (in Z axis and also in color indicated by the tool bar in the upper panel) versus different values of Hubble parameter (X axis in both upper and lower panel) and $\Omega_b h^2$ (Y axis in both upper and lower panel). The lower panel shows the relative values of the Ω_Λ in our parameter space (indicated by color in the lower panel). We have assumed here $\tau = 0.06$. Here we have used WMAP 3 year data.

Chapter 4

Conclusions

The work related to my PhD thesis has been on implementing and applying different non-parametric and model-independent statistical methods to the reconstruction of important cosmological quantities and parameters. These methods have been applied to the most recent cosmological data sets such as the WMAP data on cosmic microwave background anisotropy, the GOLD, SNLS and Union supernovae data, etc.

My research has been primarily focused on applying these advanced statistical methods (the improved Richardson–Lucy deconvolution method, wavelet analysis, smoothing methods) to two very important areas in cosmology. The main issues which I have addressed are :

* *Non-parametric recovery of the shape of the primordial power spectrum directly from observations.*

* *Non-parametric reconstruction of the expansion history of the universe and of the properties of dark energy.*

These model-independent techniques can be used to examine different cosmological models against observations, without biasing the results through any initial model assumption. In what follows, I briefly summarize the specific cosmological problems which I have studied and the methods that have been employed.

⋆ **Primordial power spectrum from CMB data:**

Precision measurements of anisotropies in the cosmic microwave background, and also of the clustering of large-scale structures, suggest that the primordial density perturbation is dominantly adiabatic and has a spectrum that is nearly scale-invariant. This is in good agreement with the simplest inflationary scenarios which predict power-law or scale-invariant forms of the primordial perturbation spectrum. However, despite the strong theoretical appeal and simplicity of a featureless primordial spectrum, it is important to determine its shape directly from observations with minimal theoretical bias. This is especially so in view of some inconsistencies that appear to have been noticed between the data and the quasi-scale-invariant form of the primordial spectrum. One such inconsistency is the observed lack of power in the low-l multipoles of the CMB angular power spectrum determined by WMAP (and also by COBE).

In my work, I have tried to reconstruct the shape of the primordial power spectrum, independently of any assumption about the model of inflation. The next logical step was to analyze the recovered features and study their effects on the resultant angular power spectrum, to match it with the observed data for consistency. And the final step was to do with parameter estimation by optimizing over the unknown primordial spectrum.

Very precise measurements of the angular power spectrum over a wide range of multipoles obtained by WMAP have opened up the possibility to deconvolve the primordial power spectrum for a given set of cosmological parameters. In studying this particular problem, I have implemented a method using a Richardson–Lucy algorithm (improved to suit my research objectives), to deconvolve the primordial power spectrum from the angular power spectrum of CMB anisotropy, as measured by WMAP. After this method was applied to the WMAP first-year data, the most prominent feature of the recovered primordial power spectrum was found to be a sharp, non-monotonic, infra-red cut-off on the horizon scale. This proved to be a much better fit to WMAP data than the most naive of monotonic infra-red cut-offs, which has been widely discussed in the post-WMAP-1 literature. Non-monotonicity in the cut-off accommodates a localized and compensating excess power below the cut-off. Most interestingly, similar features for the shape of the primordial spectrum (including the cut-off and the excess power below the cut-off) have

been obtained by other researchers using a completely different method, after our results were published. This confirms the robustness of our method.

The significance of the features in the recovered primordial power spectrum has been quantified by using Discrete Wavelet Transforms. We have found that, in addition to the infra-red cut-off around the horizon, which was proposed by many groups to explain the lack of power in very low multipoles of the observed angular power spectrum, the *features around the horizon play a crucial role* in improving the likelihood of the resultant angular power spectrum.

After release of the new set of data from WMAP mission, have applied the modified Richardson–Lucy method to the WMAP three-year data. We have improved the earlier method, notably in employing wavelet decomposition for identifying and retaining significant features. The primordial power spectrum has been reconstructed for different sets of cosmological parameters. The recovered spectrum for most of the points in the cosmological parameter space has a likelihood far better than a "best fit" power law spectrum up to $\Delta\chi^2_{eff} \approx -27$. We use Discrete Wavelet Transform (DWT) for smoothing the raw recovered spectrum from the binned data. The results obtained here reconfirm and sharpen the conclusion drawn from our previous analysis of the WMAP 1st year data. A sharp cut-off around the horizon scale and a bump after the horizon scale seem to be a common feature for all of these reconstructed primordial spectra. We have shown that although the WMAP 3 year data prefer a lower value of matter density for a power-law form of the primordial spectrum, for a free form of the spectrum we can get a very good likelihood to the data for higher values of matter density. We have even shown that a flat CDM model, with a free form of the primordial spectrum, can give a very good likelihood fit to the data. Theoretical interpretation of these results are left open to the cosmology community.

The final objective of this aspect of the project was to make an estimation of the cosmological parameters by *optimizing* over the unknown primordial spectrum. In this case, the likelihood is to be assigned to a point in the cosmological-parameter space by first obtaining the primordial spectrum that *maximizes* the likelihood. Our preliminary studies in the parameter space, show some evidence that by assuming the free form of the primordial spectrum models with higher value of matter density are better fitted to the WMAP

3 year data than models with low value of matter density. The features of the recovered results for all these points in the parameter space have something in common. They all show a sharp cut off around the horizon and some significant features after the horizon scale. Assuming a free form of the primordial spectrum, we derived the best likelihood for a ΛCDM model at $\Omega_b = 0.084$, $\Omega_{dm} = 0.764$, $\Omega_\Lambda = 0.152$ and $H_0 = 50$ within the explored region with $\Delta\chi^2_{\rm eff} = -29.282$ with respect to the best fit power law spectrum. Another point in the parameter space with $\Omega_b = 0.058$, $\Omega_{dm} = 0.416$, $\Omega_\Lambda = 0.526$ and $H_0 = 60$, which is more compatible with the other cosmological observations, also has a very good optimized likelihood with $\Delta\chi^2_{\rm eff} = -29.014$ with respect to the best fit power law spectrum.

The differences between our results in parameter estimation and the results from the WMAP team (who assume a power law form of the primordial spectrum) motivates us to work towards precise cosmological parameter estimation allowing full freedom to the form of the primordial spectrum, with a higher resolution in the spacing of the parameters and also considering the whole parameter space.

⋆ **Non-parametric reconstruction of the properties of dark energy:**

The nature of dark energy has been a subject of much debate over the past decade. Supernovae data, which gave the first indication of the accelerated expansion of the universe, are expected to elucidate this interesting question further, as the quality of the data steadily improves. Different parameterizations that have been used for the luminosity distance d_L, Hubble parameter $H(z)$, and the dark-energy equation of state $w(z)$, in modeling the properties of dark energy, are known to lead to different results for the same set of data. I have contributed to this effort by proposing a non-parametric method of smoothing the supernova data over redshift, using a Gaussian kernel, in order to reconstruct important cosmological quantities, which include $H(z)$ and $w(z)$, in a **model-independent** manner. In this approach, the data are dealt with directly, without having to rely on a parametric functional form for fitting any of the quantities $d_L(z)$, $H(z)$ or $w(z)$. The result obtained by using this approach is, therefore, expected to be model-independent. This method is shown to be successful in discriminating between different models

of dark energy if the quality of data is commensurate with that expected from the future SuperNova Acceleration Probe (SNAP). By using this method, the Hubble parameter can be reconstructed to an accuracy of better than 2%, while the look-back time can be reconstructed to an accuracy of 0.2%.

In continuation of this work, I have improved significantly upon the method of smoothing supernovae data to reconstruct the expansion history of the universe, $h(z)$, using two latest datasets, Gold and SNLS. The reconstruction process does not employ any parameterization and is independent of any dark energy model. The reconstructed $h(z)$ is used to derive the distance factor "A" up to redshift 0.35 and the results are compared with the given value of "A" from the detection of baryon acoustic oscillation peak (BAO). We find very good agreement between supernovae observations and the results from BAO for $\Omega_{0m} \approx 0.276 \pm 0.023$. The estimated values of Ω_{0m} are completely model-independent and are only based on observational data. The derived values of Ω_{0m} are then used to reconstruct the equation of state of dark energy, $w(z)$. Using our smoothing method we can demonstrate that while SNLS data are in very good agreement with LCDM, the Gold sample slightly prefers evolving dark energy. We also show that proper estimation of the equation of state of dark energy at high redshifts would be impossible at the current status of observations.

We have also introduced three new diagnostics of dark energy, "Om", "q-probe" and "w-probe". All these three diagnostics of dark energy can be calculated from the first derivative of the data. It has been found that these quantities can be reconstructed extremely accurately using different reconstruction methods even if the value of Ω_m is not known accurately.

The Om and w-probe can be used to distinguish between ΛCDM and other models of dark energy to a high degree of accuracy and q-probe can be used to probe the acceleration of the universe at different redshifts. We have applied these diagnostics to the most recent cosmological data, Union supernovae data and WMAP 5 year CMB data and we have shown that the ΛCDM model is in good agreement with the data but so are some evolving dark energy models. I am confident that the techniques developed in this thesis will shed further light to the nature of dark energy when applied to more precise future cosmological observations.

Appendix A

Smoothing errors and bias

In this section we explore the errors on the cosmological parameters due to the smoothing scheme, as also the bias which enters the results.

A.1 Smoothing errors

The smoothing scheme used in this paper is of the form :

$$y(z)^s = y_G(z) + \sum_{i=1}^{N} [y(z_i) - y_G(z_i)] S(z_i; \Delta) / \sum_{i=1}^{N} S(z_i; \Delta) \ , \tag{A.1}$$

where the quantity $S(z_i; \Delta)$ represents the smoothing function with a scale Δ and $y_G(z)$ is the subtracted guess model. The quantity being smoothed (in this case $\ln d_L$) is represented by y, while y^s represents the smoothed result. Let the errors in the data at any redshift z_i be given by $\sigma_y(z_i)$ and the errors in the guess model be $\sigma_{y_G}(z_i)$. If we look at the second term on the right hand side of eqn (A.1), we see that the errors on this term would be approximately given by the errors on y weighted down by the smoothing scale Δ and the number of data points N. Therefore the error on the smoothed result is:

$$\sigma^2_{y_s}(z) \simeq \sigma^2_{y_G}(z) + \frac{\sigma^2_y(z) + \sigma^2_{y_G}(z)}{N\Delta} \ . \tag{A.2}$$

We now consider the errors for an iterative method. The first guess is an exact

model, ΛCDM. Therefore the error on the result of the first iteration is simply

$$\sigma^2_{y_1}(z) \simeq \frac{\sigma^2_y(z)}{N\Delta} \ . \tag{A.3}$$

The next guess model is $y_1(z)$. Therefore the error on the result is

$$\sigma^2_{y_2}(z) \simeq \left(2 + \frac{1}{N\Delta}\right)\frac{\sigma^2_y(z)}{N\Delta} \ . \tag{A.4}$$

From this we can show that the errors on the result for the M-th iteration is :

$$\sigma^2_{y_M}(z) \simeq \left[1 + \sum_{i=1}^{M-1}\left(1 + \frac{1}{N\Delta}\right)^i\right]\frac{\sigma^2_y(z)}{N\Delta} \simeq \left[M + \frac{M(M-1)}{2N\Delta}\right]\frac{\sigma^2_y(z)}{N\Delta} \ .$$

The second term on the right-hand side is small for a reasonable number of iterations, since $N \simeq 2000$ and $\Delta > 0.01$ usually. Therefore we may approximate the errors on the log luminosity distance after M iterations for the guess model as

$$\sigma^M_{\ln d_L}(z) = \sqrt{M}\sigma^0_{\ln d_L}(z) \ , \tag{A.5}$$

where $\sigma^0_{\ln d_L}(z)$ is the error for a simple smoothing scheme where the data is smoothed without using a guess model.

A.2 Smoothing Bias

In any kind of a smoothing scheme for the luminosity distance, some bias is introduced both in it and in derived quantities like $H(z)$ and $w(z)$. To illustrate the effect of this bias, we calculate it for the simplest Gaussian smoothing scheme for $\ln d_L(z)$ with the width $\Delta(z) \ll 1$:

$$\ln d_L(z)^{\rm s} = N(z)\sum_{i=1}^{M} \ln d_L(z_i)\exp\left[-\frac{(z-z_i)^2}{2\Delta^2}\right] \ ,$$

$$N(z)^{-1} = \sum_{i=1}^{M}\exp\left[-\frac{(z-z_i)^2}{2\Delta^2}\right], \tag{A.6}$$

where M is the total number of supernovae data points. The bias at each redshift ($\mathcal{B}(z) = \ln d_L(z)^{\rm s} - \ln d_L(z)$) is the difference between the smoothed $\ln d_L(z)$

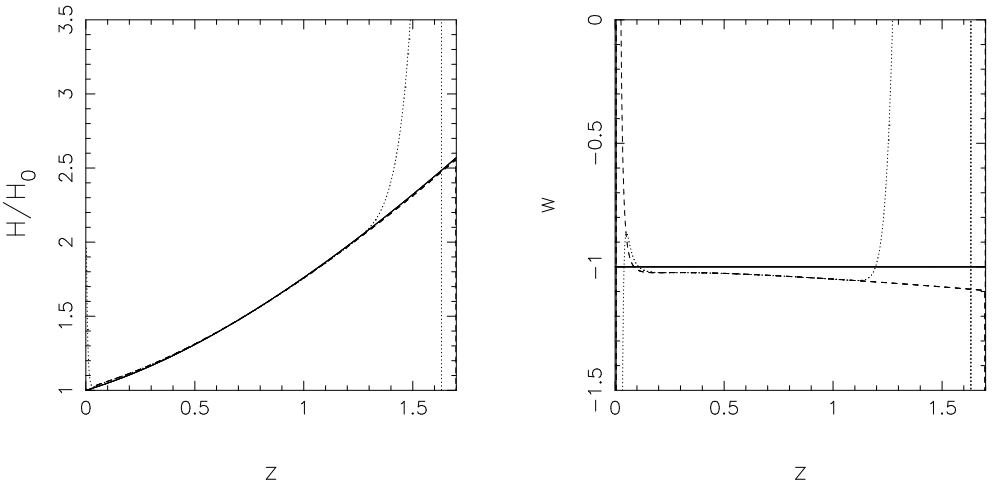

Figure A.1: Comparison of the reconstructed parameters obtained by using the smoothing method (A.6) with the variable $\Delta(z) = 0.2z/(1+z)^2$ for the ΛCDM model (the dotted line in each panel) with the analytical biased result given by eqn (A.8) (dashed line). The solid line represents the fiducial ΛCDM model. Note the excellent agreement between the analytical and numerical results in the redshift range $0.1 \leq z \leq 1.1$.

and the exact value of $\ln d_L(z)$:

$$\mathcal{B}(z) = N(z) \sum_{i=1}^{M} (\ln d_L(z_i) - \ln d_L(z)) \exp\left[-\frac{(z-z_i)^2}{2\Delta^2}\right] . \tag{A.7}$$

Expanding $\ln d_L(z_i)$ in terms of $\ln d_L(z)$ and its derivatives by Taylor expansion, we get:

$$\mathcal{B}(z) = N(z) \sum_{i=1}^{M} \left[(\ln d_L(z))'(z_i - z) + (\ln d_L(z))'' \frac{(z_i - z)^2}{2}\right] \times \exp\left[-\frac{(z-z_i)^2}{2\Delta^2}\right],$$

where the prime denotes the derivative with respect to z and we neglect higher derivatives. To see the effect of this bias at low and high redshifts where the number of supernovae on both sides of each z are not equal, we rewrite eqn (A.8) in another way. Let δ be the spacing between two neighboring data points, so that $z = m\delta$. For $m < M/2$, we have:

$$\mathcal{B}(z) = N(z)\sum_{i=1}^{2m}\left[(\ln d_L(z))''\frac{\delta^2(i-m)^2}{2}\right]\exp\left[-\frac{\delta^2(i-m)^2}{2\Delta^2}\right] + N(z)\sum_{i=2m+1}^{M}\left[(\ln d_L(z))'\delta(i-m) + (\ln d_L(z))''\frac{\delta^2(i-m)^2}{2}\right] \times \exp\left[-\frac{\delta^2(i-m)^2}{2\Delta^2}\right],$$

and for $m > M/2$:

$$\mathcal{B}(z) = N(z)\sum_{i=2m-M+1}^{M}\left[(\ln d_L(z))''\frac{\delta^2(i-m)^2}{2}\right]\exp\left[-\frac{\delta^2(i-m)^2}{2\Delta^2}\right] + N(z)\sum_{i=1}^{2m-M}\left[(\ln d_L(z))'\delta(i-m) + (\ln d_L(z))''\frac{\delta^2(i-m)^2}{2}\right] \times \exp\left[-\frac{\delta^2(i-m)^2}{2\Delta^2}\right]$$

The first term in the above equations is the general bias of the method, while the second term is the bias arising due to an asymmetric number of data points around each supernova. For $m = M/2$, the number of data points is the same from both sides and we have:

$$\mathcal{B}(z) = N(z)\sum_{i=1}^{M}\left[(\ln d_L(z))''\frac{\delta^2(i-m)^2}{2}\right]\exp\left[-\frac{\delta^2(i-m)^2}{2\Delta^2}\right].$$

In the continuous limit where $x = i - m$ is assumed, we get:

$$\mathcal{B}(z) = N(z)\int[(\ln d_L(z))''\frac{\delta^2x^2}{2}]\exp\left[-\frac{\delta^2x^2}{2\Delta^2}\right]dx\,,$$

$$N(z) = \int\exp\left[-\frac{\delta^2x^2}{2\Delta^2}\right]dx\,.$$

Therefore, the bias has the simple form

$$\mathcal{B}(z) = \frac{(\ln d_L(z))'' \delta^2}{2\delta^2/\Delta^2} = \frac{\Delta^2}{2}(\ln d_L(z))'' \ . \tag{A.8}$$

This is a good analytical approximation for the bias at redshifts in the middle range, where we do not encounter the problem of data asymmetry. To see the effect of this bias, let us assume that the real model is the standard ΛCDM, add the bias term to this model and then calculate the biased $H(z)$ and $w(z)$. The result from this analytical calculation can be compared to the result of smoothing the exact ΛCDM model using our method. The figure A.1 simply illustrates that the results obtained using Gaussian smoothing and by the use of formula eqn (A.8) are in good agreement in the middle range of redshifts. However, we do not expect the formula eqn (A.8) to work properly at very low ($z < 0.1$) and high ($z > 1$) redshifts where the above mentioned asymmetry of points adds a further bias.

Also, it appears that the smoothing bias has a tendency to decrease $w(z)$ below its actual value in the middle range of z. Thus, ΛCDM may appear to be a 'phantom' ($w < -1$) if too large a smoothing scale is chosen.

Appendix B

Exploring smoothing with variable width $\Delta(z)$

In order to deal with the problem of data asymmetry and paucity at low and high redshifts we may consider using a variable smoothing width $\Delta(z)$ in eqn (2.2). (i) Low z ($z_* \ll 1$) : in this case, there are many more supernovae at $z > z_*$ than there are at $z < z_*$. The error-bars are also small in the low redshift region. Therefore, a smaller value of Δ appears to be more appropriate at low z. (ii) High z ($z_* > 1$) : in this case, there is considerably more data at $z < z_*$ than at $z > z_*$. However, at high z the errors are considerably larger than at low z, which suggests that in order to avoid a noisy result we must use a larger value of Δ in this region. In this section, we investigate two different functional forms of $\Delta(z)$ with the above properties and show how they result in the reconstruction of the equation of state.

B.1 $\Delta(z) = \Delta_0 z/(1+z)^2$

In section 2.1.1 we mentioned that, for $|z - z_i| \ll 1$, the exponent in eqn (2.2) reduces to the form $-(z-z_i)^2/2\Delta^2(1+z)^2$ and the effective Gaussian smoothing scale becomes $\Delta(1+z)$. So if we use a variable $\Delta(z) = \Delta_0 z/(1+z)^2$ then the effective Gaussian smoothing scale approaches a constant at large z and tends to a small value at small z. The results obtained using this method are shown in figure B.1 for SNAP data, using the model $w = -0.5$. We find that, the result for the Hubble parameter does not change much. However, the equation of state is somewhat better reconstructed, but noisier at low redshift because of the small width of smoothing.

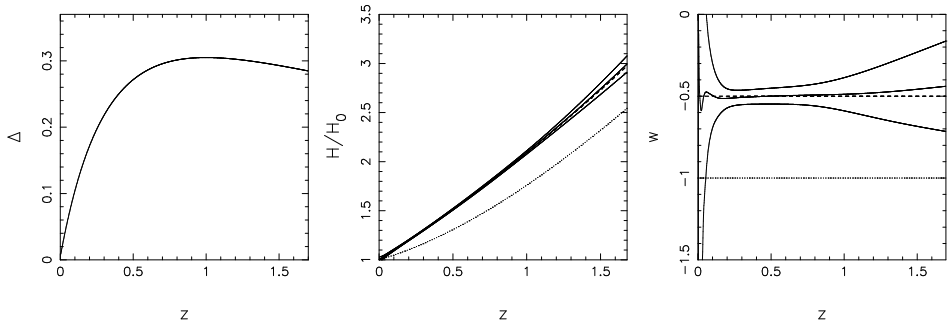

Figure B.1: The smoothing scheme of eqn (2.2) is used with $\Delta(z) = 1.2\,z/(1+z)^2$ to obtain smoothed $H(z)$ and $w(z)$ from 1000 realizations of the SNAP dataset. The panel (a) represents the form of $\Delta(z)$ used, while panels (b) and (c) represent the reconstructed $H(z)$ and $w(z)$. The dashed line in panels (b) and (c) represents the fiducial model with $w = -0.5$ while the solid lines represent the mean and 1σ limits around it. The dotted line is ΛCDM.

B.2 tan-hyperbolic form of $\Delta(z)$

Tangent hyperbolic form for $\Delta(z)$ is another form of the variable $\Delta(z)$ which can simultaneously satisfy both the low and high z requirements. It has a small value at low redshifts and a bigger value at the higher redshifts. An additional important property of this function is that it changes smoothly from low to high z, which translates into a smoother second derivative $w(z)$ – see eqn (2.2) - eqn (2.4).

A drawback of this method is that the tangent hyperbolic function introduces a number of free parameters into the problem. However the role of these parameters can be understood as follows. The tangent hyperbolic function can be written in the general form

$$\Delta(z) \;=\; a \tanh \frac{b+z}{c}\,. \tag{B.1}$$

As we saw earlier, if Δ is held constant, then optimal results are obtained for $\Delta_0 = 0.24$ in eqn (2.2) when we use bootstrap iterative process. We therefore determine a, b and c in eqn (B.1) so that $\Delta(z) \approx \frac{1}{2}\Delta_0$ at $z \approx 0$, and $\Delta(z) \approx \frac{3}{2}\Delta_0$ at $z \approx 1.7$; consequently

$$\Delta(z) \;=\; 0.36 \tanh \frac{0.23+z}{0.64}\,. \tag{B.2}$$

The results obtained using this method are shown in figure B.2 for SNAP data for the fiducial model $w = -0.5$. We find that this variable form of $\Delta(z)$ leads to a slight improvement of results at low redshifts by getting rid of the small bias which remains in the bootstrap iterative process. This improvement of the results is expected especially for the cosmological models whose equation of state at low

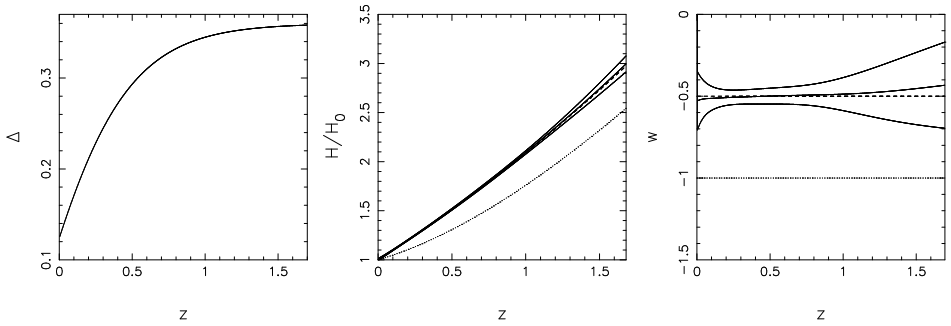

Figure B.2: The smoothing scheme of eqn (2.2) is used with a tangent hyperbolic form of variable $\Delta(z) = 0.36\tanh\frac{0.23+z}{0.64}$ to obtain smoothed $H(z)$ and $w(z)$ from 1000 realizations of the SNAP dataset. The panel (a) represents the form of $\Delta(z)$ used, while panels (b) and (c) represent the reconstructed $H(z)$ and $w(z)$. The dashed line in panels (b) and (c) represents the fiducial $w = -0.5$ model while the solid lines represent the mean and 1σ limits around it. The dotted line is ΛCDM.

redshift is very different as compared to the ΛCDM model, which is our initial guess model.

Appendix C

Examining the robustness of the smoothing method

In this section we show that the results of the smoothing method are robust against the choice of the initial guess model and also to the chosen value of smoothing width Δ.

We assumed three different cosmological models as our initial guess model and we applied our smoothing method on the Gold dataset. The final results by using these three different initial guess models are almost identical with $\Delta\chi^2 < 0.01$. We have got $\chi^2 = 157.40$ by using a flat ΛCDM model with $\Omega_{0m} = 0.30$ as the initial guess model after 89 iteration, while we have got $\chi^2 = 157.40$ for a flat ΛCDM model with $\Omega_{0m} = 0.25$ after 91 iteration, and $\chi^2 = 157.39$ for a flat quiessence model with $\Omega_{0m} = 0.30$ and $w(z) = -0.8$ after 104 iteration. In figure C.1 we can see the reconstructed $h(z)$ and $w(z)$ for the Gold data set by assuming these three different initial guess models. As we see, the robustness of the method for the choice of the initial guess model is obvious.

We have also used different values of Δ (width of smoothing in eqn (2.2), in our reconstruction process to check the reliability and stability of our results against the changes in the value of Δ. We have used three values of Δ equal to $0.30, 0.60$ and 0.90 in our smoothing method and we have applied it on the Gold dataset. By using $\Delta = 0.30$ we have got $\chi^2 = 157.38$ after 9 iteration, while we have got $\chi^2 = 157.40$ by using $\Delta = 0.60$ after 89 iteration, and $\chi^2 = 157.41$ by using $\Delta = 0.90$ after 407 iteration. In figure C.2 we can see the reconstructed $h(z)$ and $w(z)$ for the Gold dataset by using these three values of Δ. We can clearly see that the results are not sensitive to the given value of Δ. These two examinations confirm the overall

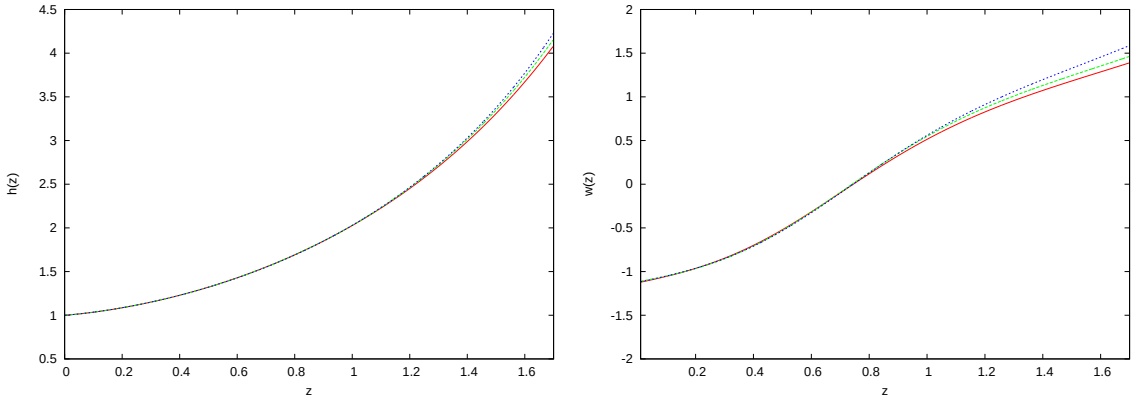

Figure C.1: Reconstructed $h(z)$ (left panel) and $w(z)$ (right panel) for the Gold dataset by assuming three different initial guess models. The red solid line is the reconstructed result by using a flat ΛCDM model with $\Omega_{0m} = 0.30$ as the initial guess model. The green dashed line is the reconstructed results by using a flat ΛCDM model with $\Omega_{0m} = 0.25$, and the blue dotted line is the reconstructed result by using a flat quiessence model with $w(z) = -0.8$ and $\Omega_{0m} = 0.30$ as the initial guess models. We can clearly see that the results are almost identical which shows the robustness of the method for the different choices of the initial guess model.

robustness of the method for different initial assumptions.

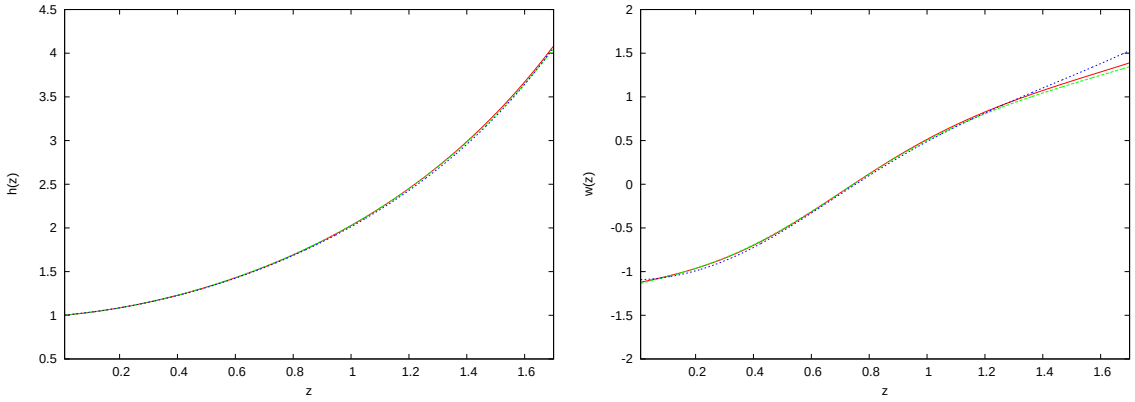

Figure C.2: Reconstructed $h(z)$ (left panel) and $w(z)$ (right panel) for the Gold dataset by using three different values of Δ (width of smoothing). The red solid line is the reconstructed result by using $\Delta = 0.60$. The green dashed line is the reconstructed results by using $\Delta = 0.90$, and the blue dotted line is the reconstructed result by using $\Delta = 0.30$. In all these cases we have stopped the boot-strapping process after reaching to the minimum χ^2. We can see that the method is robust against the variation of Δ in a wide range.

Appendix D

Some aspects of the Richardson-Lucy deconvolution method.

In this appendix, we provide support and justification for some steps in our method for recovering the primordial power spectrum. In section D.1 we demonstrate the robustness of the iterative Richardson-Lucy deconvolution to changes in the initial guess. The next section (D.2) discusses the advantage of the improved Richardson-Lucy method used in our work. In the last section (D.3), we model the broad features of reference spectrum analytically and show that it is well understood.

D.1 Effect of the initial guess in the Richardson-Lucy method

The effect of the initial guess is negligible in the Richardson-Lucy method of deconvolution for our problem. We find that the result for various different initial guesses come very close to each other after a few iterations. Here we demonstrate the robustness of our method by convolving using the C_l from a test spectrum (with a step) using different initial guesses. In figure D.1 deconvolved raw $P(k)$ arising from different forms of the initial guess spectra

$$P(k) = constant, \quad P(k) = 1/k, \quad P(k) = 1/k^2, \tag{D.1}$$

are shown. The effect of the initial guess is absent in the portion of the k space probed well by the kernel. The deconvolved spectra are almost identical for all

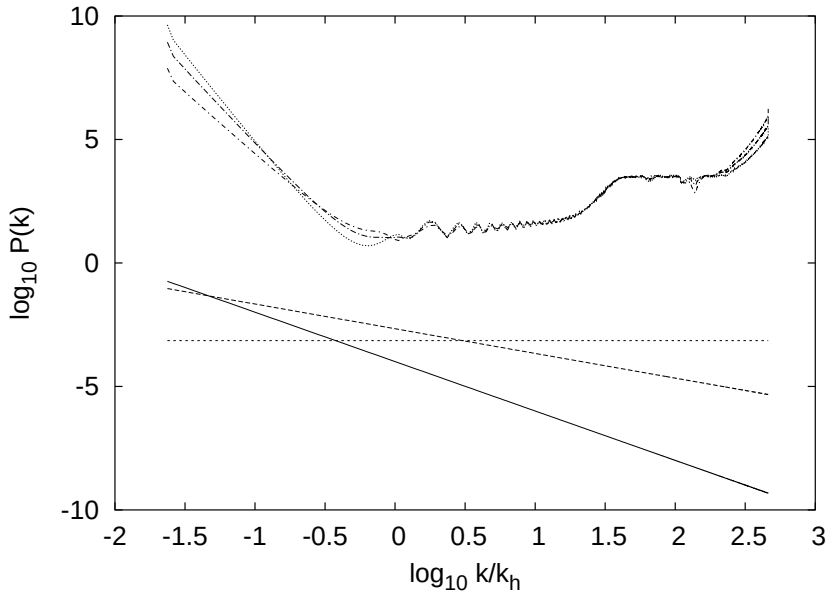

Figure D.1: The figure shows the raw power spectrum recovered using the Richardson-Lucy algorithm starting from three different initial guesses. The effect of the initial guess is negligible in the other region k space. As shown in the next section D.3, the artifacts at low k and high k which are removed by the reference spectrum have a known dependence on the initial guess.

these different initial guesses in that region of k space. As discussed in section D.3, the dependence of deconvolved spectrum at the small and large k ends is well understood and get largely removed when divided by the reference spectrum. In a previous work we have checked a large variety of initial guesses and concluded the RL method applied to our problem of recovering the primordial spectrum from the CMB anisotropy is independent of the initial guess. [146].

D.2 The Improved Richardson Lucy method

In this section we show the advantage of the improved Richardson Lucy algorithm given by eqn (3.14) over the standard method given by eqn (3.13). We compare the raw power spectrum $P^{(i)}(k)$ and the corresponding angular spectrum $C_l^{(i)}$ obtained from the WMAP binned angular power spectrum, C_l^D using RL and IRL algorithm as the iterations progress. In figure D.2, the left panel shows the χ^2 of $C_l^{(i)}$ w.r.t C_l^D. As expected, the RL method leads to a lower (better) χ^2 than the IRL method. However, we are interested in a recovering a $P(k)$ which give C_l that has better likelihood with respect to WMAP data. The right panel of figure D.2 plots the WMAP likelihood

(a)

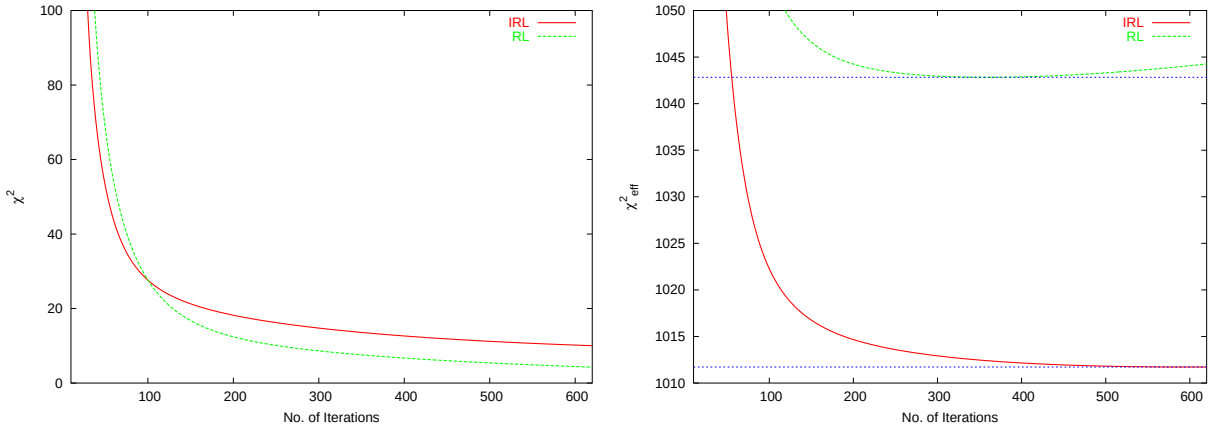

Figure D.2: The left panel plots the variation of χ^2 of $C_l^{(i)}$ obtained after ith iteration (w.r.t the binned WMAP spectrum, C_l^D) with increasing iterations for the Richardson-Lucy (RL) method and improved version (IRL) we present in this work. The panel on the right, plots the variation of $\chi^2_{\rm eff} \equiv -2\ln\mathcal{L}$ of the $C_l^{(i)}$ given by the WMAP likelihood, $\mathcal{L}$. In contrast to RL, in the IRL method $\chi^2_{\rm eff}$ converges with iteration and to a significantly lower value.

given in terms of $\chi^2_{\rm eff} = -2\ln\mathcal{L}$. This figure justifies the 'improved' label to the IRL method. For the RL case, the value of $\chi^2_{\rm eff}$ is seen to bounce and increase at large iterations. (This bounce is more pronounced and happens at a lower iteration for certain cosmological model, e.g., one with high optical depth to reionization, τ.) This is a reflection of the problem of the RL method fitting the noise in the data. In contrast, in the IRL case the $\chi^2_{\rm eff}$ converges with iterations and to significantly better (lower) value that for the RL case.

D.3 Reference spectrum

In this subsection, we show that the reference spectrum used to remove numerical artifacts from the raw power spectrum recovered by the deconvolution is analytically well understood. The reference spectrum reflects the sensitivity of the kernel $|\bar{\Delta}(l,k)|^2$ to the k space. (Here, the over-bar in $|\bar{\Delta}(l,k)|$ alludes to the binned version related to $\bar{G}(l,k)$ following eqn (3.7)). In the regions of k space where the kernel probes $P(k)$ weakly, there is scope for changing the power spectrum without changing the C_l. In such degenerate regions, the Richardson Lucy method (both RL and IRL) pushes the power spectrum up to the extent possible changing the C_l.

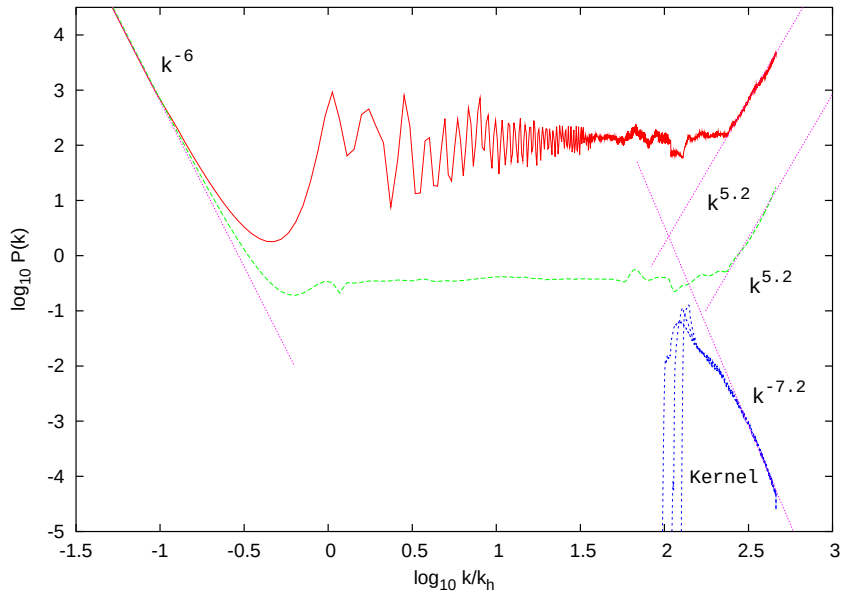

Figure D.3: The figure shows the $P_{\rm raw}(k)$ and $P_{\rm ref}(k)$ obtained from the WMAP binned data C_l^D for an initial guess $P^{(0)}(k) \propto 1/k^2$. The dashed straight line labeled corresponds to the analytical power law form ($k^{-4}P^{(0)}(k) = k^{-6}$) that matches the identical fall in $P_{\rm raw}(k)$ and $P_{\rm ref}(k)$ at low k. The dashed line matching the rise in $P_{\rm raw}(k)$ and $P_{\rm ref}(k)$ at large k corresponds to the analytical power law form ($k^{7.2}P^{(0)}(k) = k^{5.2}$) expected from the roughly $k^{-7.2}$ tail of the kernels for the last few multipole bins.

Figure D.3 shows that the strong features at the low k and high k are well fitted by analytically obtained power law forms. At the low wavenumbers ($k/k_h \ll 1$), the CMB anisotropy is dominated by the Sachs-Wolfe effect. The sensitivity of the CMB anisotropy to the power at very small wavenumbers is dominated by the lowest multipole as $|\bar{\Delta}(l,k)|^2 \propto k^{2l}$. This is the well known Grishchuk-Zeldovich effect [203]. When the quadrupole is included, $|\bar{\Delta}(l,k)|^2 \propto k^4$ is the strongest probe of the $P(k)$ at low wavenumbers. Hence, there is no change to C_l (here, chiefly the quadrupole) caused from this region of k space from the initial guess $P^{(0)}(k)$ onward if $P(k) \propto k^{-4+\epsilon}\, P^{(0)}(k)$ for $\epsilon > 0$. In our work we have used an initial guess of the form $P^{(0)}(k) \propto 1/k^2$. Hence, the slope of $P(k)$ at low k is driven to the $\sim k^{-6}$ form shown in figure D.3.

At the large k end, the $|\bar{\Delta}(l,k)|^2$ is governed by the power slope of the tail in the sensitivity of the highest few multipole bins shown plotted in figure D.3. The slope of these tails are well fitted by a power law form $k^{-7.2}$. Using the same argument, it is clear that there will be no change to the C_l caused from this region of k space from the initial guess onward if $P(k) \propto k^{7.2-\epsilon}\, P^{(0)}(k)$. For the initial guess $P^{(0)}(k) \propto 1/k^2$,

the rise at high k end is driven to a $\sim k^{5.2}$ form.

The division of reference spectrum used here is a simple numerical recipe for estimating and removing the artifacts of the deconvolution method for a given kernel. We have shown that the gross features of the $P_{\rm ref}(k)$ can be understood analytically. The finer features of $P_{\rm ref}(k)$ are likely linked to the details of the structure of $|\bar{\Delta}(l,k)|^2$ and will be explored in future work.

Appendix E

Least squares method

In parametric methods of reconstruction usually we use the method of **least squares** to determine the unknown parameters of a given model. The principle of the least square method can be derived from the principle of maximum likelihood, if the measurements follow a Gaussian distribution. We use this method to find the parameters of a given model when we fit the functional form of the model to the given data.

For a set of data with N data points we define χ^2 as

$$\chi^2 = \sum_{i=1}^{N} [\frac{y_i - f(x_i; a_m)}{\sigma_i}]^2 \tag{E.1}$$

where y_i is the measured value of the observed quantity for the ith data point at x_i and σ_i is its measured uncertainty. $f(x_i; a_m)$ is the predicted theoretical value of the quantity at x_i by using the given set of a_m parameters. In this method we try to minimize χ^2 by changing the values of a_m parameters.

If the derivatives of f with respect to a_m are known then we can find the solution (the value of the parameters) by

$$\frac{d\chi^2}{da_m} = 0 \tag{E.2}$$

which results in

$$\sum_i \frac{1}{\sigma_i^2} \frac{df(x_i; a_m)}{da} [y_i - f(x_i; a_m)] = 0 \tag{E.3}$$

If there are more than one unknown parameter in the a_m set, then we will have n simultaneous equations where n is the number of unknown parameters in set of a_m.

We should note that in many cases we solve these equations numerically. In fact we vary the values of a_m parameters to get the minimum χ^2. In many cases by using the available computational facilities it is much more trivial and faster to minimize the χ^2 numerically rather than find the a_m parameters by analytically solving the above equations.

If y measurement errors are correlated, then the χ^2 will become

$$\chi^2 = (\tilde{y} - \tilde{f})V^{-1}(y - f) \tag{E.4}$$

where V is the covariance matrix of the y_i measurements and $\tilde{y}$ and $\tilde{f}$ are transpose of y and f [34].

Goodness of fit

Now what is very important here is to make judgment and decision about the goodness of fit. In fact we need to check that the chosen model or the assumed functional form really does describe the observed data. Making a right decision is very crucial to test a theoretical model against observations. There is a mathematical basis on which we can relate the derived minimum χ^2, number of data points, number of the free unknown parameters of the model and the goodness of fit. The probability distribution for χ^2 is given by

$$P(\chi^2; N) = \frac{2^{-N/2}}{\Gamma(N/2)}\chi^{N-2}exp(-\chi^2/2) \tag{E.5}$$

where N is the number of data points minus the number of free unknown parameters of the assumed functional form. So to make decision about the goodness of fit for a functional form to a set of data we can calculate the relevant χ^2 probability function

$$Prob(\chi^2_{min}; N) = \int_{\chi^2_{min}}^{\infty} P(\chi^2; N)d\chi^2. \tag{E.6}$$

It simply means that for N degree of freedom (N=number of data points−number of free parameters of the assumed theoretical model) if we derive the minimum χ^2 to be χ^2_{min}, then $Prob(\chi^2_{min}; N)$ would be the probability of getting the value of χ^2 greater than or equal χ^2_{min}. If $Prob(\chi^2_{min}; N)$ be very small, then we can say that we have a bad fit to the data or the derived χ^2 is very much improbable for a correct assumed theoretical model. If $Prob(\chi^2_{min}; N)$ be considerable large, we can conclude with a high confidence that we have a good fit to the data and the assumed theoretical

model explain the data satisfactorily.

Bibliography

[1] A. Einstein, *Sitz Preuss. Akad. d. Wiss. Phys.-Math* **142** (1917).

[2] W. L. Freedman *et al.*, *Astrophys. J* **553** (2001) 47.

[3] J. Dunkley *et al.*, *submitted* (2008).

[4] A. A. Starobinsky,*Phys. Lett. B.* **91** (1980) 99.

[5] A. H. Guth, *Phys. Rev. D.* **23** (1981) 347.

[6] A. D. Linde,*Phys. Lett. B.* **108** (1982) 389.

[7] A. Albrecht and P. J. Steinhardt, *Phys. Rev. Lett* **48** (1982) 1220.

[8] A. A. Starobinsky,*Phys. Lett. B.* **117** (1982) 175.

[9] S. W. Hawking,*Phys. Lett. B.* **115** (1982) 295.

[10] A. Guth and S. Y. Pi, *Phys. Rev. Lett* **49** (1982) 1110.

[11] J. M. Bardeen, P. S. Steinhardt, S. M. Turner, *Phys. Rev. D.* **28** (1983) 679.

[12] W. M. Wood-Vasey *et al.*, *Submitted to Astrophys. J* (2008).

[13] Y. B. Zeldovich, *Mon. Not. Roy. Ast. Soc.* **160** (1972) 1 .

[14] E. R. Harrison, *Phys. Rev. D.* **1** (1970) 2726.

[15] P. J. E. Peebles and J. T. Yu, *Astrophys. J* **162** (1970) 815.

[16] S. Fukuda *et al.*, *Phys. Rev. Lett* **85** (2000) 3999.

[17] A. R. Liddle and D. H. Lyth, *Cosmological Inflation and Large Scale Structure*. Cambridge University Press, Cambridge, UK, 2000.

[18] W. Hu and N. Sugiyama, *Astrophys. J* **471** (1996) 30.

[19] V. Sahni and A. A. Starobinsky, *Int. J. Mod. Phys. D.* **9** (2000) 373.

[20] V. Sahni and A. A. Starobinsky, *Int. J. Mod. Phys. D.* **15** (2006) 2105.

[21] C. Contaldi *et al.*, *J. Cosmo. Astropart. Phys.* **0307** (2003) 002.

[22] A. A. Starobinsky, *J. Exp. Theo. Phys. Lett.* **55** (1992) 489.

[23] A. Vilenkin and L. H. Ford, *Phys. Rev. D.* **26** (1982) 1231.

[24] A. Shafieloo and T. Souradeep, *Phys. Rev. D.* **70** (2004) 043523.

[25] R. Sinha and T. Souradeep, *Phys. Rev. D.* **74** (2006) 043518.

[26] M. Joy, V. Sahni, A. A. Starobinsky, *Phys. Rev. D.* **D 77** (2008) 023514.

[27] M. Kowalski *et al.*, *accepted in Astrophys. J* (2008).

[28] A. A. Penzias and R. Wilson, *Astrophys. J* **142** (1965) 419.

[29] R. A. Alpher, H. Bethe and G. Gamow, *Phys. Rev.* **73, Issue 7** (1948) 803.

[30] G. F. Smoot *et al.*, *Astrophys. J* **396** (1992) L1.

[31] C. L. Bennett *et al.*, *Astrophys. J. Suppl* **148** (2003) 1.

[32] S. Courteau *et al.*, *Astrophys. J* **544** (2000) 636.

[33] W. Hu and S. Dodelson, *Ann. Rev. Astron. Astrophys.* **40** (2002) 171.

[34] R. J. Barlow, *Statistics, A guide to the Use of Statistical Methods in the Physical Sciences*. John Wiley and Sons, West Sussex, UK, 1989.

[35] W. M. Yao *et al.*, *Journal of Physics G* **33** (2006) 1.

[36] S. Dodelson, *Modern Cosmology*. Academic Press, San Diego, USA, 2003.

[37] S. M. Carroll, *Living Rev.Rel.* **4** (2001) 1.

[38] P. J. E. Peebles and B. Ratra, *Rev.Mod.Phys.* **75** (2003) 559.

[39] T. Padmanabhan, *Phys. Rep.* **380** (2003) 235.

[40] V. Sahni, *Lect.Notes Phys.* **653** (2004) 141.

[41] A. G. Riess *et al.*, *Astron. J.* **116** (1998) 1009.

[42] S. J. Perlmutter *et al.*, *Astrophys. J* **517** (1999) 565.

[43] R. A. Knop *et al.*, *Astrophys. J* **598** (2003) 102(k).

[44] J. L. Tonry *et al.*, *Astrophys. J* **594** (2003) 1.

[45] A. G. Riess *et al*, *Astrophys. J* **607** (2004) 665(R).

[46] A. G. Riess *et al*, *Astrophys. J* **659** (2007) 98.

[47] P. Astier *et al.*, *Astron. Astroph.* **447** (2006) 31.

[48] A. A. Starobinsky, *J. Exp. Theo. Phys. Lett.* **68** (1998) 757.

[49] D. Huterer and M. S. Turner, *Phys. Rev. D.* **60** (1999) 081301.

[50] T. Nakamura and T. Chiba, *Mon. Not. Roy. Ast. Soc.* **306** (1999) 696.

[51] T. D. Saini *et al.*, *Phys. Rev. Lett.* **85** (2000) 1162.

[52] T. Chiba and T. Nakamura, *Phys. Rev. D.* **62** (2000) 121301(R).

[53] V. Sahni, T. D. Saini, A. A. Starobinsky and U. Alam, *J. Exp. Theo. Phys. Lett.* **77** (2003) 201.

[54] U. Alam, V. Sahni and A. A. Starobinsky, *J. Cosmo. Astropart. Phys.* **0406** (2004) 008.

[55] M. Chevallier and D. Polarski, *Int. J. Mod. Phys. D.* **10** (2001) 213.

[56] J. Weller and A. Albrecht, *Phys. Rev. D.* **65** (2002) 103512.

[57] B. Gerke and G. Efstathiou, *Mon. Not. Roy. Ast. Soc.* **335** (2002) 33.

[58] I. Maor, R. Brustein, J. McMahon and P. J. Steinhardt, *Phys. Rev. D.* **65** (2002) 123003.

[59] P. S. Corasaniti and E. J. Copeland, *Phys. Rev. D.* **67** (2002) 063521.

[60] E. V. Linder, *Phys. Rev. L.* **90** (2003) 091301.

[61] Y. Wang and P. Mukherjee, *Astrophys. J* **606** (2004) 654.

[62] T. D. Saini, J. Weller and S. L. Bridle, *Mon. Not. Roy. Ast. Soc.* **348** (2004) 603.

[63] S. Nesseris and L. Perivolaroupolos, *Phys. Rev. D.* **70** (2004) 043531.

[64] Y. Gong, *Int. J. Mod. Phys. D.* **14** (2005) 599.

[65] R. Lazkoz, S. Nesseris and L. Perivolaroupolos, *J. Cosmo. Astropart. Phys.* **0511** (2005) 010.

[66] J. Simon, L. Verde and R. Jimenez, *Phys. Rev. D.* **71** (2005) 123001.

[67] Z-K. Guo, N. Ohta, Y-Z. Zhang, *Phys. Rev. D.* **72** (2005) 023504.

[68] U. Alam, V. Sahni, T. D. Saini and A. A. Starobinsky, *Mon. Not. Roy. Ast. Soc.* **354** (2004) 275.

[69] U. Alam, V. Sahni, T. D. Saini and A. A. Starobinsky, *Mon. Not. Roy. Ast. Soc.* **344** (2003) 1057.

[70] Y. Gong, *Cosmo. Quant. Grav.* **22** (2005) 2121.

[71] B. Bassett, P. S. Corasaniti and M. Kunz, *Astrophys. J* **617** (2004) L1.

[72] Y. Wang and G. Lovelace, *Astrophys. J* **562** (2001) L115.

[73] D. Huterer and G. Starkman, *Phys. Rev. Lett.* **90** (2003) 031301.

[74] T. D. Saini, *Mon. Not. Roy. Ast. Soc.* **344** (2003) 129.

[75] R. A. Daly and S. G. Djorgovsky, *Astrophys. J* **597** (2003) 9.

[76] R. A. Daly and S. G. Djorgovsky, *Astrophys. J* **612** (2004) 652.

[77] Y. Wang and M. Tegmark, *Phys. Rev. D.* **71** (2005) 103513.

[78] P. Coles and F. Lucchin, *Cosmology, the origin and evolution of large scale structure.* John Wiley and sons, West Sussex, UK, 1995.

[79] V. J. Martinez and E. Saar, *Statistics of Galaxy Distribution*. Chapman and Hall, Boca Raton, FL, USA, 2002.

[80] V. Sahni and P. Coles, *Phys.Rept.* **262** (1995) 1.

[81] G. Aldering *et al*, *submitted to PASP* (2004) `astro-ph/0405232`.

[82] M. Tegmark, *Phys. Rev. D.* **66** (2002) 103507.

[83] C. Deffayet, G. Dvali and G. Gabadadze, *Phys. Rev. D.* **65** (2002) 044023.

[84] K. Freese and M. Lewis, *Phys. Lett. B.* **540** (2002) 1.

[85] V. Sahni and Y. V. Shtanov, *J. Cosmo. Astropart. Phys.* **0311** (2003) 014.

[86] S. M. Carroll, M. Hoffman and M. Trodden, *Phys. Rev. D.* **68** (2003) 023509.

[87] S. Capozziello, S. Carloni, A. Troisi *Recent Research Developments in Astronomy and Astrophysics-RSP/AA* **21** (2003).

[88] S. Nojiri and S.D. Odintsov, *Phys. Rev. D.* **68** (2003) 123512.

[89] A. D. Dolgov and M. Kawasaki, *Phys. Lett. B.* **573** (2003) 1.

[90] V. Sahni *Cosmological Surprises from Braneworld models of Dark Energy*, *Proceedings of the 14th Workshop on General relativity and Gravitation (JGRG14), Kyoto University, Japan*, Ed. by W. Hikida, M. Sasaki, T. Tanaka and T. Nakamura (2004) 95.

[91] G. Dvali, G. Gabadadze, M. Porrati, *Phys. Lett. B.***485** (2000) 208.

[92] V. Sahni and Yu. Shtanov, *Phys. Rev. D.* **71** (2005) 084018.

[93] E. V. Linder (2004) `hep-th/0410017`.

[94] U. Alam and V. Sahni (2002) `astro-ph/0209443`.

[95] V. Sahni and L. Wang, *Phys. Rev. D.* **62** (2000) 103517.

[96] D. J. Eisenstein *et al.*, *Astrophys. J* **633** (2005) 560.

[97] U. Alam, V. Sahni, A. A. Starobinsky, *J. Cosmo. Astropart. Phys.* **0702** (2007) 002.

[98] Y. Gong and A. Wang, *Phys. Rev. D.* **75** (2007) 043520.

[99] E. V. Linder, *Phys. Rev. D.* **68** (2007) 083504.

[100] D. Spergel *et al.*, *Astrophys. J. Supp* **170** (2007) 377.

[101] "Legacy Archive for Microwave Background Data Analysis (LAMBDA)". http://lambda.gsfc.nasa.gov/.

[102] M. Tegmark *et al.*, *Astrophys. J.* **606** (2004) 702.

[103] S. Cole *et al.*, *Mon. Not. Roy. Ast. Soc.* **362** (2005) 505.

[104] S. Fay and R. Tavakol, *Phys. Rev. D.* **74** (2006) 083513.

[105] S. Nesseris, L. Perivolaropoulos, *J. Cosmo. Astropart. Phys.* **0702** (2007) 025.

[106] H. K. Jassal, J. S. Bagla, T. Padmanabhan, *Phys. Rev. D.* **72** (2005) 103503.

[107] Ya. B. Zeldovich, *Sov. Phys. Uspekhi* **11** (1968) 381.

[108] S. Weinberg, *Rev. Mod. Phys.* **61** (1989) 1.

[109] D. N. Spergel *et al.*, *Astrophys. J. Supp* **148** (2003) 175.

[110] E. Komatsu *et al.*, *submitted to Astrophys. J. Supp* arXiv:0803.0547.

[111] Y. Wang and M. Tegmark, *Phys. Rev. Lett* **92** (2004) 241302.

[112] H. K. Jassal, J. S. Bagla and T. Padmanabhan, *Mon. Not. Roy. Ast. Soc.* **356** (2005) L11.

[113] S. Nesseris and L. Perivolaropoulos, *Phys. Rev. D* **72** (2005) 123519.

[114] F. Simpson and S. Bridle, *Phys. Rev. D* **73** (2006) 083001.

[115] A. Shafieloo, *Mon. Not. Roy. Ast. Soc.* **380** (2007) 1573.

[116] A. Shafieloo, U. Alam, V. Sahni, A. A. Starobinsky, *Mon. Not. Roy. Ast. Soc.* **366** (2006) 1081.

[117] M. Kunz, *to be published in J. physics* arXiv:0710.5712.

[118] T. Barreiro, E.J. Copeland, N.J. Nunes, *Phys. Rev. D* **61** (2000) 127301.

[119] G. Efstathiou, *to be published in Il Nuovo Cimento* (2008) astro-ph/0712.1513.

[120] V. Sahni, Y. Shtanov, A. Viznyuk, *J. Cosmo. Astropart. Phys.* **0512** (2005) 005.

[121] B. Boisseau, G. Esposito-Farese, D. Polarski, A. A. Starobinsky, *Phys. Rev. Lett* **85** (2000) 2236.

[122] J. M. Virey *et al.*, arXiv:0802.4407.

[123] E. E. Ishida, R. R. Reis, A. V. Toribio, I. Waga, *Astroparticle Phys.* **28** (2008) 547.

[124] J. A. Lima, arXiv:0708.3414.

[125] J. V. Cunha and J. A. Lima, arXiv:0805.1261.

[126] N. Pires, Z. H. Zhu, J.S. Alcaniz, *Phys. Rev. D* **73** (2006) 123530.

[127] R. Jimenez, L. Verde, T. Treu and D. Stern, *Astrophys. J.* **593** (2003) 622.

[128] J. Santos, J. S. Alcaniz, M. J. Reboucas, N. Pires, *Phys. Rev. D* **76** (2007) 043519.

[129] A. Sandage, *Ann. Rev. Astron. Astrophys.* **26** (1988) 561.

[130] S. W. Allen *et al.*, *Mon. Not. Roy. Ast. Soc.* **383** (2008) 879.

[131] A. Shafieloo and T. Souradeep, *Phys. Rev. D* **78** (2008) 023511.

[132] I. Maor, R. Brustein and P. J. Steinhardt, *Phys. Rev. Lett* **86** (2001) 6.

[133] C. L. Bennett *et al.*, *Astrophys. J. Supp* **148** (2003) 1.

[134] G. Hinshaw *et al.*, *Astrophys. J. Supp* **148** (2003) 135.

[135] M. Limon *et al.*, *First Year Wilkinson Microwave Anisotropy Probe (WMAP) Observations: Explanatory Supplement* (http://lambda.gsfc.nasa.gov/).

[136] A. Kogout *et al.*, *Astrophys. J. Supp* **148** (2003) 161.

[137] D. Spergel *et al.*, *Astrophys. J. Supp* **170** (2007) 377.

[138] G. Hinshaw *et al.*, *Astrophys. J. Supp* **170** (2007) 288.

[139] A. A. Starobinsky, *J. Exp. Theo. Phys. Lett.* **42** (1985) 124.

[140] L. A. Kofmann, A. D. Linde, A. A. Starobinsky, *Phys. Lett. B.***157** (1985) 361.

[141] J. Silk and M. S. Turner,*Phys. Rev. D* **35** (1987) 419.

[142] J. R. Bond and D. Salopek,*Phys. Rev. D* **40** (1989) 1753.

[143] D. Polarski and A. A. Starobinsky, *Nucl. Phys. B.***385** (1992) 623.

[144] J. Lesgourgues, D. Polarski, A. A. Starobinsky, *Mon. Not. Roy. Ast. Soc.* **308** (1999) 281.

[145] T. Souradeep, J. R. Bond, L. Knox, G. Efstathiou, M.S. Turner, *Proc. COSMO-97 – International workshop on 'Particle Physics and Early Universe' Sept. 15-19, 1997, Ambleside, U.K.*, (ed L. Roszkowski, World Scientific, 1998) `astro-ph/9802262`.

[146] A. Shafieloo, *M. Sc. dissertation; Supervisor T. Souradeep, Univ. of Pune* (2002).

[147] S. L. Bridle, A. M. Lewis, J. Weller, G. Efstathiou, *Mon. Not. Roy. Ast. Soc.* **342** (2003) L72.

[148] P. Mukherjee and Y. Wang, *Astrophys. J.* **598** (2003) 779.

[149] S. Hannestad, *J. Cosmo. Astropart. Phys.* **0404** (2004) 002.

[150] M. Matsumiya, M. Sasaki, J. Yokoyama, *Phys. Rev. D.* **65** (2002) 083007.

[151] N. Kogo, M. Matsumiya, M. Sasaki, J. Yokoyama, *Astrophys. J* **607** (2004) 32.

[152] A. Niarchou, A. H. Jaffe and L. Pogosian, *Phys. Rev. D.* **69** (2004) 063515.

[153] D. Tocchini-Valentini, Y. Hoffman, J. Silk, *Mon. Not. Roy. Ast. Soc.* **367** (2006) T1095.

[154] U. Seljak and M. Zaldarriaga, *Astrophys. J* **469** (1996) 437 (http://cmbfast.org/).

[155] S. Podariu *et al.*, *Astrophys. J* **559** (2001) 9.

[156] L. B. Lucy, *Astron. J* **79** (1974) 6.

[157] B. H. Richardson, *J. Opt. Soc. Am.* **62** (1972) 55.

[158] C. M. Baugh and G. Efstathiou, *Mon. Not. Roy. Ast. Soc.* **265** (1993) 145.

[159] C. M. Baugh and G. Efstathiou, *Mon. Not. Roy. Ast. Soc.* **267** (1994) 323.

[160] R. L. White, *A. S. P. Conference series.* **61** (1994) 292.

[161] G. Efstathiou, *Mon. Not. Roy. Ast. Soc.* **348** (2004) 885.

[162] M. Tegmark, A. de Oliveira-Costa, A. Hamilton, *Phys. Rev. D.* **68** (2003) 123523.

[163] L. Knox, *Phys. Rev. D.* **52** (1995) 4307.

[164] J. M. Cline, P. Crotty, J. Lesgourgues, *J. Cosmo. Astropart. Phys.* **0309** (2003) 010.

[165] S. M Leach, M. Sasaki, D. Wands and A. Liddle, *Phys. Rev. D.* **64** (2001) 023512.

[166] N. Kaloper and M. Kaplinghat, *Phys. Rev. D.* **68** (2003) 123522.

[167] J. Yokoyama, *Phys. Rev. D.* **59** (1999) 107303.

[168] B. Feng and X. Zhang, *Phys. Lett. B.* **570** (2003) 145.

[169] S. Tsujikawa, R. Maartens, R. Brandenberger, *Phys. Lett. B.* **574** (2003) 141.

[170] Y. Piao, B. Feng, X. Zhang, *Phys. Rev. D.* **63** (2000) 084520.

[171] J. Lasue and T. Souradeep, *in preparation*.

[172] J. P. Luminet *et al.*, *Nature* **425** (2003) 593.

[173] A. Hajian and T. Souradeep *et al.*, *Astrophys. J. Lett.* **597** (2003) L5.

[174] I. Daubechies, *Ten Lectures on Wavelets, SIAM, Philadelphia, PA; CBMS-NSF Conference Series in Applied Mathematices* **Vol.64**(1992).

[175] C. L. Kuo *et al.*, *Astrophys. J* **664** (2007) 687.

[176] T. Roy Choudhury, A. Ferrara, *Mon. Not. Roy. Ast. Soc.* **371** (2006) L55.

[177] S. Samui, R. Srianand, K. Subramanian, *Mon. Not. Roy. Ast. Soc.* **377** (2007) 285.

[178] B. Fields, S. Sarkar, *J. Phys. G.* **33** (2006) 1.

[179] O. Lahav, A. R. Liddle, *J. Phys. G.* **33** (2006) 1.

[180] A. Shafieloo *et al.*, *Phys. Rev. D.* **75** (2007) 123502.

[181] P. Hunt, S. Sarkar, *Phys. Rev. D.* **76** (2007) 123504.

[182] K. Heitmann *et al.*, *Astrophys. J* **646** (2006) L1.

[183] W. A. Fendt, B. D. Wandelt, *Astrophys. J* **654** (2006) 2.

[184] A. Hajian, *Phys. Rev. D.* **75** (2007) 083525.

[185] T. Auld *et al.*, *Mon. Not. Roy. Ast. Soc.* **376** (2007) L11.

[186] D. Munshi, T. Souradeep and A. A. Starobinsky, *Astrophys. J* **454** (1995) 552.

[187] Y. Jing and L. Fang, *Phys. Rev. Lett* **73** (1994) 1882.

[188] J. Martin and C. Ringeval, *Phys. Rev. D.* **69** (2004) 083515.

[189] D. Tocchini-Valentini, M. Douspis, J. Silk, *Mon. Not. Roy. Ast. Soc.* **359** (2005) 31.

[190] B. Ratra and J. Peebles, *Phys. Rev. D.* **52** (1995) 1837.

[191] K. Yamamoto, M. Sasaki, T. Tanaka, *Phys. Rev. D.* **54** (1996) 1996.

[192] A. A. Starobinsky, *Proc. of Cosmo-94*, Ed. M.Y. Klopov, M. E. Prokhorov, A. A. Starobinsky, and J. Tran Thanh Van,(Editions Frontieres, 1996).

[193] J. R. Bond, D. Pogosyan, and T. Souradeep, *Phys. Rev. D.* **62** (2000) 043005.

[194] A. A. Starobinsky, *Sov. Astron. Lett.* **11** (1985) 133.

[195] R. Davis *et al.*, *Phys. Rev. Lett* **69** (1992) 1856.

[196] T. Souradeep and V. Sahni, *Mod. Phys. Lett. A.* **7** (1992) 3541.

[197] R. Crittenden *et al.*, *Phys. Rev. Lett* **71** (1993) 324.

[198] G. Efstathiou and J. R. Bond, *Mon. Not. Roy. Ast. Soc.* **218** (1986) 103.

[199] P. Crotty *et al.*, *Phys. Rev. Lett* **91** (2003) 171301.

[200] M. Tegmark and M. Zaldarriaga, *Phys. Rev. D.* **66** (2002) 103508.

[201] E. Gawiser, *Ph.D. Thesis, U.C. Berkeley* (1999).

[202] J. Hinderks*et al.*, `arXiv:0805.1990`.

[203] L. P. Grishchuk and Ya. B Zeldovich, *Soviet Astronomy* **22** (1978) 125.